An ytterbium-doped fiber laser at 1.1 μm

By
Zachary Jordan Chaboyer

A thesis submitted to the faculty of graduate studies
Lakehead University
In partial fulfillment of the requirements for the degree of
Master of Science in Physics

Department of Physics
Lakehead University
July 2012

Abstract

A pulsed ytterbium-doped fiber laser is proposed and developed. A length of samarium-doped fiber was inserted into the laser cavity to induce passive Q-switching. The laser oscillated in the continuous wave, Q-switched mode-locked or Q-switched regime depending on adjustment of the intracavity polarization controller and the pump power. Q-switched pulses with a pulse energy of ~7.5 nJ and duration of ~70 ns were obtained at a pump power of ~1500 mW, corresponding to a peak output power of ~106 mW at an average power of 2 mW. The low output power was attributed to the low coupling efficiency of pump radiation into the cavity and the high cavity losses. All results were obtained at room temperature.

Acknowledgement

I would like to take this opportunity to thank my family and friends whose encouragement and support have been invaluable throughout my studies at Lakehead University. I would especially like to express my gratitude toward my supervisor, Dr. Gautam Das. I would not have been able to complete this task without his mentorship and the many hours he devoted to assisting and advising me with my work. I would also like to thank: my fellow research group members, Jonas Valiunas, Peter Moore and Andrew Drainville, for their help and advice and for making the days spent experimenting, reading, studying and writing in the laboratory and office much more enjoyable; Jean-Marc Lachaine, Kristine Carey, my supervisory committee members (Dr. Apichart Linhananta and Dr. Werden Keeler) and the entire Physics faculty at Lakehead University for their instruction throughout my years of study in this department.

This thesis is dedicated to my mother, Kathryn Berry,
and to my sister, Sarah Chaboyer

Contents

Chapter 3

Applications of the Developed Laser

Chapter 4

List of Figures

Chapter 1

Introduction

1.1: Introduction

Laser technology has reached a high level of maturity and has taken a prominent position over the course of its 50 year history. Lasers are now used in everything from household tools for leveling and distance measurement to particle accelerators and experimental fusion reactors [2;3]. Fiber lasers are one type of laser that has gone through intense development in the last two decades. Fiber lasers are compact, reliable and environmentally stable compared to their bulk counterparts and are commercially available. Despite the progress already made by fiber lasers, there is still much room for the development of new lasers intended for specific applications.

The objective of the proposed thesis is to design a fiber laser in the 1.1 μm spectral region using an ytterbium-doped fiber as a gain medium. We will also explore the possibility of operating the laser in the continuous wave (CW) and pulsed regimes. Finally, we will discuss the possible application of the proposed laser in sensing.

The present chapter will describe different types of lasers and their working principles.

1.2: Lasers

"LASER" is an acronym for "light amplification by stimulated emission of radiation". A laser is a device that takes advantage of the phenomenon of stimulated emission to generate a beam of intense, temporally and spatially coherent optical radiation. Schawlow and Townes first proposed the laser in 1958, and Theodore Maiman constructed the first solid-state ruby laser soon after [4;5].

A laser in its simplest form comprises two main parts: a gain medium in which the signal radiation is amplified via stimulated emission, and a resonant cavity within which the gain medium is placed to provide feedback of radiation into the medium so that signal amplification can continue as long as pumping is maintained [6]. Figure 1.1 shows a schematic diagram of a typical laser system.

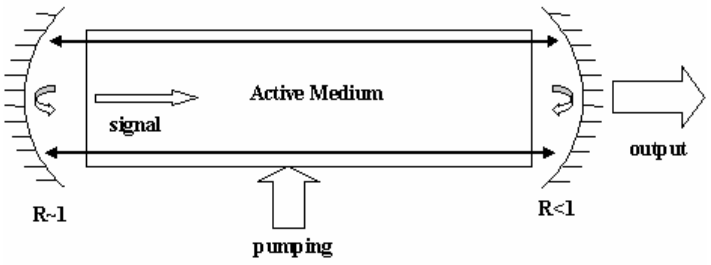

Figure 1.1: A basic laser oscillator.

When an electromagnetic wave with frequency ω travelling along the x-axis and polarized along the z-axis is incident on an atom in the ground state, the oscillating

electric field of the EM wave can induce an electronic transition to an excited state, with the atom absorbing energy $E_b - E_a = \hbar\omega_0$ (figure 1.2 a). The probability of this transition is [7]:

$$P_{a\to b}(t) = \left(\frac{\left| e\langle \psi_b | z | \psi_a \rangle \right|}{\hbar} \right)^2 \frac{\sin^2[(\omega_0 - \omega)t/2]}{(\omega_0 - \omega)^2} \tag{1.2.1}$$

If another photon of the same frequency interacts with the same atom while it is still in the excited state, it can induce a transition back to the ground state (figure 1.2 c). This transition occurs with the same probability as the excitation from the ground state and leads to the emission of two photons of energy $\hbar\omega_0$ with the same phase and polarization. The above phenomenon is known as stimulated emission.

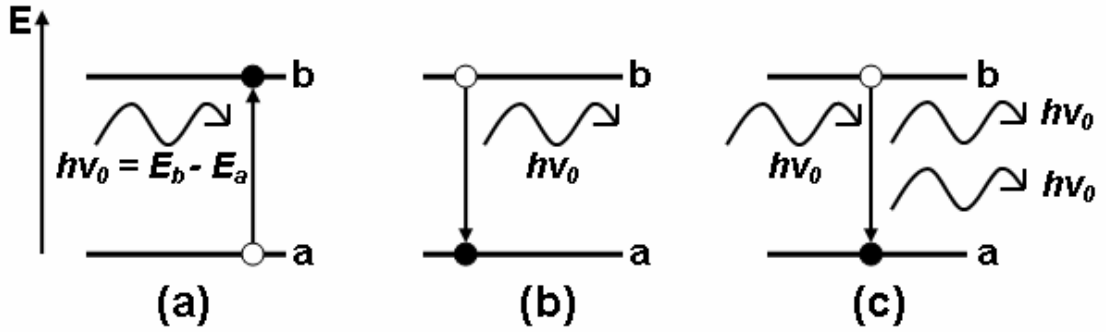

Figure 1.2: a) Absorption of a photon with energy $h\nu_0$ inducing a transition from the ground state *"a"* to the excited state *"b"*. b) Spontaneous emission of a photon resulting in a transition from the excited state to the ground state. c) Stimulated emission.

In order for stimulated emission to dominate over absorption, population inversion is required, which is achieved by pumping the amplifying medium [6]. Pumping is carried out by transferring energy to the amplifying medium in order to

induce transitions to the excited state. Population inversion is achieved when a greater number of atoms occupy the excited state than the ground state.

Another important element for laser oscillation is a resonant cavity to direct the signal radiation through the amplifying medium repeatedly, allowing a high intensity wave to build up within the cavity (figure 1.1). In order for a given frequency to oscillate within an optical cavity it must experience a zero net phase change on each cavity round trip. This is known as the resonant phase condition and is written as [8]:

$$\begin{aligned} 2nL_{cavity} &= m\lambda \\ \nu_m &= m\frac{c}{2nL_{cavity}} \\ \Delta\nu_{FSR} &= \nu_m - \nu_{m-1} = \frac{c}{2nL_{cavity}} \end{aligned} \tag{1.2.2}$$

Where c is the speed of light in a vacuum, n is the effective refractive index inside the cavity, L_{cavity} is the cavity length and m is an integer. The spacing between resonant frequencies is called the free spectral range (FSR) of the cavity and is denoted by $\Delta\nu_{FSR}$. Another important cavity parameter is the finesse, defined as the ratio of the FSR to the linewidth of the resonant peaks (FWHM:Full width at half maximum) [9]:

$$F = \frac{\Delta\nu_{FSR}}{\Delta\nu\big|_{FWHM}} = \frac{\pi\sqrt{R}}{1-R} \tag{1.2.3}$$

The above expression neglects cavity losses other than transmission through the cavity mirrors. It is clear that a high finesse can be achieved with high mirror reflectivity and low cavity losses. However, the linewidth also exhibits an inverse dependence on the

FSR. Therefore, at a constant finesse, there is a trade-off between having a large FSR and a narrow linewidth.

Lasers with different gain media such as gas, dye and semiconductor materials have been developed. Lasers may furthermore be classified in the wavelength domain as single-wavelength [10] or multi-wavelength [11] and in the time domain as continuous or pulsed mode [12].

1.3: Optical Fibers

An optical fiber is a coaxial cylindrical dielectric waveguide designed to transmit EM waves at optical frequencies [13]. Optical fibers were first proposed and produced by K.C. Kao and G.A. Hockham in 1966 [14]. Since this development, refinements in fiber design and fabrication processes have led to the production of fibers with low dispersion and losses (0.2 dB/km), and optical fibers now hold a prominent place as the backbone of communication systems.

The material of choice for most telecommunications-grade optical fibers is fused (amorphous) silica glass. A glass becomes a viscous fluid above the glass transition temperature with its viscosity decreasing continuously as the temperature is further increased [15]. This property makes glasses ideal for drawing into thin fibers of arbitrary and controllable thickness when heated to temperatures at which they become soft and ductile. The resulting fibers are extremely durable, with tensile strengths as high as steel wires of the same diameter, and are resistant to degradation by most chemicals at ambient temperatures [16]. Most importantly for communication, pure silica is highly transparent

at optical frequencies, allowing transmission distances of tens of kilometers at a wavelength band centered at ~1.55μm [17].

Optical fibers in their most simple form consist of a cylindrical glass core surrounded by a coaxial cylindrical cladding made of glass of slightly lower refractive index. The complete glass fiber is then coated with a protective polymer jacket. Fibers in which the core and cladding refractive indices have no radial dependence are called step index fibers (figure 1.3).

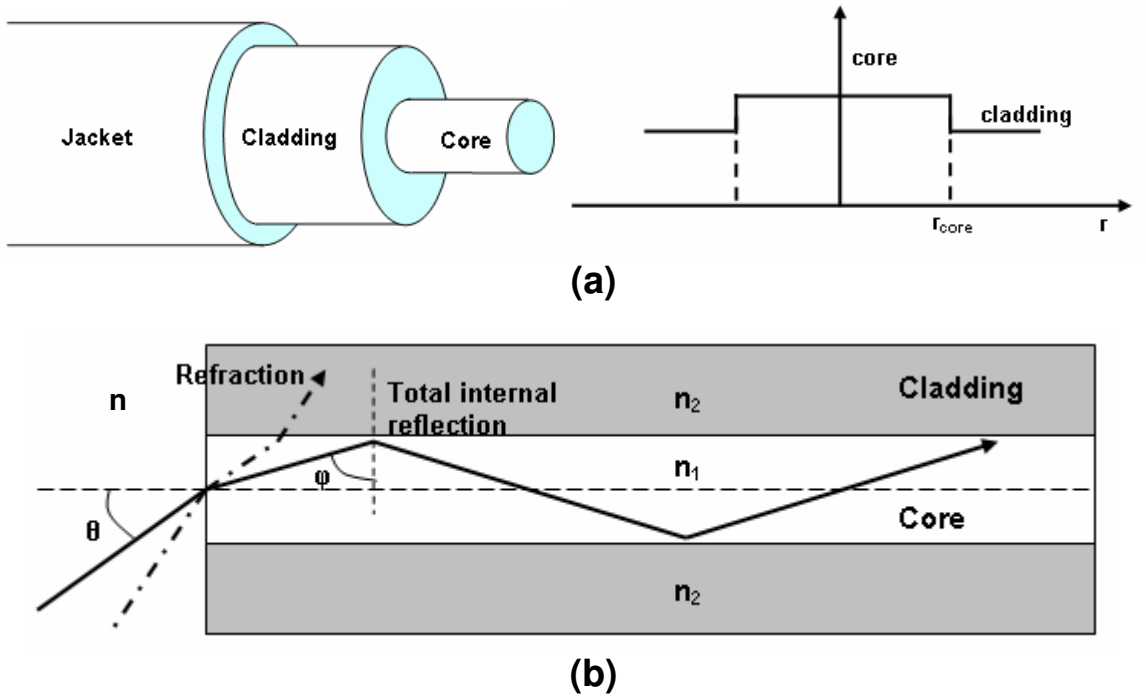

Figure 1.3: (a) Left: Structure of a single-clad optical fiber. Right: Refractive index profile of a step-index fiber. (b) Confinement of light within the fiber core by total internal reflection.

Light is confined within the core of a step index fiber by means of total internal reflection at the core-cladding interface. Light rays incident on the fiber end face within a certain angle known as the acceptance angle will couple into the fiber (figure 1.3). The

maximum angle of incidence "θ_{max}" for coupling to the fiber is related to the core and cladding refractive indices [13]:

$$n \sin \theta_{0,\max} = \left(n_1^2 - n_2^2\right)^{1/2} \tag{1.3.1}$$

The quantity $n\sin\theta_{0,max}$ quantifies the light accepting capability of a fiber and is known as the numerical aperture.

The above ray optics description does not give an accurate picture of light propagation within an optical fiber. In general a dielectric waveguide supports a number of transverse modes [13]. Each of these modes corresponds to a solution of Maxwell's equations in cylindrical coordinates subject to boundary conditions at the core-cladding interface [18]. Maxwell's equations in an isotropic non-conducting dielectric medium in the absence of currents and free charges are written as follows [8]:

$$\nabla \times \vec{E} = -\frac{\partial \vec{B}}{\partial t} \tag{1.3.2a}$$

$$\nabla \times \vec{H} = \frac{\partial \vec{D}}{\partial t} \tag{1.3.2b}$$

$$\nabla \cdot \vec{D} = 0 \tag{1.3.2c}$$

$$\nabla \cdot \vec{B} = 0 \tag{1.3.2d}$$

One can obtain wave equations by combining equations 1.3.2 (a) to (d), and each solution of this equation represents a unique transverse electric and magnetic field distribution of the propagating waves. The solution of the wave equations take the form [13]:

$$\begin{aligned} \vec{E}(\vec{r},t) &= \vec{E}(r,\varphi)e^{i(\omega t-\beta z)} \\ \vec{H}(\vec{r},t) &= \vec{H}(r,\varphi)e^{i(\omega t-\beta z)} \end{aligned} \tag{1.3.3}$$

The order of a transverse mode corresponds to the number of zeros in the optical field profile [18]. For the strongest waveguiding, it is advantageous to limit the propagating light to a single zero-order mode. The number of transverse modes is quantified by the so-called normalized frequency, or "*V-number*" [9]:

$$V = k_0 a\left(n_1^2 - n_2^2\right)^{1/2} \tag{1.3.4}$$

Where a is the core radius of the fiber. The fundamental, lowest order transverse mode exists for all values of V, and the first higher order mode appears for $V>2.405$ [9]. This is known as the cut-off condition for single mode propagation in fibers. A single mode fiber may be produced by choosing values of a, n_1 and n_2 that fulfill the cut-off condition at a given wavelength ($V<2.405$). A single-mode fiber operating at 1.55 μm has lower attenuation, and is free from intermodal dispersion. Using a single-mode fiber thus allows the integrity of an optical signal to be maintained over a much longer distance [13]. For these reasons, single mode fibers have become the backbone of modern communication networks.

1.4: Rare-Earth-Doped Fibers

The properties of optical fibers can be altered significantly by introducing impurities (dopants) into the glass from which the fiber is fabricated. One of the most important dopants is rare-earth ions. The rare earths comprise two rows of the periodic table: the lanthanides and actinides, of which only the lanthanides (row six) are used as dopants. They usually exist within a glass or crystal as a triply ionized cation, displacing an ion of the same charge in the host medium [19]. Erbium (Er), ytterbium (Yb),

neodymium (Nd), thulium (Tm), praseodymium (Pr), holmium (Ho) and samarium (Sm) have all been used as dopants in optical fibers, but Yb and Er have by far found the most widespread technological application.

Lanthanide ions are attractive as gain media due to their large selection of absorptive and luminescent transitions between sublevels of their partially filled 4f shell [20]. Although the intra-4f transitions are forbidden by parity selection rules, their probabilities become non-zero in a host due to the effect of the field applied by the ions in the surrounding glass or crystal matrix [21]. The resulting transition probability for an atom with valence electron configuration $4f^N$ between states with quantum numbers *S, L* and *J* and *S', L'* and *J'* and wavefunctions ψ_i and ψ_f is calculated as [22]:

$$S = \frac{1}{e^2}\left|\left\langle \psi_f \left| H \right| \psi_i \right\rangle\right|^2 = \sum_{k=2,4,6} \Omega_k \left|\left\langle f^N \gamma S' L' J' \left| U^{(k)} \right| f^N \gamma S L J \right\rangle\right|^2 \qquad (1.4.1)$$

Where *H* is the electric dipole Hamiltonian, which is expressed in the form of a rank *k* tensor and γ is a degeneracy factor. The low probability for luminescent transitions leads to long excited state lifetimes in most rare earth ions, allowing a large amount of energy to be stored within the doped medium, leading to a high gain [23]. It is possible to construct pulsed lasers using doped fibers by releasing the stored energy in a single high-energy pulse. This technique is known as Q-switching and is discussed in section 1.10.

An unpumped length of doped fiber can exhibit an intensity dependent absorption at the transition wavelengths of the dopant ions. As the incident intensity increases the number of dopant ions in the ground state decreases, leading to a decrease in the amount of light absorbed by the dopants in the fiber. Media that display an intensity dependent

absorption are known as saturable absorbers, and are discussed in detail in the next chapter.

In this work, an ytterbium-doped fiber is chosen as the gain medium for a laser oscillating in the 1.1 μm wavelength band by virtue of its broad emission spectrum in that region [24], and an unpumped samarium doped fiber is chosen to provide the saturable absorption effect.

1.5: Fiber Lasers

A fiber laser is essentially a laser oscillator in which a section of rare earth doped fiber serves as the gain medium. Fiber lasers possess several advantages over other solid state laser designs: first, the laser cavity may be constructed by fusion splicing fibers together, bypassing the careful and skilled alignment required in open air cavities. Second, the confinement of the lasing light within the fiber core results in a near-diffraction limited beam [25]. Third, the cylindrical symmetry of fiber waveguides enables efficient interaction between the pump beam and the active medium. Finally, the extremely high surface area to volume ratio of optical fibers allows excess heat produced within the fiber to be easily dissipated so that problems of thermally-induced damage and beam distortion due to thermal lensing (beam focusing due to thermally-induced changes in refractive index) that occur in bulk lasers are avoided [26]. These advantages make fiber lasers ideal candidates for application in inexpensive, versatile and durable instruments.

Optical feedback to the gain medium in a fiber laser may be provided by a wide variety of optical cavity geometries. This allows a resonator type to be chosen to best

provide the desired laser characteristics (power, longitudinal-mode-structure, pulsed or cw operation, etc.) for any given application. A fiber cavity may exist in two basic configurations: the linear configuration (Fabry-Perot) and the ring configuration. A linear cavity is formed by inserting the gain fiber between two reflectors, most commonly fiber Bragg gratings (Section 2.4) [27]. Ring cavities are constructed using either a fused fiber coupler [28;29], or an optical circulator and reflector (figure 1.4 b) [30]. A linear laser cavity tends to suffer from an effect called spatial hole burning effect, due to the interference between counter-propagating signal waves. The gain is preferentially saturated in the antinodes of the resulting standing wave at the primary lasing frequency, leading to a gain in the unsaturated regions (nodes) for weaker cavity modes, and possible multimode oscillation of the laser [31]. Spatial hole burning is absent in ring cavities due to unidirectional propagation of waves in the cavity. Despite this advantage, ring cavities typically contain components having extra lengths of fiber, and the bending radii of the cavity fibers must be large to avoid bend losses [32]. This makes minimizing the length of such cavities more difficult, so longitudinal mode spacing is usually shorter. One also usually encounters more difficulty stabilizing ring cavities against environmental fluctuations such as vibration and temperature [25].

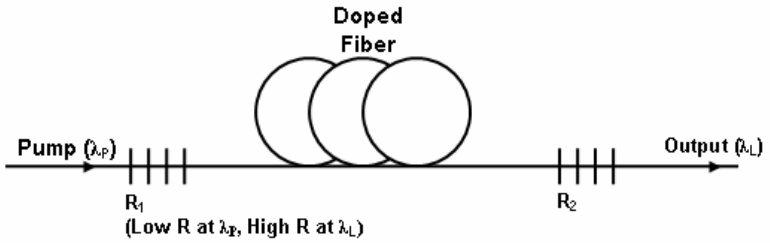

(a)

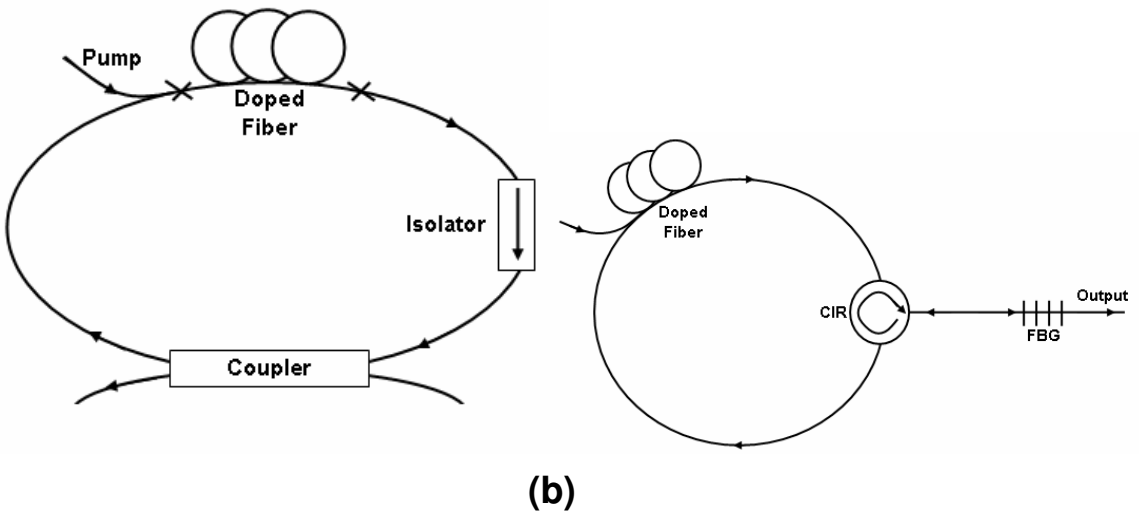

Figure 1.4: Fiber laser cavity configurations: (a) Basic linear fiber laser cavity, the first reflector (R_1) has a low reflectivity at the pump wavelength to allow for end-pumping. The output reflector (R_2) has a lower reflectivity than R_1 at the laser wavelength. (b) Left: Basic fiber ring laser formed by splicing a pumped gain fiber between an input and output of a fused fiber coupler. Right: Fiber ring laser formed from a fiber circulator (CIR) and a fiber Bragg grating reflector (FBG).

A greater degree of control may be exerted over the longitudinal mode structure of a laser resonator by employing coupled-cavity type designs. Combining two linear cavities of different lengths [33] or a ring cavity and a short linear cavity [30] results in a modulation in the longitudinal mode spectrum of the lower FSR cavity by the higher FSR cavity, limiting the overall number of longitudinal modes present in the laser output. This is a highly effective method for achieving single frequency oscillation in a fiber laser [10].

Pump energy is typically delivered to the gain fiber by means of a fiber-coupled semiconductor diode laser. The dopant ions may either be excited by unidirectional pumping (figure 1.5 a), or bidirectional pumping (figure 1.5 b). A bidirectional pumping scheme typically allows for greater pump-to-signal conversion efficiency and therefore higher output power [34].

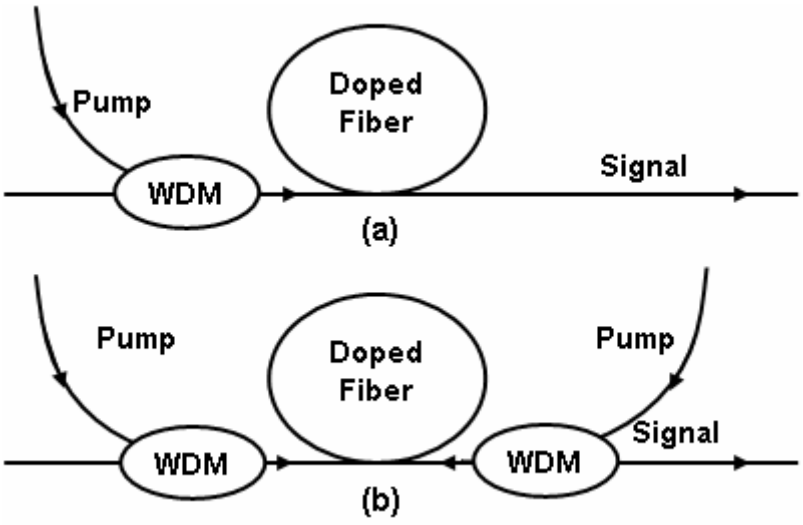

Figure 1.5: Fiber laser pumping schemes: (a) Unidirectional pumping (b) Bidirectional pumping.

Fiber lasers may be operated in continuous or pulsed regimes, and they are ideal for pulsed operation for several reasons. The extremely wide emission spectra of doped fibers allows for the amplification of pulses that are both short and wavelength-tunable [35]. A mode-locked fiber resonator may be constructed by splicing together optical components based on optical fiber technologies which reduce cost, alignment sensitivity and reliability over lasers based on bulk optical components. In this thesis, we study the operation of an ytterbium-doped fiber laser in both the pulsed and continuous wave regimes.

1.6: Dispersion

The speed of light propagation in a medium is dependent on its wavelength. For an optical pulse, consisting of multiple frequencies, the unequal propagation speed of each frequency component can lead to broadening of the pulse in the time domain. The propagation constant of a wave is defined as:

$$\beta(\omega) = \frac{2\pi n(\omega)}{\lambda} \tag{1.6.1}$$

Expanding equation 1.6.1 about the central frequency ω_0:

$$\beta(\omega) = \beta(\omega_0) + \frac{d\beta}{d\omega}(\omega - \omega_0) + \frac{1}{2}\frac{d^2\beta}{d\omega^2}(\omega - \omega_0)^2 + \frac{1}{6}\frac{d^3\beta}{d\omega^3}(\omega - \omega_0) + \ldots \tag{1.6.2}$$

The second order term in this expansion describes the pulse spreading due to the delay between each frequency (group delay) and is called the group velocity dispersion (GVD) parameter [13]. The *group velocity* is defined as the inverse of the derivative of the propagation constant with respect to angular frequency:

$$V_g = \frac{L}{\tau_g} = \left(\frac{\partial\beta}{\partial\omega}\right)^{-1} \tag{1.6.3}$$

Where τ_g is the group delay acquired per unit length. The broadened pulse duration following propagation in a dispersive medium may now be written in terms of the bandwidth and propagation distance:

$$\tau_P\big|_{z=L} = \delta\lambda \cdot L \cdot |D| \tag{1.6.4}$$

$$D = \frac{1}{L}\frac{d\tau_g}{d\lambda} = -\frac{2\pi c}{\lambda^2}\beta_2 \tag{1.6.5}$$

Another form of dispersion that can take place in optical fibers is called waveguide dispersion, which arises from the fact that a portion of the radiation in an optical fiber propagates in the cladding. The radiation in the lower index cladding travels at a faster speed than in the core, leading to further broadening of the pulse [13]. Although material and waveguide dispersion are intricately related, they may be calculated to a good approximation by considering each effect independently [36]. The total dispersion may then be found as the sum of the material and waveguide dispersion. By assuming the core and cladding indices to be wavelength independent the pulse spreading due to waveguide dispersion can be shown to be [13]:

$$\begin{aligned} \tau_P\big|_{wg} &= \delta\lambda \cdot \left|D_{wg}(\lambda)\right| \cdot L \\ &= \frac{n_2 \cdot L \cdot \Delta \cdot \delta\lambda}{c\lambda} \cdot V \cdot \frac{d^2(Vb)}{dV^2} \end{aligned} \tag{1.6.6}$$

The normalized propagation constant b and the parameter Δ are defined as:

$$\begin{aligned} b &= \frac{\beta^2/k^2 - n_2^2}{n_1^2 - n_2^2} \\ \Delta &= \frac{n_1 - n_2}{n_1} \end{aligned} \tag{1.6.7}$$

The dispersion described here is assumed to take place within a single-mode fiber and is referred as intramodal dispersion. Since the fiber laser cavity presented in this thesis is constructed from single mode fibers, it is only necessary to consider intramodal dispersion.

1.7: Self Phase Modulation

Within certain materials, or at high enough field strengths, it is possible for an induced polarization to exhibit a nonlinear dependence on the magnitude of the applied field. Under such conditions, the polarization is related to the applied field by [37]:

$$\vec{P} = \varepsilon_0 \left[\chi^{(1)} \cdot \vec{E} + \chi^{(2)} : \vec{E}\vec{E} + \chi^{(3)} \vdots \vec{E}\vec{E}\vec{E} + ... \right] \tag{1.7.1}$$

Here $\chi^{(j)}$ is a tensor value of rank j and represents the j^{th} order susceptibility. The second order nonlinear term vanishes for media consisting of symmetric molecules such as SiO_2, therefore, its contribution to nonlinear effects in fibers is zero. Frequency-independent changes in refractive index called the Kerr effect arise from the third order nonlinearity. The nonlinear refractive index is written as [9]:

$$\bar{n}\left(\omega, |E|^2\right) = n(\omega) + n_2 |E|^2 \tag{1.7.2}$$

Where n_2 is a constant known as the nonlinear index. One important consequence of the Kerr effect is self-phase modulation (SPM). The nonlinear phase-shift due to SPM imparted on a pulse field envelope $A(z,t)$ after a propagation distance z may be written as [37]:

$$\phi_{NL}(z,T) = |A(0,T)|^2 \cdot \gamma \cdot z_{eff} \tag{1.7.3}$$

$$A(z,T) = A(0,T) e^{i\phi_{NL}(z,T)}$$

The direct relation between the nonlinear phase shift and $|A(0,T)|^2$ means that the high intensity portions of the propagating pulse undergo a larger phase shift than the lower intensity parts. The resulting temporally varying phase in turn leads to a shift of the instantaneous frequency across the pulse profile, while leaving the temporal profile *A(0,t)* unchanged [37]. This can be seen mathematically by considering the example of a Gaussian pulse:

$$\begin{aligned}\delta\omega(T) &= -\frac{\partial\left|A(0,T)\right|^2}{\partial T}\cdot\gamma\cdot z_{eff} \\ &= \gamma\cdot z_{eff}\cdot\frac{2T}{\tau^2}e^{-\left(\frac{T}{\tau}\right)^2}\end{aligned} \tag{1.7.4}$$

Here z_{eff} represents an effective distance adjusted for the linear loss within the medium [37]. The instantaneous frequency $\omega(T)$ is red-shifted (negative chirp) for negative values of T in front of the pulse center and blue-shifted (positive chirp) at the rear of the pulse. The frequency shifting at the temporal edges of the pulse translates to the generation of new frequency components at the edges of the pulse spectrum. Therefore, the SPM acts to spectrally broaden the pulse. Figure 1.6 shows the spectrum of an initially unchirped 100 ps Gaussian pulse after experiencing SPM due to propagation within a single mode silica fiber (n_2~$2.6\cdot10^{-20}$ m^2/W [38]).

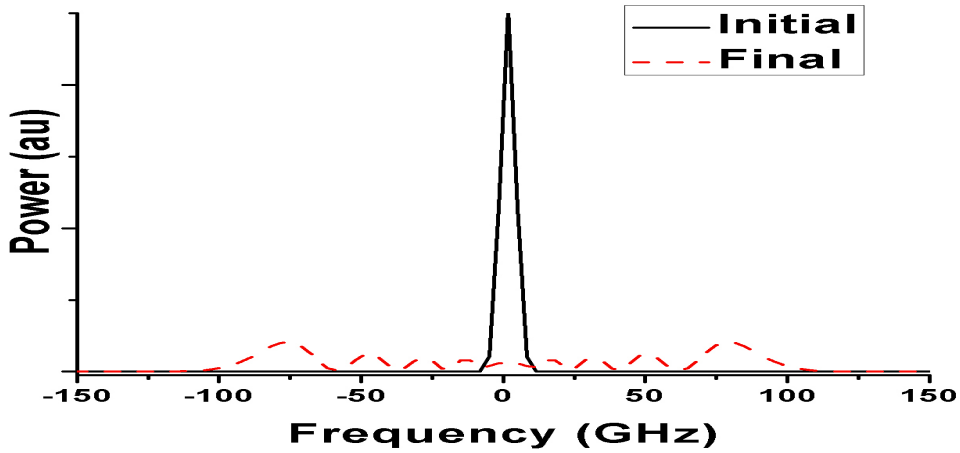

Figure 1.6: Self phase modulation-induced spectrum broadening of an initially unchirped 10W, 100 ps pulse following propagation through 1 km of single mode fiber (n_2~3·10^{-20} m^2/W, 8 µm core diameter, numerical aperture of 0.1).

Figure 1.6 shows that despite the relatively small value of n_2 for fused silica, SPM can have a considerable effect on a pulse of high enough intensity after propagation through a sufficient distance of fiber. Since pulses circulating within a pulsed fiber laser can have broad frequency bandwidths at peak powers of many watts, SPM is an extremely important effect to consider when designing a pulsed laser [35;39].

1.8: Mode-Locking

When multiple waves of different, evenly spaced frequencies are superimposed with a fixed phase relationship, they will interfere to form a single high amplitude pulse at values of time when the maxima of each wave occurs simultaneously [6]. This phenomenon is known as mode-locking, and results in the laser output being a periodic train of pulses. Figure 1.7 shows the temporal profile of 200 superimposed sine waves with a fixed phase compared with the same frequency components superimposed with the addition of a random phase. While irregular peaks in amplitude are present in the random

phase case, in the fixed phase case a single high amplitude peak is formed. The temporal width of these peaks is related to the inverse of the frequency range spanned by the superimposed modes and their repetition rate is equal to the frequency spacing between the modes [6]. This illustrates the fundamental concept behind mode-locking. The main challenge is in forcing the fixed phase relationship between the oscillating modes: this may be done either through the action of an externally controlled modulator (active mode-locking) or by a passive element such as a saturable absorber (SA) [40]. The present discussion will focus on passive mode-locking.

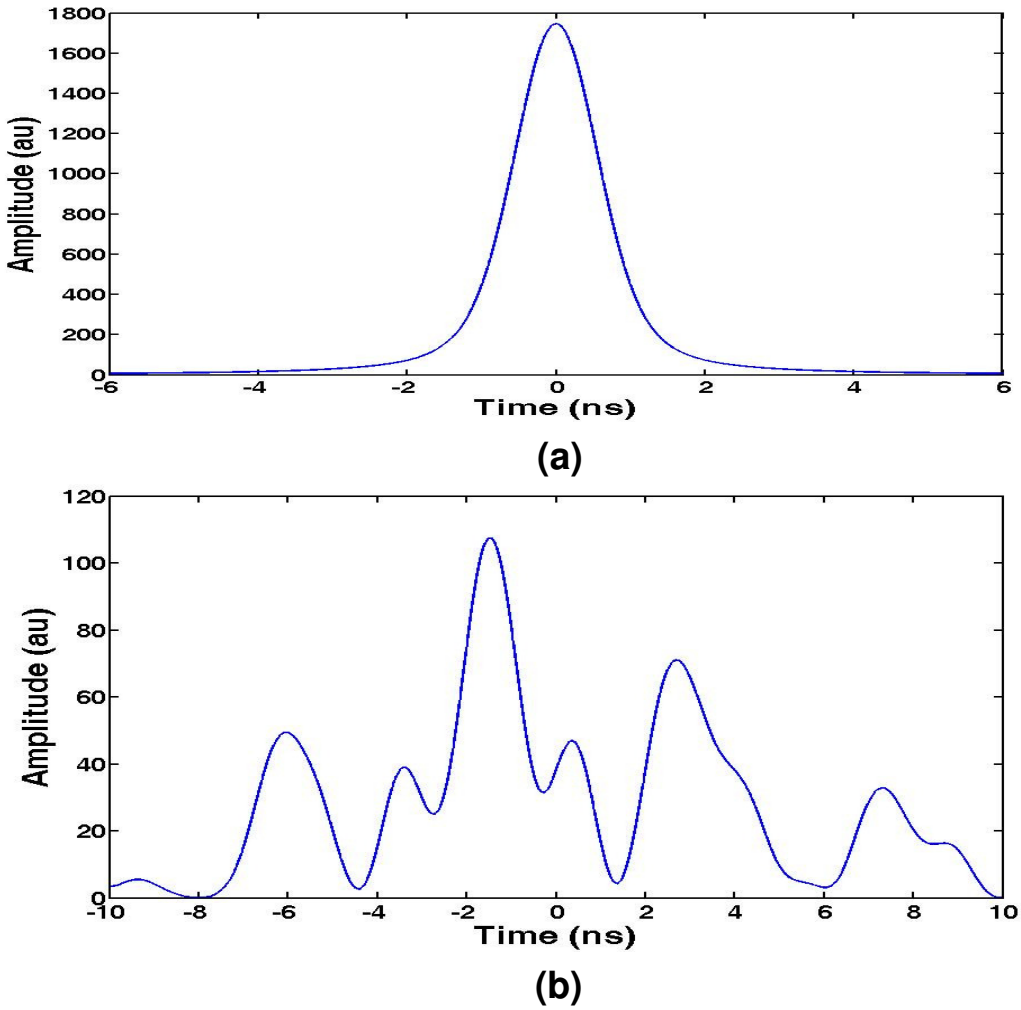

Figure 1.7: Temporal profile resulting from the summation of a Gaussian distribution of sine waves with frequencies equally spaced by 10 MHz spanning a frequency range of 2 GHz with: a) No relative phases, b) Random phase between 0 and 2π radians added to each wave.

1.9: Passive Mode-Locking

It is possible to convert the irregular fluctuations in amplitude (beating) of superimposed cavity modes into a single pulse by introducing an element with an intensity-dependent loss (saturable absorber) [41]. The SA induces a net loss on the low-intensity fluctuations that cannot saturate its absorption, while allowing a net gain for those with a high enough intensity to cause saturation. After many round-trips, the net loss leads to attenuation of the low-intensity beats, while the highest intensity beat is amplified into a pulse with high peak intensity. The steady state mode-locking condition is reached when the pulse energy and duration remains approximately constant after each round-trip [40].

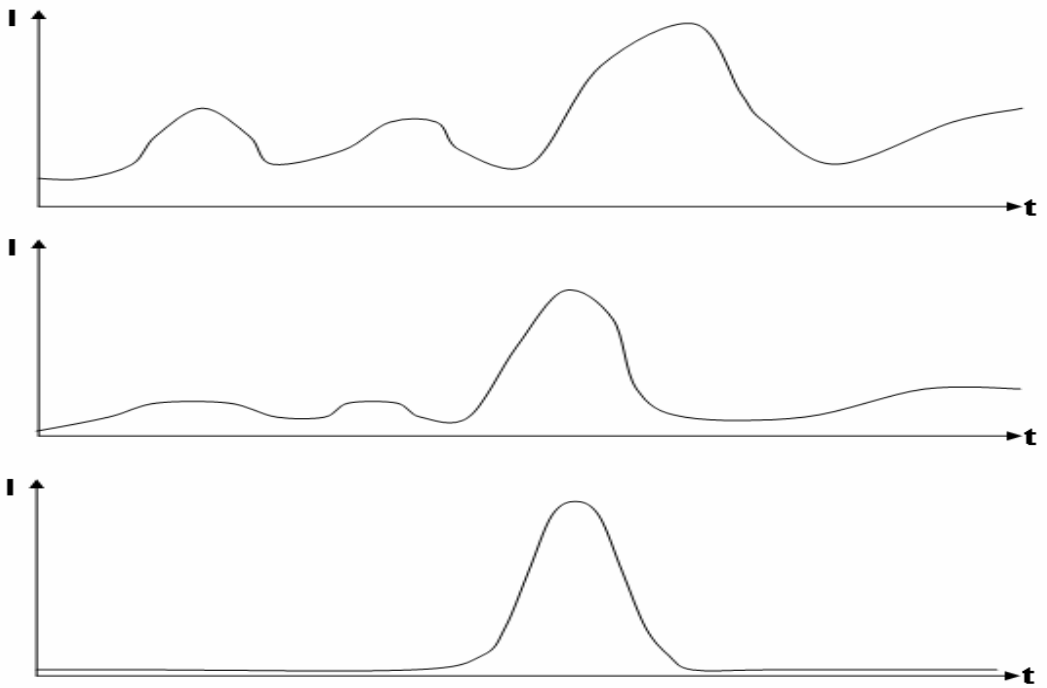

Figure 1.8: Formation of a mode-locked laser pulse from initial intensity fluctuations in a cavity containing a saturable absorber. The number of round-trips increases going downward.

Amplitude modulation by a saturable absorber is necessary to initiate and stabilize passive mode-locking, but the combined effects of Kerr nonlinearity and GVD can have significant effects on the circulating field pattern over many round-trips (especially in fibers). The spectral broadening due to SPM combined with the temporal broadening due to GVD can eventually lead a circulating pulse to break up into a quasi-continuous radiation pattern, preventing stable mode-locking [42]. The effect of saturable absorbers, SPM and GVD within a fiber laser cavity in the pulsed regime is discussed in more detail in the next chapter.

1.10: Q-Switching

Pulses may also be extracted from a laser cavity through a modulation of the resonator quality or "Q-factor". The Q-factor is defined as the ratio of the stored signal energy to the energy dissipated within the resonator per round-trip [6]:

$$\begin{aligned} Q &= \frac{\omega_0 \times E_{stored}}{E_{dissipated}} \\ &= \omega_0 T_{RT} \frac{1}{l} \end{aligned} \tag{1.10.1}$$

Where ω_0 is the central resonant frequency, T_{RT} is the resonator round-trip time, and l is the total intracavity losses. The oscillation within a low Q cavity is more strongly damped than in a high Q cavity. Therefore if the quality factor of a laser resonator is deliberately held at a low value by increasing cavity losses while the pump power remains constant then the laser oscillation and output will be suppressed. While the output is suppressed the upper level population increases and pump energy is stored in the gain medium. If the losses are then abruptly decreased for a short time, the stored

energy is released as the gain medium relaxes and is extracted from the cavity in the form of a pulse. Once the cavity loss returns to its initial large value, laser oscillation is again suppressed and the pulse ends.

The cavity loss modulation necessary to generate a Q-switched pulse may be induced by an active device such as an electro-optic [43] or acousto-optic [44] modulator. Another commonly employed method for active Q-switching for fiber lasers is to tune the reflected wavelength of a cavity-forming fiber Bragg grating on-and-off resonance with the other cavity grating. Since the cavity losses are related to the overlap between the reflection bands of the cavity forming reflectors, oscillation is suppressed in the off-resonance case [45]. It is also possible for a laser cavity to be passively Q-switched by a saturable absorber. The present study focuses on passive Q-switching.

1.11: Passive Q-Switching

Q-switching of a laser oscillator may be induced passively by introducing a saturable absorber into the cavity [46]. The passive Q-switching process as pump energy is stored in the gain medium in the form of an increasing excited state population [6]. As this is occurring, signal output from the laser remains quenched by the unsaturated saturable absorber. The excited state population within the saturable absorber eventually reaches a high enough value for it to become transparent to the signal radiation, at which time the stored energy in the gain medium is released over the course of one or more cavity round-trips. The pulse ends as the stored energy is dissipated and the saturable absorber relaxes, and the process repeats. Figure 1.9 shows how the gain, loss, and signal

power change with time in both an actively Q-switched and passively Q-switched laser [6].

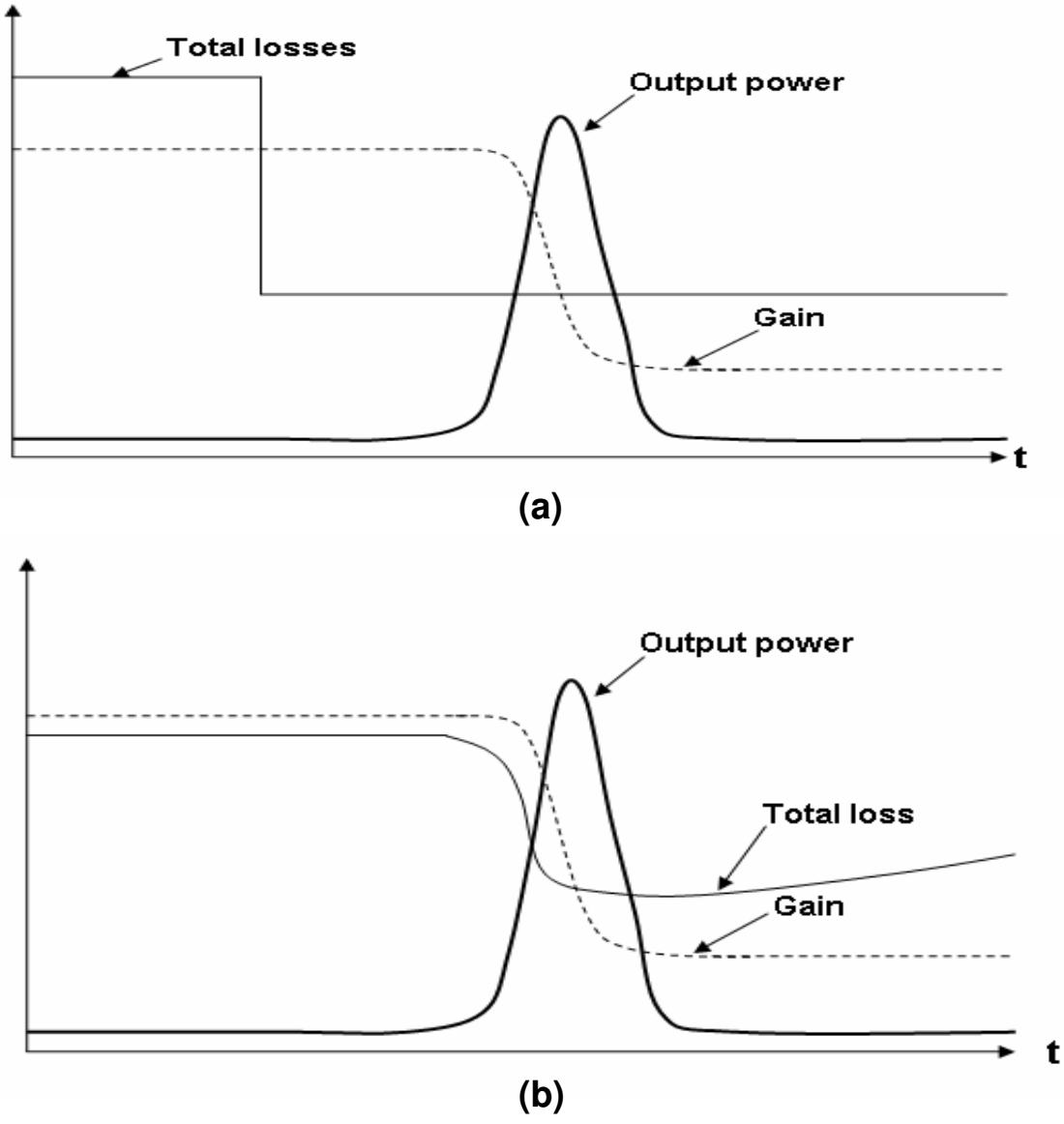

Figure 1.9: Total losses, gain and output power as functions of time in a) An actively Q-switched laser and b) A passively Q-switched laser. In the active case the active device abruptly reduces the cavity loss to allow the dissipation of a pulse, while in the passive case the saturable absorber is gradually bleached and then recovers over the course of the pulse cycle.

For the above to occur, it is necessary for the saturable absorber to saturate more quickly than the gain medium. This condition can be expressed mathematically as [47]:

$$\frac{\alpha_0 L_{SA}}{g_0 L_g} \cdot \frac{\sigma_{SA}}{\sigma_g} \cdot \frac{A_g}{A_a} \geq \gamma \qquad (1.11.1)$$

Where α_0 and g_0 are the small-signal SA absorption and gain medium gain coefficients, respectively, σ_{SA} and σ_g are the absorption and emission cross-sections of the SA and gain medium, L_{SA} and L_g are the lengths of the SA and gain medium, and A_g and A_{SA} are the effective mode areas within the gain medium and SA. The constant γ is known as the inversion reduction factor and is equal to 2 for three-level media [48].

A laser cavity containing a saturable absorber may operate in a simultaneously mode-locked and Q-switched regime. In this case, mode-locked pulses form at the start of the longer Q-switched "giant pulse", and the stored energy in the gain medium is dissipated by the shorter mode-locked pulses [49]. This leads to a series of pulse "bursts", consisting of mode-locked pulses repeating at the fundamental cavity frequency (or one of its harmonics) modulated by a longer Q-switched envelope (figure 1.12).

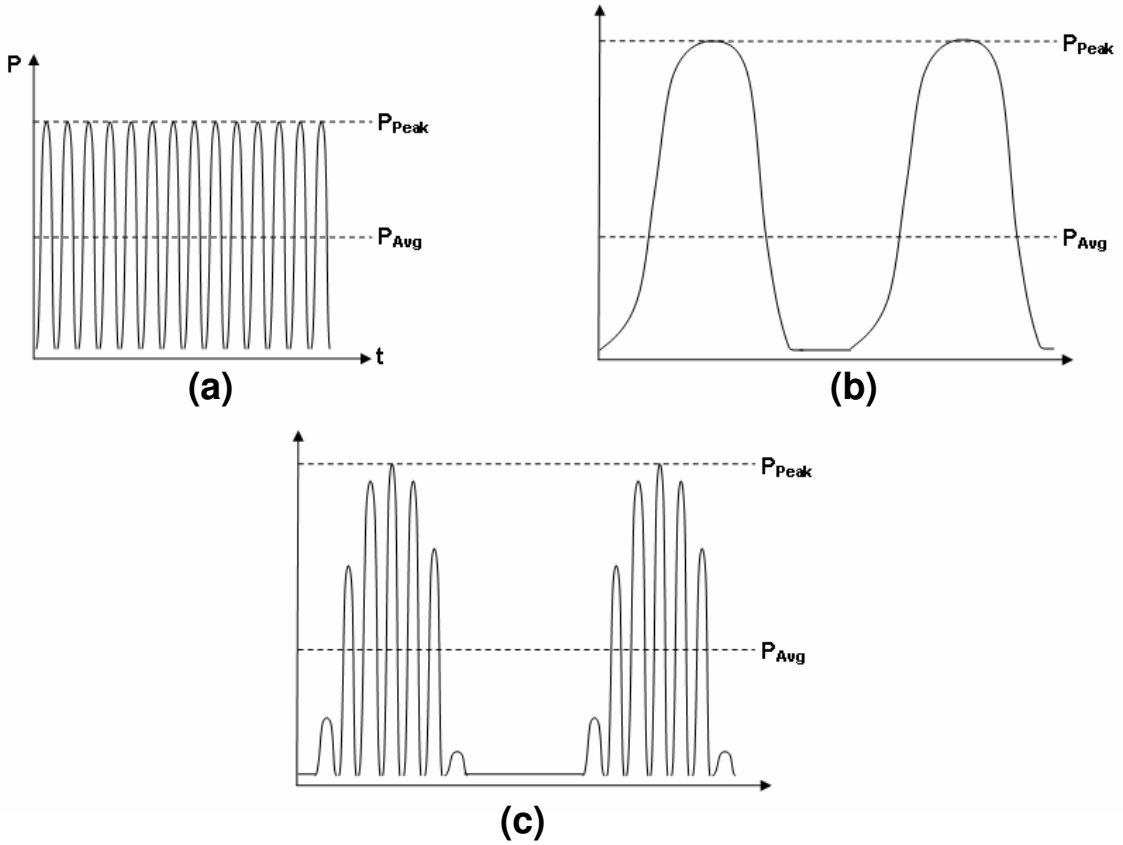

Figure 1.10: Comparison of a) CW mode-locked b) Q-switched and c) Q-switched mode-locked laser outputs.

Q-switched mode-locking (QML) allows for the generation of mode-locked pulses with much higher peak powers than in continuous-wave mode-locked lasers [50]. However, since the duration of the Q-switched envelope typically encompasses too few round-trip times for the mode-locked pulses to reach the steady state, their pulse duration and energy are often irreproducible from one pulse bunch to the next [51]. Steps are usually taken to avoid such "Q-switching instabilities" in mode-locked lasers for this reason. QML can be reasonably stable if the mode-locked pulses are not modulated to zero amplitude between each Q-switched pulse, since they do not grow from noise at the start of each burst. QML is typically observed in solid state lasers with gain media having long upper state lifetimes on the order of microseconds to milliseconds, since in these

systems the gain medium is unable to relax and adjust itself to changes in signal power that occur within one round-trip transit time or less [49]. An experimental study of Q-switched mode-locking in an ytterbium-doped fiber laser is described in the next chapter.

1.12: Organization of the Thesis

Chapter 2 describes an ytterbium-doped fiber laser emitting at 1064 nm. The effect of the samarium-doped fiber as a saturable absorber, pump power, and polarization state of the wave inside the cavity on the laser oscillation has been explored. The laser can operate in the continuous wave (CW), Q-switched mode-locked (QML) and continuous wave Q switched regimes.

Chapter 3 describes potential applications of the developed laser in sensing making use of gold nanorods as an intermediary. Relevant background information and early experimental results on the interaction of light-nanoparticle are discussed.

Chapter 4 summarizes the work.

Chapter 2

An Ytterbium-doped Fiber Laser

2.1: Introduction

Fiber laser technology is a promising alternative to other laser technologies by virtue of its performance and compactness. Erbium-doped fiber lasers emitting at 1.55 μm have become very important in optical communications. Advancements in the development of pump sources, pumping techniques and doped fiber fabrication have enabled high power, cladding-pumped, ytterbium-doped fiber lasers to generate peak powers in excess of 1 megawatt [52]. Pulses with durations of only tens of femtoseconds have been obtained directly from passively mode-locked fiber lasers, equaling many solid-state bulk mode-locked lasers [53].

Ytterbium-doped fiber lasers emitting near 1 μm are particularly attractive for applications in medicine [54]. The bulk lasers that are currently used in medicine are costly and require precise optical alignment [55]. A device based on fiber laser technology could present a more cost-effective and robust alternative. In addition, the wide gain spectrum (more than 100 nm) of ytterbium-doped fiber allows for wide

tunability of the laser emission wavelength, allowing a larger range of wavelengths to be exploited for the desired application.

In this chapter, we demonstrate an ytterbium-doped fiber laser operating in both the continuous wave (CW) and pulsed regimes. The cavity design is proposed, and the principles of operation of each of its components are described. A theoretical study of pulse formation in fiber lasers is presented. Finally, we show experimentally oscillation of the ytterbium-doped fiber laser in the CW, Q-switched mode-locked and Q-switched regimes.

2.2: Experimental Set-up

A schematic diagram of the fiber laser is shown in figure 2.1. One end of the laser resonator is terminated with a high reflecting (99.74% reflectance) fiber Bragg grating (FBG1) and the laser output is coupled out of the cavity through a lower reflecting (79.01%) fiber Bragg grating (FBG2) at the other end. Both FBGs have a Bragg wavelength of approximately 1064 nm and a reflection bandwidth of approximately 0.2 nm. A 2.5 m length of double-clad ytterbium-doped fiber (DCYDF, CorActive DCF-YB-8/128-P-FA) serves as the active medium. The gain fiber is pumped by a high power diode laser module emitting up to 25 watts of power at 976 nm. Pump radiation is coupled to the gain fiber via a multimode fused fiber coupler (MMFC). A fiber polarization controller (PC) is inserted to control the polarization of the wave in the cavity. An unpumped, samarium doped, single-mode fiber (SmDF, CorActive SM119) of length ~ 30 cm is spliced between the PC and FBG2 to act as a saturable absorber (SA). A polarization independent optical isolator (OI) was placed at each cavity output to

prevent Fresnel reflections from the fiber ends from re-entering the laser resonator. The total estimated cavity length is ~14 m.

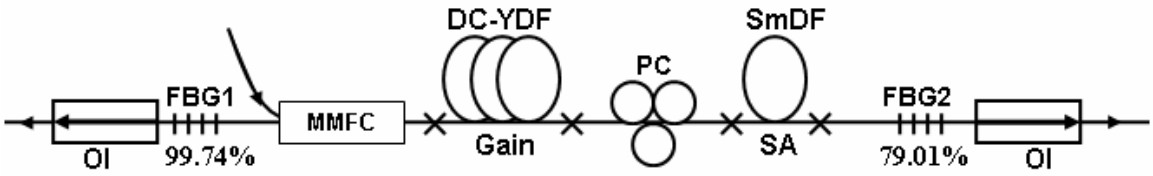

Figure 2.1: Schematic diagram of the fiber laser.

The laser output from the high reflecting FBG1 output end was monitored using an optical spectrum analyzer (OSA) with 1.25 GHz resolution, and the output from FBG2 was monitored with both an optical power meter, and a high speed InGaAs photo-detector (PD) with a maximum rise/fall time of 100 ps and an oscilloscope. The PD enabled us to measure the temporal profile of the laser output on a short time scale, allowing its transition between continuous-wave and pulsed operation to be observed.

2.3: Double-Clad Ytterbium-Doped Fiber

A double-clad, ytterbium-doped fiber (DCYDF) acts as the gain medium in our fiber laser. A cross-section of the DCYDF is shown in figure 2.2: it consists of a circular core (8 μm diameter) made of silica glass doped with trivalent ytterbium ions (Yb^{3+}) surrounded by a 128 μm wide octagon-shaped silica inner cladding. The inner cladding is enclosed by a circular outer cladding.

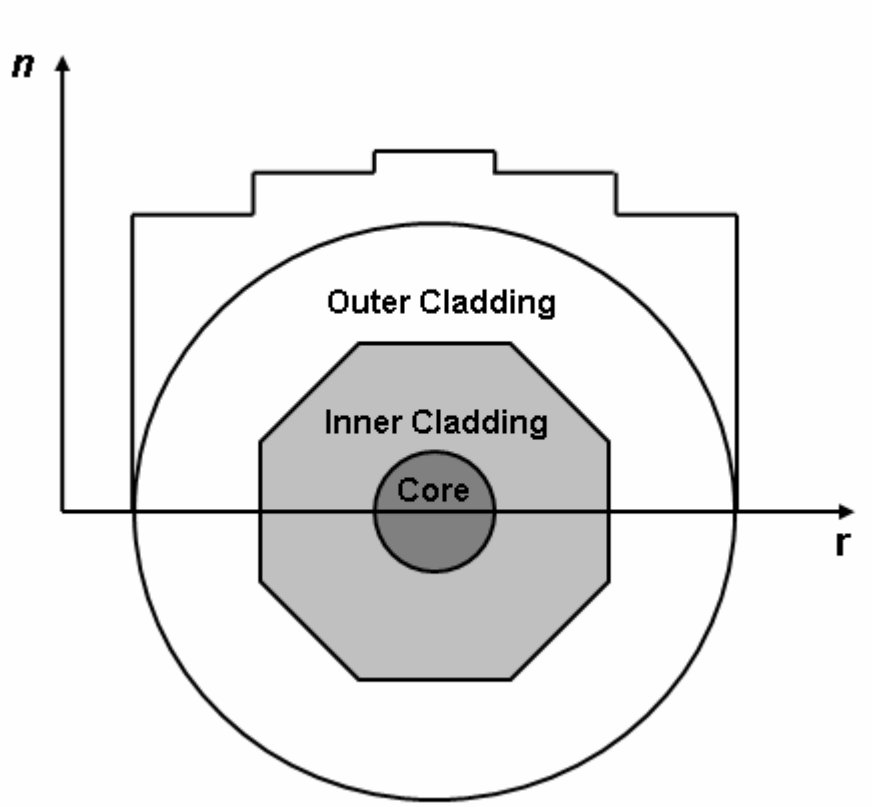

Figure 2.2: Cross-section and refractive index profile of a double-clad fiber with an octagonal inner cladding [56].

The double-clad geometry increases the coupling efficiency of the pump radiation into the fiber and thus improves the laser output power. An inexpensive multimode pump laser with high output power may therefore be used as a pump source [57] In these cladding-pumped lasers the pump radiation propagates within both the cladding and core, being absorbed by the dopant ions in the core. The signal radiation generated by stimulated emission from the dopant ions, however, remains confined within the core and is coupled out of the laser as a near-diffraction limited beam in a single transverse mode [56]. In this way, the highly divergent and low brightness pump radiation from the pump laser is converted to a high quality beam at the signal wavelength. Improvements in available pump power and fiber fabrication have enabled the CW output power from a

single ytterbium-doped fiber laser to be scaled all the way up to 10 kW [56] and pulsed ytterbium-doped fibers with megawatt peak power have been reported [52].

The Yb^{3+} ion possesses a number of emission transitions within the 950 – 1100 nm wavelength range. Furthermore, the homogeneous and inhomogeneous broadening of these transitions within a glass host leads to a wide and continuous emission spectrum in the 1 micron band [58] (figure 2.3). .

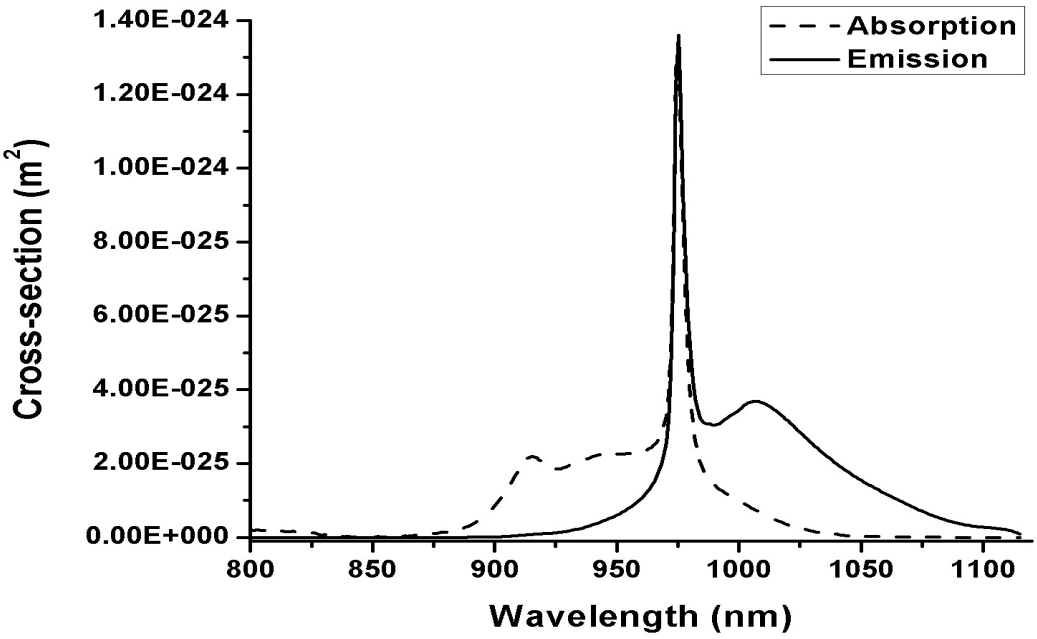

Figure 2.3: Absorption (dashed) and emission (solid) spectra of ytterbium-doped phosphosilicate glass fiber (obtained from CorActive Canada).

The broadened absorption and emission transitions that make up the above spectrum occur between sublevels of the ground and first excited states of Yb^{3+} whose degeneracy has been lifted due to the *Stark effect*. The electronic configuration of triply-ionized ytterbium is **[Xe] $4f^{13}$**. This gives the following values for the orbital, spin and total angular momentum quantum numbers:

$$L = 3$$
$$S = 1/2$$
$$J = 5/2, 7/2$$

Applying Hund's rules gives the term symbols $^2\mathbf{F_{7/2}}$ for the ground state and $^2\mathbf{F_{5/2}}$ for the excited state [7]. In the absence of an external perturbation, each of these states further consists of ***2J+1*** degenerate (equal energy) angular momentum states, corresponding to the allowed values of $\boldsymbol{m_j}$. The degeneracy of these states may be lifted through the application of an external electric field, turning each set of degenerate states into a *manifold* of Stark levels. The external field polarizes the atom and then interacts with the resulting dipole moment according to the interaction potential $V_{\text{int}} = -\vec{\mu} \cdot \vec{E}$ [59]. Since the interaction is dependent on only the magnitude of $\boldsymbol{m_j}$, each manifold will then consist of ***J+½*** Stark levels. For the case of Yb^{3+}, this means that the $^2\mathbf{F_{7/2}}$ ground state manifold is split into four Stark levels and the $^2\mathbf{F_{5/2}}$ excited state is split into three Stark levels. It has been shown that absorption transitions between each of these manifolds occur from the lowest energy ground state Stark level, terminating on each of the three excited state Stark levels (figure 2.4) [60;61], while the fluorescence transitions begin at the lowest energy $^2\mathbf{F_{5/2}}$ Stark level and terminate on each of the $^2\mathbf{F_{7/2}}$ Stark levels. These three absorption lines and four emission lines are then homogeneously and inhomogenously broadened due to their presence in an amorphous glass host, forming continuous absorption and emission spectra (figure 2.3).

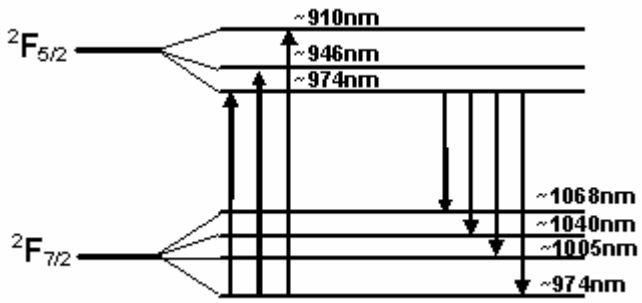

Figure 2.4: Stark levels and absorption and fluorescence transitions for Yb^{3+}. The transitions are labeled on the terminating energy level with the absorbed or emitted photon wavelength. Values for the absorbed or emitted wavelengths obtained from [61].

The field applied to the Yb^{3+} ions is highly dependent on the glass host composition as well as any co-dopants and their concentrations. It is therefore possible to control both the transition wavelengths as well as the transition strengths to a large degree by altering these properties [62]. A large number of ytterbium-doped glasses are now available commercially in both bulk and fiber form. The gain fiber in our laser is drawn from ytterbium-doped phosphosilicate glass (CorActive Canada).

2.4: Fiber Bragg Gratings

Permanent modifications in the refractive index of crystals and glasses are known to occur upon exposure to high energy radiation [63]. By spatially varying such refractive index changes along the length of an optical fiber, it is possible to produce a device capable of reflecting light propagating within the core. These devices, which are known as fiber Bragg gratings (FBGs) are now widely available and have found extensive application in communication and sensing of strain and temperature. The fabrication of high performance FBGs has also been critical to the development of improved fiber lasers.

The refractive index of a material is dependent upon a variety of factors including temperature, material density, phase (crystalline or amorphous), and the molar refractivity. Irradiation by light of a suitable frequency and intensity can modify these properties by causing the formation of colour centers (vacancy defects in the material lattice) or densification [64]. These alterations are widely accepted to occur by means of two-photon absorption at visible frequencies followed by dissipation of the absorbed energy into the glass matrix. Excitation through single-photon absorption is also possible at ultraviolet frequencies [65], decreasing the irradiance and exposure time necessary to induce a permanent refractive index change.

Bragg reflection gratings may be produced by spatially modulating the induced refractive index change. This is achieved by setting up an interference pattern within the fiber core. Prolonged exposure to the interference pattern leads to perturbations of the refractive index at the interference maxima, the magnitudes of which are dependent on the intensity and wavelength of the interfering beams, the exposure time and the fiber core composition [64]. The resulting refractive index grating reflects light within a narrow range of frequencies through successive scattering events at each index change.

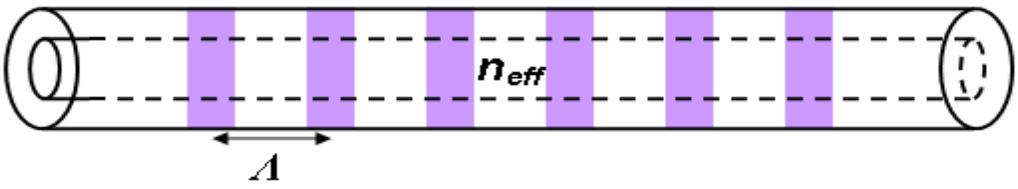

Figure 2.5: Schematic diagram of a fiber Bragg grating. Λ: grating period, n_{eff}: effective core index.

The wavelength of maximum reflection (Bragg wavelength) from the index grating is dependent on the period of the refractive index perturbation Λ and the effective modal index n_{eff} in the fiber core:

$$\lambda_B = 2\Lambda n_{eff} \tag{2.4.1}$$

The strength of the grating, or the reflectivity, depends primarily on the amplitude of the index perturbation and the grating length. In a single mode fiber, the reflectivity at the Bragg wavelength is related to these, as well as the fiber parameters, as follows [9;66]:

$$R(\lambda_B, L) = \tanh^2\left(\frac{2\partial n}{\lambda}\eta L\right) \tag{2.4.2}$$

Where L is the grating length, δn is the magnitude of the index perturbation and η is the modal overlap factor. Even an extremely weak refractive index perturbation can produce a grating of high reflectivity when the multiple reflections are compounded over the entire grating length: for δn = 0.0001 and η = 1, a reflectivity of 90% is calculated from equation 2.4.2. Because they can be fabricated with an arbitrary reflectivity at any wavelength, FBGs are ideal for application as fiber laser cavity reflectors.

2.5: Polarization Controllers

A method for controlling the polarization state of light propagating within a fiber is vital for achieving optimal CW or pulsed laser operation, given its fundamental importance in phenomena such as interference taking place within a laser cavity. Due to their amorphous nature, glasses such as fused silica are optically isotropic and possess no natural birefringence. Therefore, to produce the birefringence necessary to alter and control the polarization of a wave propagating within a silica fiber, an optical anisotropy must be imposed by some means [67]. This may be done by deforming the circular core cross-section so that it becomes elliptical in shape, or through the application of external electric or magnetic fields [68]. Birefringent fibers can also be produced by introducing elliptical or circular shaped stress elements on opposite sides of the core (see figure 2.6). These fibers, known as PANDA fibers, have achieved the highest birefringence and lowest loss with minimal changes in the polarization state of propagating light over long transmission distances [69].

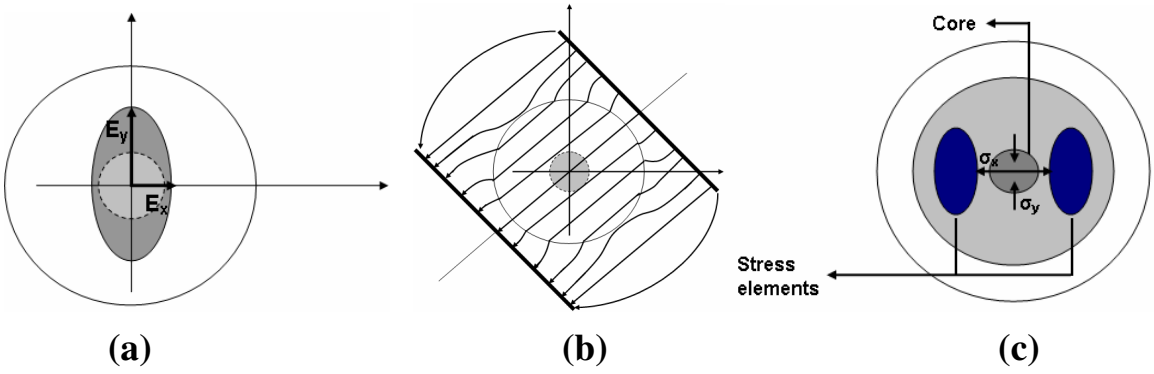

Figure 2.6: Methods of inducing birefringence in fibers a) Elliptical core fiber. b) External field. c) PANDA type fiber.

A birefringence may also be induced within the core of a standard single-mode fiber through bending and twisting [70;71]. Bending the fiber results in a longitudinal stress that is compressive on the side facing the center of curvature and tensile on the opposite side of central axis of the fiber (figure 2.7). This stress gradient results in a lateral stress in the radial direction being exerted on the inner layers by the outer layers [70]. The lateral stress produces the core birefringence.

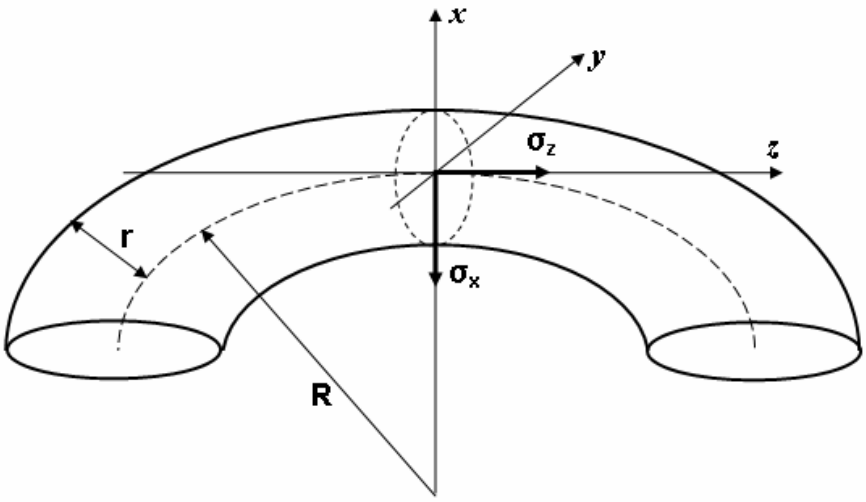

Figure 2.7: Schematic diagram of a bent fiber. R: radius of curvature measured from the center of curvature to the neutral axis, r: radius of the fiber, σ_x: stress in the *x*-direction, σ_y: stress in the *y*-direction.

The total stress is calculated by integrating the stress applied to an infinitesimal section of the fiber across the entire cross-section. The non-uniform strain (physical deformation) of the core is then found from the stresses in the *x* and *y*-directions, which induces a shift in the permittivity of the core in each direction via the photoelastic effect [67]. The refractive index change along each direction and therefore the fiber

birefringence may then be related straightforwardly to the elastic constants and bending radius of the fiber [71]:

$$\delta n = \Delta n_x - \Delta n_y = \tfrac{1}{4}(p_{12} - p_{11})(1+\nu)\left(\frac{r}{R}\right)^2 \cdot n^3 \qquad \text{at } x=0 \qquad (2.5.1)$$

The birefringence δn, although small, will cause light propagating through sufficiently long lengths of bent fiber to incur a considerable phase delay between its x and y polarized components. This phase delay allows each of the fiber loops to act as a fractional waveplate, depending on the length of bent fiber. A quarter wave plate is constructed by choosing a loop radius "R" and a number of loops "N" such that the total delay is equal to $\pi/2$, and a half wave plate for a total delay of π:

$$\text{Quarter wave:} \qquad \frac{2\pi}{\lambda}(N \cdot R)_{Q.W.} \cdot \delta n = \frac{\pi}{2} \qquad (2.5.2)$$

$$\text{Half wave:} \qquad \frac{2\pi}{\lambda}(N \cdot R)_{H.W.} \cdot \delta n = \pi$$

By suitably combining quarter and half-wave plates, and carefully adjusting these plates, it is possible to convert any given input polarization state into an arbitrary output state. Combining a quarter-wave plate, half-wave plate and a second quarter-wave plate in series enables such control over polarization: the two quarter-wave plates facilitate control over the ellipticity of the output polarization, while the half-wave plate allows for rotation of the polarization through an arbitrary angle [71]. This wave-plate combination may be straightforwardly implemented in fiber form by combining three rotatable drums

in series. Fiber is wound around each drum an appropriate number of times in order to induce a phase retardance of $\pi/2$ in the first loop, π in the second loop and $\pi/2$ again in the third loop, effectively producing a $\lambda/4, \lambda/2, \lambda/4$ sequence of birefringent wave-plates [71]. The orientation angle of each plate may furthermore be adjusted by changing the angle of each drum with respect to the vertical (figure 2.8).

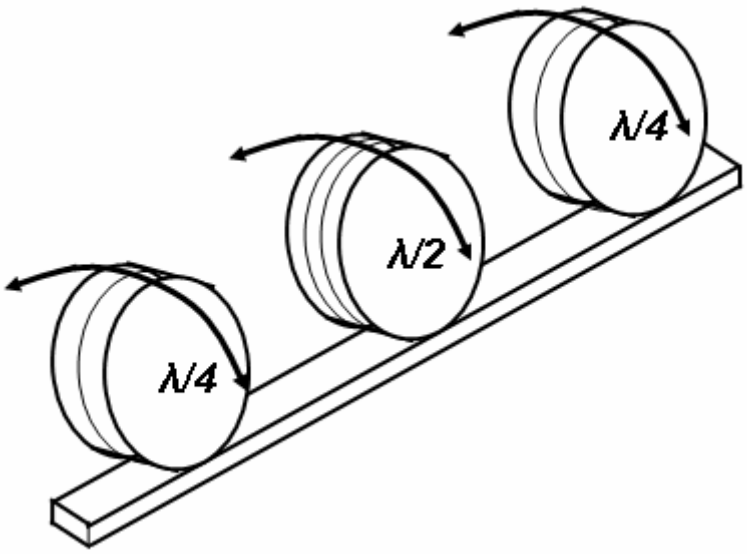

Figure 2.8: Schematic diagram of a fiber Polarization controller.

A fiber polarization controller of the above described type is incorporated into our laser cavity to control the polarization of the waves circulating within the cavity.

2.6: Saturable Absorbers

It is possible for light to experience an intensity-dependent transmission through or reflection from a medium by exciting atomic or molecular transitions or other nonlinearities. Such media are known as saturable absorbers (SAs). Bulk crystals [72],

semiconductor mirrors [73], dyes [74] and doped fibers [75] have all found application as real SAs taking advantage of resonant absorption.

Saturation occurs as an increasing number of absorbing atoms or molecules within the SA medium are excited to an upper level by incident signal photons. As the signal intensity and therefore the upper state population increases, the probability of a photon interacting with an absorber in the ground state decreases, leading to a reduced absorption coefficient within the medium. The saturation intensity is defined as the signal intensity that reduces the absorption coefficient to half its small signal value [6]:

$$I_{sat} = \frac{h\nu}{\sigma\tau_{eff}} \tag{2.6.1}$$

The effects that may take place within a saturable absorber when subjected to EM radiation, as well as the properties of the Samarium-doped fiber that functions as a saturable absorber within our laser are discussed in this section.

2.6.1: Pulse Shaping in Saturable Absorbers

A temporally varying optical field will experience a temporally varying absorption when it propagates through a saturable absorber (SA). Under the assumption of uniform saturation along the propagation direction, the change in the absorption coefficient due to saturation when a SA is subjected to an optical field *A(t)* may be described by a rate equation [76]:

$$\frac{dq(t)}{dt} = -\frac{q - q_0}{\tau_A} - q\frac{|A(t)|^2}{E_A} \tag{2.6.2}$$

Where q_0 is the initial, unsaturated absorption exponent. If $A(t)$ describes the temporal profile of an optical pulse, the solution of equation 2.6.2 may be used to obtain the profile following transmission through the SA. In general, a SA tends to shorten a pulse and alter its shape. This occurs because the lower intensity portions at the beginning and end of the pulse experience a higher loss and are thus more strongly absorbed than the pulse center, which is able to saturate the absorption. The manner in which the pulse profile changes following transmission is also dependent to a large degree on the length of the recovery time τ_a of the absorber [77]. An important distinction may be drawn between fast saturable absorbers in which the relaxation time is much shorter than the pulse duration, and slow absorbers where τ_a is comparable to or much longer than the pulse duration. For the fast case, the fact that τ_a is negligible compared with the time interval under consideration means that the time-dependence of q may be described by the steady state solution of equation 2.6.2:

$$q(t) = \frac{q_0}{1 + \frac{|A(t)|^2}{P_{sat}}} \tag{2.6.3}$$

For a slow absorber, τ_a is allowed to approach infinity in equation 2.6.2, resulting in a saturation dependent on the total integrated pulse energy [78]:

$$q(t) = q_0 e^{-\int |A(t)|^2 dt \,/\, E_{sat}} = q_0 e^{-E(t)/E_{sat}} \qquad (2.6.4)$$

Figure 2.9 compares the temporal profiles of a 10 ps with a peak power of $100P_{sat}$ pulse following transmission through both slow and fast saturable absorbers with small-signal transmission $T_0=exp(-q_0)$ of 10%. These plots show the differing saturation effects that can take place in fast and slow absorbers at high peak powers. While the fast absorber shortens the pulse by evenly attenuating both pulse wings (due to its ability to recover instantaneously), the slow absorber is bleached by the pulse front and subsequently unable to recover before the rest of the pulse passes. As a result, the pulse front is very strongly absorbed while the end of the pulse is left almost unchanged. This leads to both a reduction in pulsewidth and a temporal shift of the peak [77].

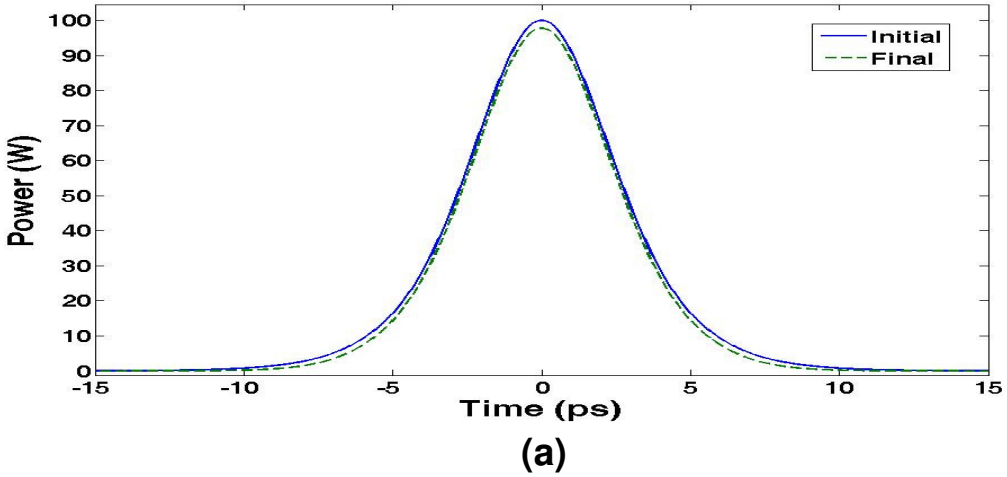

(a)

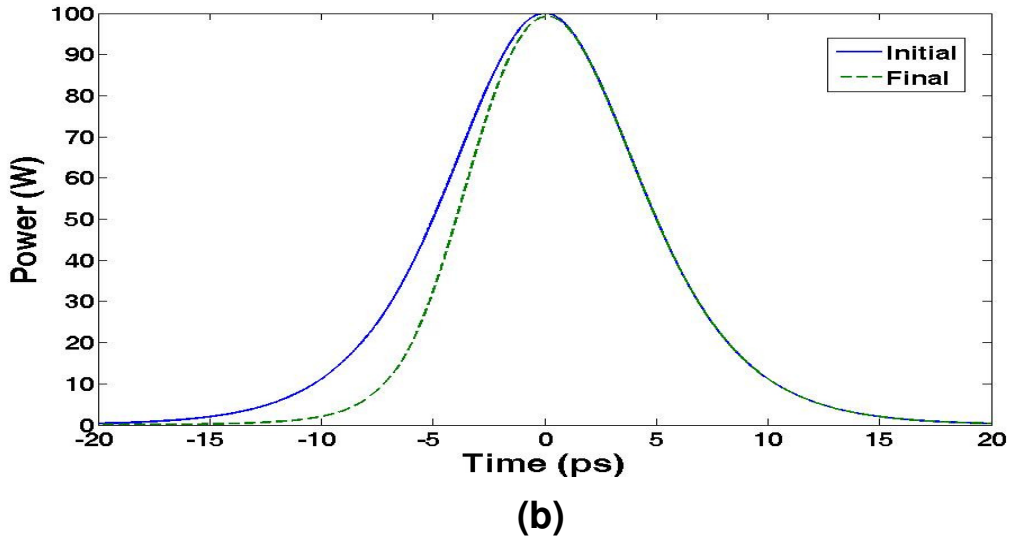

Figure 2.9: Action of saturable absorbers on a 10 ps pulse with $P_0=100P_{sat}$. a) Fast absorber b) Slow absorber.

The pulse shaping action of a saturable absorber is also highly dependent on the peak power of the pulse [6]. If the power is too low no saturation and therefore no pulse shaping may take place, while if the power is too high, then the entire pulse profile bleaches the saturable absorber and there is also no pulse shaping. This means that for a given value of q_0 there exists an optimum input peak power for the strongest pulse shaping.

The above described pulse-shaping effects performed by a saturable absorber are essential for both the formation and stabilization of mode-locked pulses within a laser resonator[40]. The absorber serves to both induce a negative net gain for noise preceding and following the circulating pulse and shorten the pulse to balance pulse broadening effects such as dispersion [41]. Figure 2.10 shows the gain and loss for a cavity containing a saturable absorber as functions of time following the passage of a pulse. For the case of both a fast and slow saturable absorber, the pulse opens a net gain "window" which closes after the absorber recovers [79]. To prevent the break-up of the pulse into an

unstable radiation pattern due to the growth of ASE noise within the post-pulse gain window, the window must be sufficiently short in comparison to the pulse duration. Numerical studies have shown that pulses can be stabilized by absorbers with a recovery time as much as an order of magnitude longer than their duration [76]. This is due to the temporal delay undergone by a pulse propagating within a cavity with a slow SA: each round-trip, the delayed pulse is able to incorporate the trailing radiation that developed within the gain window. A numerical study on the effect of SA properties on pulsed oscillation of an ytterbium-doped fiber laser is detailed in section 2.8.

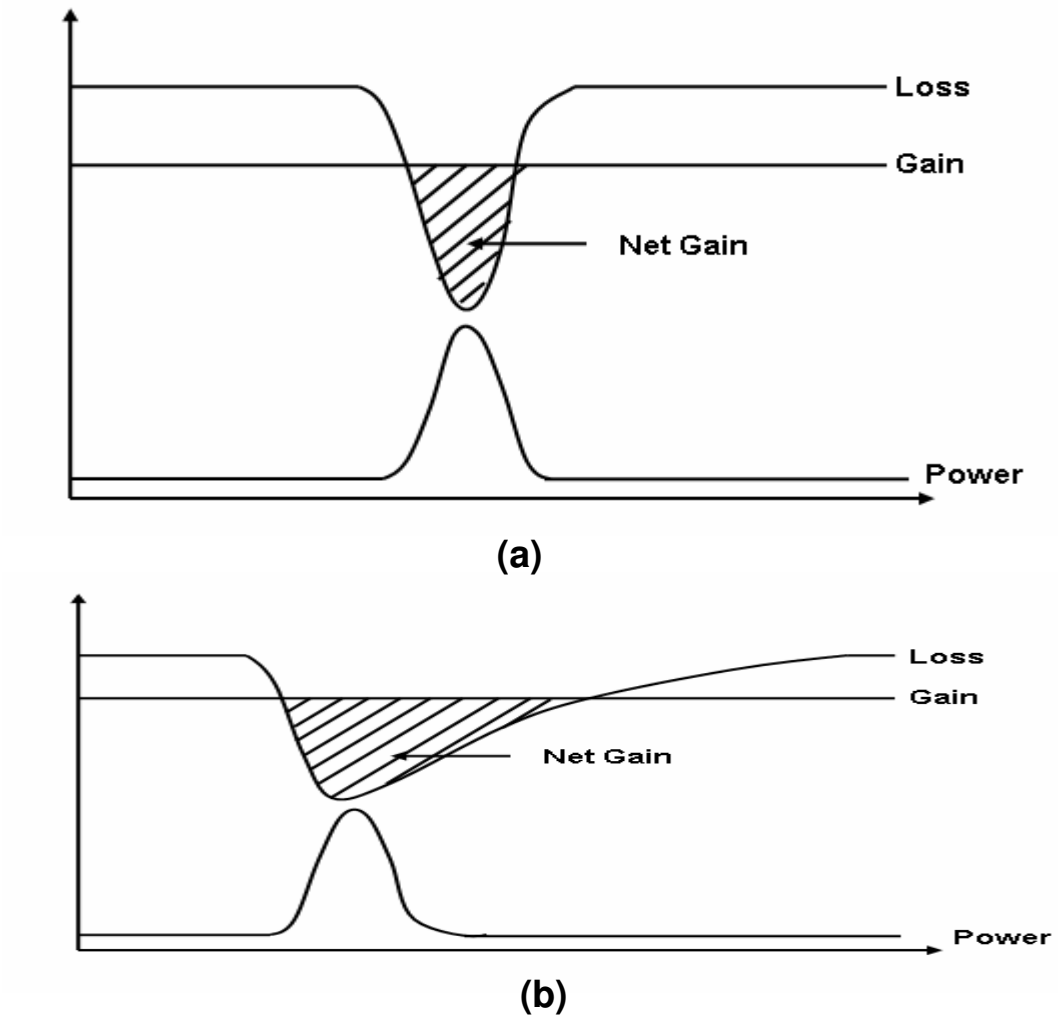

Figure 2.10: Gain, loss and pulse power as functions of time for a) A fast saturable absorber; the gain is saturated at its steady state value. b) A slow saturable absorber [77].

2.6.2: Transient Gratings in Saturable Absorbers

In addition to its role in starting and sustaining passive mode locking and Q-switching, a saturable absorber can support the formation of dynamic reflection gratings when it is host to counter-propagating, interfering EM waves [80]. The standing wave pattern formed by the interfering waves leads to spatial variation in light intensity, which in turn leads to a non-uniform excitation of the dopant ions. The resonant absorption by dopant ions within the interference pattern maxima modifies the imaginary portion of the complex susceptibility of the medium, which subsequently leads to a change in the real susceptibility (and therefore refractive index) due to the intrinsic link between the two as described by the Kramers-Kronig relations [81;82]. As a result, a periodic refractive index variation develops within the absorber medium which acts as a resonant reflection grating by the same mechanism as the permanently written FBGs described in section 2.4. The Bragg wavelength of this grating is equal to the wavelength of the counter-propagating writing beams, and its reflectivity is dependent upon the intensity of the writing beams, the length of the absorbing medium, and the concentration of the absorbers within the medium [83].

The formation of the dynamic grating and reflection of light from it may be understood as a type of four wave mixing process, in which two counter-propagating pump waves interfere to form the dynamic grating and subsequently interact with a third signal wave. The interaction of the pump and signal waves in turn generates a fourth wave, which propagates in the opposite direction of the original signal wave [84]. Each of these waves with frequency $\omega_{p,s}$ and wavenumber $k_{p,s}$ may be written as [85]:

$$
\begin{aligned}
E_p^{(+)}(z,t) &= A_p^{(+)}(z)e^{i(\omega_p t - k_p z)} \\
E_p^{(-)}(z,t) &= A_p^{(-)}(z)e^{i(\omega_p t + k_p z)} \\
E_s^{(+)}(z,t) &= A_s^{(+)}(z)e^{i(\omega_s t - k_s z + \varphi)} \\
E_s^{(-)}(z,t) &= A_s^{(-)}(z)e^{i(\omega_s t + k_s z + \varphi)}
\end{aligned}
\tag{2.6.5}
$$

Where the subscripts *p* and *s* denote pump and signal waves, and the superscripts *(+)* and *(-)* denote forward and backward propagating waves, and φ is the relative phase between the pump and signal waves. The interference of the pump waves first sets up a standing wave field distribution along the *z*-direction, which induces a spatially varying polarization within the medium, modifying its susceptibility [6]. The intensity-dependent susceptibility can be approximated as $\chi''(\omega,z) = \chi''(\omega) - I(z)/I_{sat}$ for low writing beam intensities [6]. Substituting this and equations 2.6.5 into the standard wave equation allows a set of coupled wave equations to be derived for the forward and backward propagating pump and signal waves. For the pump waves in a medium with unsaturated absorption coefficient α_0, these take the form:

$$
\begin{aligned}
\frac{dA_p^{(+)}}{dz} &= \alpha_0\left(1 - \frac{I_p^{(+)} + I_p^{(-)}}{I_{sat}}\right)A_p^{(+)} - \alpha_0 \frac{A_p^{(+)}A_p^{(-)*}}{I_{sat}}A_p^{(-)} \\
&= \alpha' A_p^{(+)} - \kappa A_p^{(-)}
\end{aligned}
\tag{2.6.8}
$$

$$
\frac{dA_p^{(-)}}{dz} = -\alpha' A_p^{(-)} + \kappa^* A_p^{(+)} \tag{2.6.9}
$$

For the signal waves, the coupled equations describe both the interaction between the forward and backward propagating waves as well as their interaction with the index grating written by the pump waves:

$$\frac{dA_s^{(+)}}{dz} = \alpha' A_s^{(+)} - \kappa A_s^{(-)} e^{i(2\Delta kz-\varphi)} \tag{2.6.10}$$

$$\frac{dA_s^{(-)}}{dz} = -\alpha' A_s^{(-)} + \kappa^* A_s^{(+)} e^{-i(2\Delta kz-\varphi)} \tag{2.6.11}$$

Where $\Delta k=k_s-k_p$ is the difference between the wavenumbers of the pump and signal waves. Solving equations 2.6.10 and 2.6.11 with the boundary conditions $A_s^{(+)}(0)=1$ and $A_s^{(-)}(L)=0$ gives the forward and backward propagating signal wave amplitudes as a function of distance z along the saturable absorber [86]:

$$A_s^{(+)} = -e^{i(\Delta kz-\varphi)}\left\{\frac{(\alpha'-i\Delta k)\sinh S(z-L) + S\cosh S(z-L)}{(\alpha'-i\Delta k)\sinh SL - S\cosh SL}\right\} \tag{2.6.12}$$

$$A_s^{(-)} = -e^{-i(\Delta kz-\varphi)}\left\{\frac{\kappa\sinh(z-L)}{(\alpha'-i\Delta k)\sinh SL - S\cosh SL}\right\} \tag{2.6.13}$$

$$S^2 = \left[i\Delta k - \alpha'\right]^2 - \left|\kappa\right|^2$$

With these expressions, we can finally obtain the reflectivity of the transient grating:

$$
\begin{aligned}
r &= \frac{A_s^{(-)}(z=0)}{A_s^{(+)}(z=0)} \\
&= \frac{\kappa \sinh SL}{(\alpha' - i\Delta k)\sin SL - S\cosh SL} \\
R &= |r|^2
\end{aligned}
\tag{2.6.14}
$$

Equation 2.6.14 describes the dependence of the transient grating reflectivity on the signal wavelength, writing beam intensity, saturable absorber length, and absorption coefficient (dopant concentration) of the saturable absorber. This enables the reflectivity to be plotted and optimized with respect to each variable [86]. Figure 2.11 shows the reflection spectrum and plots of reflectance as functions of saturable absorber length and absorption coefficient for an average writing beam power equal to $0.3P_{sat}$, assuming no initial relative phase φ between the signal and writing waves. Figures 2.11 b) and c) show asymptotic behaviour with respect to the SA length and absorption coefficient. This is expected in both cases due to saturation at constant writing power; increasing the length or absorption coefficient at constant power beyond the saturated value does not yield an increased reflectivity.

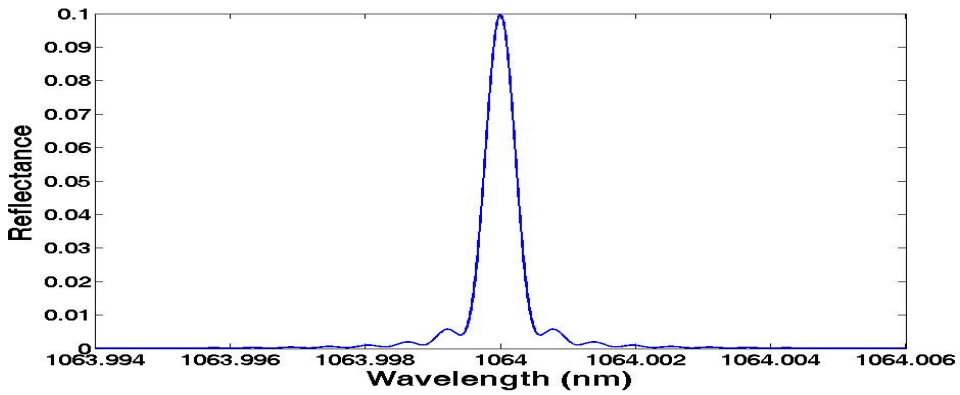

(a)

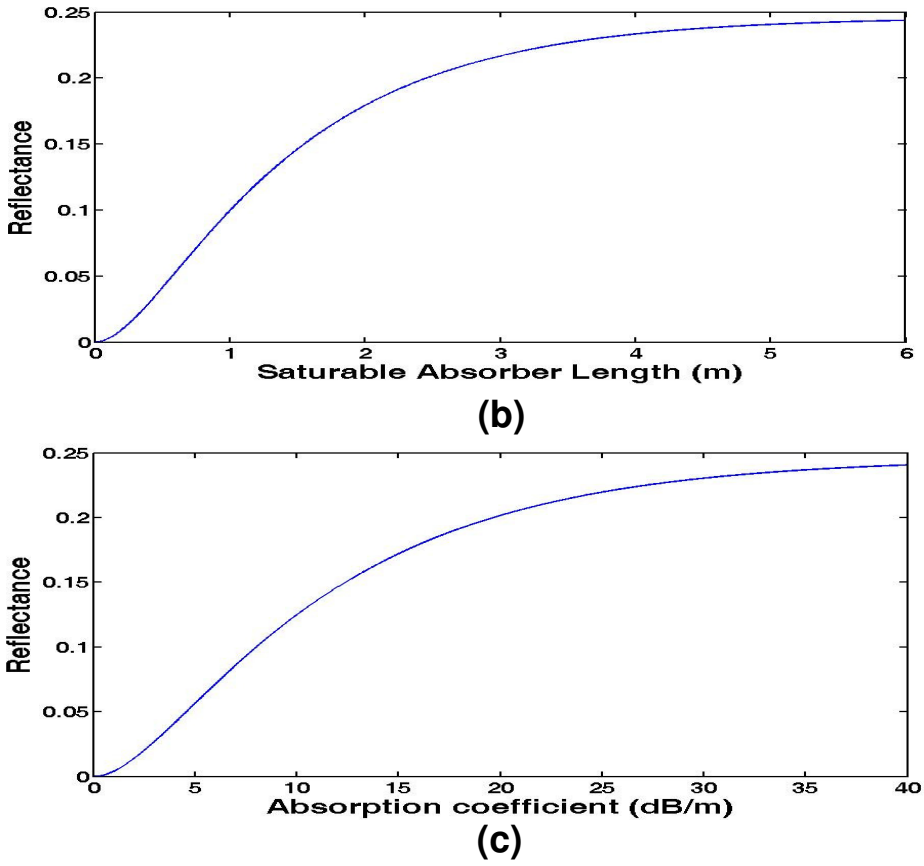

Figure 2.11: Reflectance plots for a transient grating at a writing wave power equal to $0.3P_{sat}$. a) Reflection spectrum. b) Reflectance as a function of saturable absorber length. c) Reflectance as a function of absorption coefficient.

The reflection bandwidth also exhibits a dependence on the above described parameters. It is inversely related to the saturable absorber length, and also varies slightly with writing power and absorption coefficient. The bandwidth is expressed analytically as [85]:

$$\delta\nu\big|_{FWHM} = \frac{c}{2nL_{SA}}\left\{1+\frac{|\kappa|^2 L_{SA}^2}{\pi^2+(\alpha' L)^2}\right\}^{1/2} \tag{2.6.15}$$

Which in the limit of low writing power approaches the value $\delta\nu\big|_{FWHM} = c/2nL_{SA}$.

2.6.3: Samarium-Doped Fiber as Saturable Absorber

In our laser, a length of unpumped single mode silica fiber doped with trivalent samarium (Sm^{3+}) functions as a saturable absorber. The attractiveness of Sm^{3+} as a saturable absorber for a laser cavity may be seen from an examination of its ground state electron configuration, which is **[Xe] $4f^5$**. The five unpaired electrons result in a large number of possible states that are closely separated in energy (figure 2.12). The diversity of states enables a large number of possible excitation transitions, giving rise to a spectrum consisting of distinguishable broadened absorption lines when Sm^{3+} is placed within a glass host (figure 2.13).

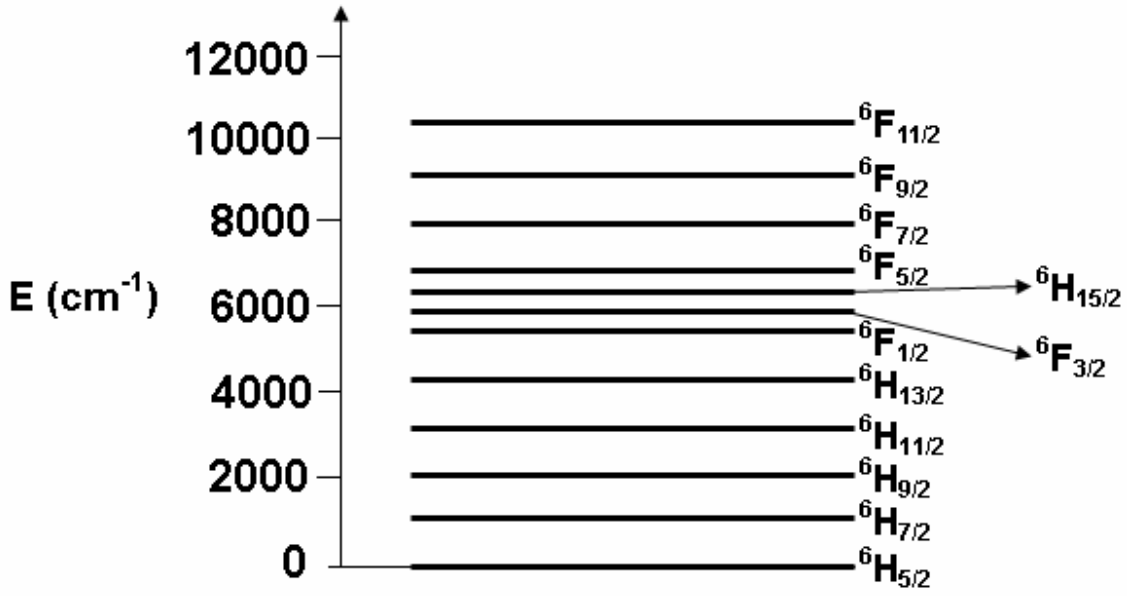

Figure 2.12: Energy level diagram of Sm^{3+} (adapted from [87]).

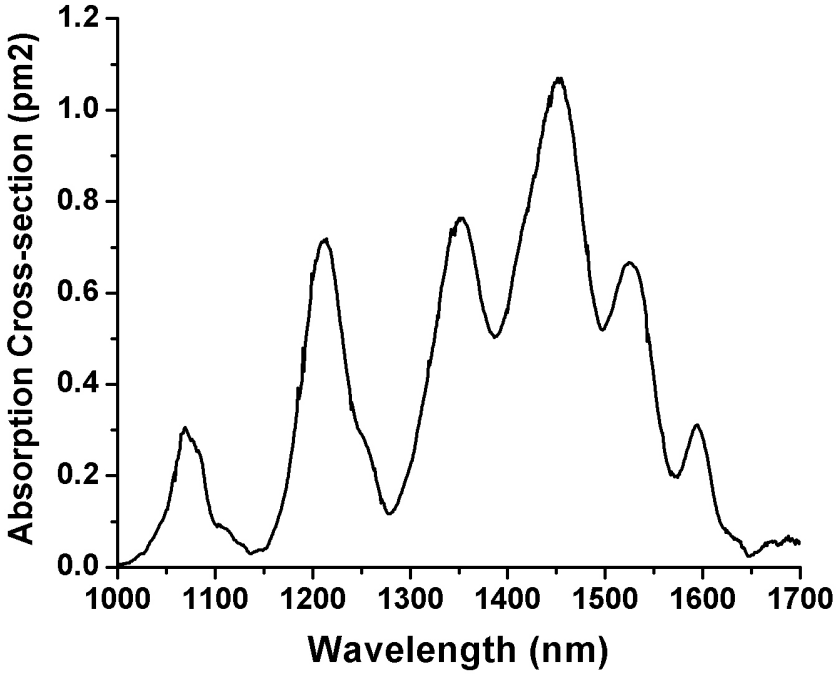

Figure 2.13: Absorption spectrum of Sm^{3+} in silica glass fiber (obtained from CorActive Canada).

As is evident from figure 2.13, the energy levels of the Sm^{3+} are separated by energy gaps of less than 2000 cm^{-1}. It has been shown that non-radiative processes dominate when relaxation from energy levels spaced this close occurs [88]. These relaxations are mediated via the emission of phonons with energy equal to the gap between the adjacent energy levels. When an ion is excited to a high-energy (from $^6H_{5/2}$ to $^6F_{11/2}$, for example) state via photon absorption it will relax back to the ground state via the emission of multiple phonons, transitioning between each level separating the ground and excited state and emitting a phonon at each step. Since a single phonon relaxation event can take place on a time scale of picoseconds to hundreds of picoseconds, the relaxation time for Sm^{3+} from the excited state is expected to be 1 ns or less [87]. One study measured a switching time of less than 5 ns for a 10 ns pulse launched into a length of Samarium-doped fiber (SmDF). It was noted by the authors of this study that the

accuracy of their measurement was limited by the available instruments and that the true response time should be lower than this value [87].

Using the cross-section data and the fiber parameters obtained from the manufacturer, the saturation energy and power of the saturable absorber fiber may be estimated. At the laser operating wavelength of 1064 nm, the absorption cross-section is 0.261 pm^2. The 6.5 μm core diameter and numerical aperture of 0.14 give a mode-field radius of 3.33 μm, and the overlap factor between the mode-field area and the total Sm^{3+} doped area is 0.425686. Using these values, and a 5 ns relaxation time, the saturation energy and power of the saturable absorber are calculated to be:

$$\begin{aligned} E_{sat} &= \frac{h\nu_s}{\sigma_a(\nu_s)} \cdot A_{SA} \cdot \Gamma \\ &= \frac{1.867\times10^{-19} J}{2.61\times10^{-25} m^2} \cdot \pi(3.33\times10^{-6} m)^2 \cdot 0.425686 \\ &\cong 10.6\mu J \end{aligned} \tag{2.6.16}$$

$$P_{sat} = \frac{E_{sat}}{\tau_{SA}} \cong 2120W$$

Given the relaxation time of ~1.35 ms for Yb^{3+} in phosphosilicate glass, emission cross-section of ~0.105 pm^2 and core area of ~50 μm^2 we may also calculate the saturation energy and power of the gain medium at the signal frequency:

$$\begin{aligned} E_{sat} &= \frac{h\nu_s}{\sigma_g(\nu_s)} \cdot A_g \\ &\cong 89.4\mu J \end{aligned} \tag{2.6.17}$$

$$P_{sat} = 66.2mW$$

The condition 1.11.1 (Section 1.9) for passive Q-switching can be rewritten in terms of the gain and SA saturation energies as:

$$\frac{\alpha_0 L_{SA}}{g_0 L_g} \cdot \frac{E_g}{E_{SA}} \geq \gamma \qquad (2.6.18)$$

The dependence of the left side of relation 2.6.18 on E_g/E_{SA} means that E_{SA} compares favourably with the gain saturation energy for achieving Q-switched operation. Q-switching in fiber lasers using doped fiber saturable absorbers is an established technique for producing high energy nanosecond to microsecond duration pulses [75]. Samarium-doped fibers in particular have been used as a passive Q-switching element for both ytterbium-doped fiber lasers oscillating at ~1064 nm [89] and erbium-doped fiber lasers oscillating at ~1550 nm [90]. These lasers have produced pulses with durations of ~650 ns and ~450 ns, respectively. A Q-switched fiber laser with a samarium-doped fiber saturable absorber has also been demonstrated using a two-core, double-clad ytterbium doped gain fiber. The two core geometry serves to induce a birefringence within the gain fiber and maintain the polarization of the laser output [91]. In this work a length of single-mode samarium-doped fiber is inserted into the laser cavity to induce passive Q-switching. The Q-switched mode of operation is detailed in section 2.9.

The high saturation power of the samarium-doped fiber saturable absorber means that the transient grating response of the SmDF described earlier is extremely weak for

practical values of intracavity power; a peak reflectance of less than 0.1% is calculated from equation 2.6.14 for a writing power of 100 W. Despite this, it is well known that even small back-reflections can have a considerable effect on the output spectrum of a laser oscillator [92]. Transient grating effects are thus expected to influence the observed spectrum of our laser when it oscillates in the continuous wave regime.

2.7: Passive Resonator

A linear Fabry-Perot laser resonator has been chosen in this study. The cavity is formed between the high-reflecting FBG1 and the lower-reflecting output coupler FBG2. A schematic diagram of a linear Fabry-Perot cavity is shown in figure 2.14.

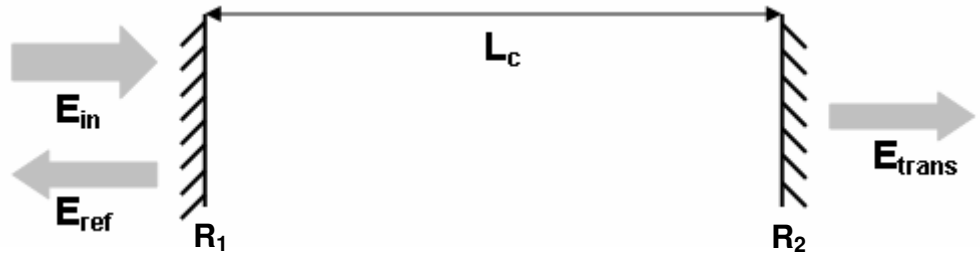

Figure 2.14: Schematic diagram of a linear Fabry-Perot (FP) cavity. E_{in}: incident field. E_{ref}: reflected field. E_{trans}: transmitted field.

Waves entering the cavity at one end will experience a frequency-dependent reflection or transmission. Frequencies which incur a total phase of 2π in a single round-trip are in resonance with the cavity and are transmitted, while frequencies that experience a round-trip phase of π are anti-resonant and are reflected. The frequency-dependent transmission and reflection may be written as [9]:

$$\frac{I_{out}}{I_{in}} = \left|\frac{E_{out}}{E_{in}}\right|^2 = \frac{(1-R_1)(1-R_2)}{1-2\sqrt{R_1R_2}\cos 2kL_c + R_1R_2} \tag{2.7.1}$$

$$\frac{I_{ref}}{I_{in}} = \left|\frac{E_{ref}}{E_{in}}\right|^2 = \frac{R_1 - 2\sqrt{R_1R_2}\cos 2kL_c + R_2}{1-2\sqrt{R_1R_2}\cos 2kL_c + R_1R_2} \tag{2.7.2}$$

In addition to the main cavity formed between the two FBGs, a second and third sub-cavity can be present during laser oscillation due to the dynamic reflection grating written by counter-propagating waves within the SA [84]. These cavities are enclosed by the transient grating within the SA and each of the FBGs, and their lengths are equal to the total length of fiber spliced between the ends of the SA and each reflector (figure 2.15 a). The sub-cavity formed between the transient grating and FBG2 may be treated as a mirror with a complex reflectivity equal to the field reflection function of a FP cavity formed by mirrors with reflectivity r_{SA} and r_2 (figure 2.15 b). The reflectivity function of the complete compound cavity may then be determined as that of a cavity enclosed by FBG1 and the effective mirror.

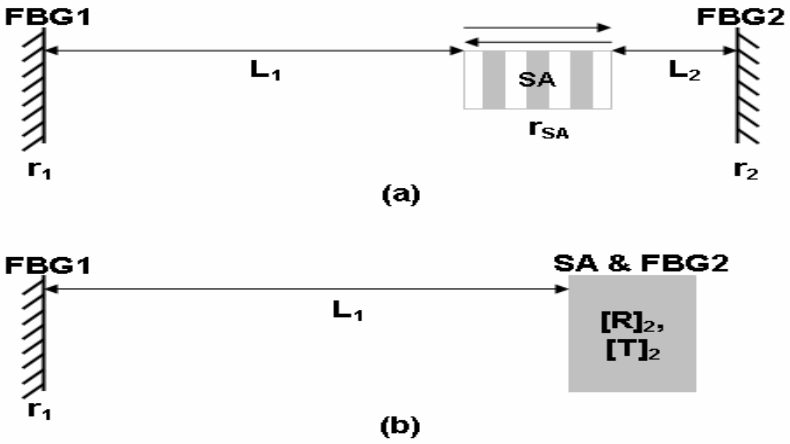

Figure 2.15: Sub-cavities formed by the FBGs and the saturable absorber transient grating: a) Cavity with FBGs and transient grating. b) Resonator in which cavity 2 is represented as an effective mirror.

The reflectivity and transmission of the effective mirror are:

$$[R]_2 = \frac{r_{SA} - r_2 e^{-2ikL_2}}{1 - r_{SA} r_2 e^{-2ikL_2}} \tag{2.7.3}$$

$$[T]_2 = \frac{t_{SA} t_2 e^{-ikL_2}}{1 - r_{SA} r_2 e^{-2ikL_2}} \tag{2.7.4}$$

Equations 2.7.3 and 2.7.4 may be substituted into the expression for the transmission through a Fabry-Perot cavity in order to obtain the intensity transmitted through the compound cavity:

$$\frac{I_{out}}{I_{in}} = (1-R_1)(1-R_2)(1-R_{SA}) \times \left\{ \begin{array}{l} 1 + R_{SA}R_2 + R_1R_{SA} + R_1R_2 - 2\sqrt{R_{SA}R_2}(1+R_1)\cos 2kL_2 - \\ 2\sqrt{R_1R_{SA}}(1+R_2)\cos 2kL_1 + 2\sqrt{R_1R_2}(1+R_{SA})\cos 2kL_1 \cos 2kL_2 + \\ 2\sqrt{R_1R_2}(1-R_{SA})\sin 2kL_1 \sin 2kL_2 \end{array} \right\}^{-1} \tag{2.7.5}$$

Minimizing the denominator of equation 2.7.5 yields the following two phase conditions for optimum transmission through the cavity:

$$\begin{aligned} k_n L_1 &= n\pi \\ k_m L_2 &= (2m+1)\frac{\pi}{2} \end{aligned} \tag{2.7.6}$$

In addition, optimum transmission at each resonant peak requires that both conditions 2.7.6 are satisfied at the same frequency:

$$\begin{aligned} & k_m = k_n \\ & \Rightarrow \frac{L_1}{L_2} = \frac{2n}{2m+1} \end{aligned} \tag{2.7.7}$$

If L_2 is set to be small compared to L_1, then $m<<n$, and condition 2.7.7 can be reduced to the following simple condition for optimal overlap between the transmission maxima of each cavity:

$$L_1 \cong \frac{2}{3} n L_2 \tag{2.7.8}$$

Figure 2.16 shows the longitudinal mode structure for the passive, compound cavity. It can be seen that the transmission spectrum of the low FSR, higher finesse cavity is modulated by the reflection spectrum of the higher-FSR, low finesse cavity formed by the transient grating and FBG2. This serves to reject a large number of the low-FSR cavity longitudinal modes.

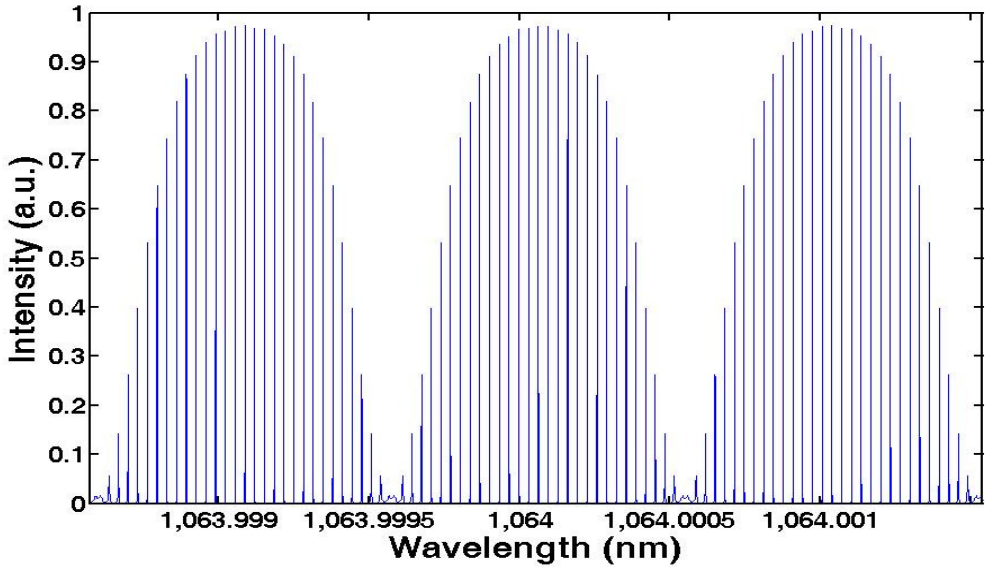

Figure 2.16: Longitudinal mode structure of the cavity with a transient grating that is written by strong waves at each individual wavelength. L_1=12m, L_2=0.4m, L_{SA}=1m.

The above described modulation of the longitudinal mode structure is only expected to take place during CW operation of the laser. Although it has been shown that dynamic gratings may be recorded in doped fibers by counter-propagating, interfering pulses [93], this may only occur if there are multiple pulses travelling in the cavity that can interfere with each other, or if a pulse is long enough to be reflected from a cavity end reflector and then interfere with itself. Because of this fact, we expect the laser to operate in either a CW state in which the longitudinal mode structure is influenced by the transient grating in the saturable absorber, or in a separate Q-switched mode-locked or Q-switched state. These distinct regimes of operation, as well as the conditions for transitioning between them, are discussed in section 2.9.

The close separation of the low-FSR cavity modes means that a very large number of longitudinal modes may oscillate within the reflection bandwidth of the FBGs. With proper adjustment of the conditions within the laser cavity, it is possible to force a

fixed phase between these modes to produce a short passively mode-locked pulse. The pulsed regime of a laser oscillator is discussed in detail next.

2.8: Pulse Formation in Ytterbium-Doped Fiber Lasers: Theory

2.8.1: Background

A series of numerical simulations were performed to understand the effect of the intracavity fiber length, gain, loss and the saturable absorber characteristics on mode-locked pulse formation and propagation in an ytterbium-doped laser. Each of the effects considered in the simulations are discussed here.

The oscillating radiation in a mode-locked laser cavity is influenced by the amplifying medium, the saturable absorber medium, group velocity dispersion (GVD), self phase modulation (SPM) due to Kerr nonlinearity and a frequency bandwidth-limiting element over the course of each round-trip. The bandwidth limitation could be imposed by the finite width of the active medium gain spectrum, or through another spectral filter such as a cavity mirror with a frequency-dependent reflection. It is also possible for additional anomalous dispersion to be present in the cavity. Chirped fiber Bragg gratings [1], sections of microstructured fiber [94] and grating pairs [95] are some of the techniques used to introduce anomalous dispersion. If each effect can be considered to have a small effect on a pulse per cavity round-trip, then the pulse evolution may be described by the so-called master equation of mode-locking [40]:

$$T_R \frac{\partial}{\partial T} A(T,t) = \left(-iD \frac{\partial^2}{\partial t^2} + i\delta |A|^2 \right) A(T,t) + \left(g - l + D_{g,f} \frac{\partial^2}{\partial t^2} - q(T,t) \right) A(T,t) \qquad (2.8.1)$$

$$D_{g,f} = \frac{1}{\Delta\omega_{g,f}{}^2}$$

$$\delta = \gamma L = \frac{2\pi n_2}{\lambda_0 A_{eff}} L$$

Where t is a short-term time variable describing the pulse profile on a time scale on the order of the pulse duration and T is a long term time describing the evolution of the pulse across many cavity round-trips. T_R represents the cavity round-trip time, D is the group velocity dispersion and $D_{g,f}$ is the "filter dispersion" arising from either the gain bandwidth or some other bandwidth limiting element. The non-linear phase-shift due to Kerr nonlinearity per round-trip is represented by δ. Finally, g and q are the saturated gain and loss (respectively) and l represents the other nonsaturable cavity losses. The master equation considers each effect to act on the field profile $A(T,t)$ simultaneously, describing its evolution according to the long term time T. The steady state pulse profile is the solution to equation 2.8.1 that remains unchanged with T [40]. Equation 2.8.1 was first developed by H. A. Haus to describe mode-locking by fast saturable absorbers analytically [96]. Analytical descriptions of mode-locking by slow saturable absorbers [78] and artificial saturable absorbers utilizing Kerr nonlinearity followed [97]. These models were originally developed in the context of conventional bulk or dye lasers in which the assumption of simultaneous and weak shaping of a pulse by each effect is valid [40]. However, large fluctuations in the pulse profile can occur in fiber lasers with long cavity lengths due to their higher dispersion and nonlinearity [42], limiting the applicability of previously developed analytical models. A numerical approach is chosen for this reason.

We first consider the effect of saturable absorption. In our own laser cavity, the saturable absorption is provided by a length of samarium doped fiber, with a nanosecond-order recovery time [87]. A SA with nanosecond recovery time can act as a slow absorber for sub-nanosecond pulses, while for pulses of nanosecond or greater duration the slow absorber approximation (equation 2.6.4) may not be accurate. Therefore, the exact solution of equation 2.6.2 is employed to model the saturable absorption in the simulation:

$$q(t) = \frac{q_0}{f(t)}\left[\frac{1}{\tau_{SA}}\int f(t)dt + 1\right] \tag{2.8.2}$$

$$f(t) = \int\left[\frac{1}{\tau_{SA}} + \frac{|A(T,t)|^2}{E_{SA}}\right]dt$$

The above expression is numerically integrated via the trapezoidal rule within the simulation to obtain the saturated absorption coefficient as a function of time. The pulse profile following transmission through the saturable absorber is then calculated as $A'(T,t) \approx A(T,t)e^{-q(t)}$.

The next pulse-shaping mechanism considered in the simulation is the combined effect of self-phase modulation induced by the Kerr nonlinearity and group velocity dispersion. While in conventional mode-locked solid state lasers the intracavity radiation propagates mostly in free space, in a fiber cavity it propagates within either pure or doped silica. This medium possesses values of both group velocity dispersion and nonlinear index that are non-negligible in comparison with free space. Therefore, both GVD and

Kerr nonlinearity can modify both the temporal profile and frequency spectrum of a pulse over many resonator round-trips.

The temporal broadening due to GVD is incorporated into the numerical simulation by means of the following (considering GVD separately from SPM) [37]:

$$\frac{\partial A}{\partial z} = \frac{-i}{2}\beta_2 \frac{\partial^2 A}{\partial t^2} \tag{2.8.3}$$

Taking the Fourier transform allows the above to be straightforwardly solved for the pulse envelope $\tilde{A}(z,\omega)$ in the frequency domain, so the pulse after a propagation distance z is:

$$\tilde{A}(z,\omega) = \tilde{A}(0,\omega)e^{\frac{i}{2}\beta_2\omega^2 z} \tag{2.8.4}$$

One may then obtain the broadened pulse envelope in the time domain by applying the inverse Fourier Transform to equation 2.8.4. Figure 2.17 shows dispersion-broadened pulses following propagation distances of z=10 and 50 km.

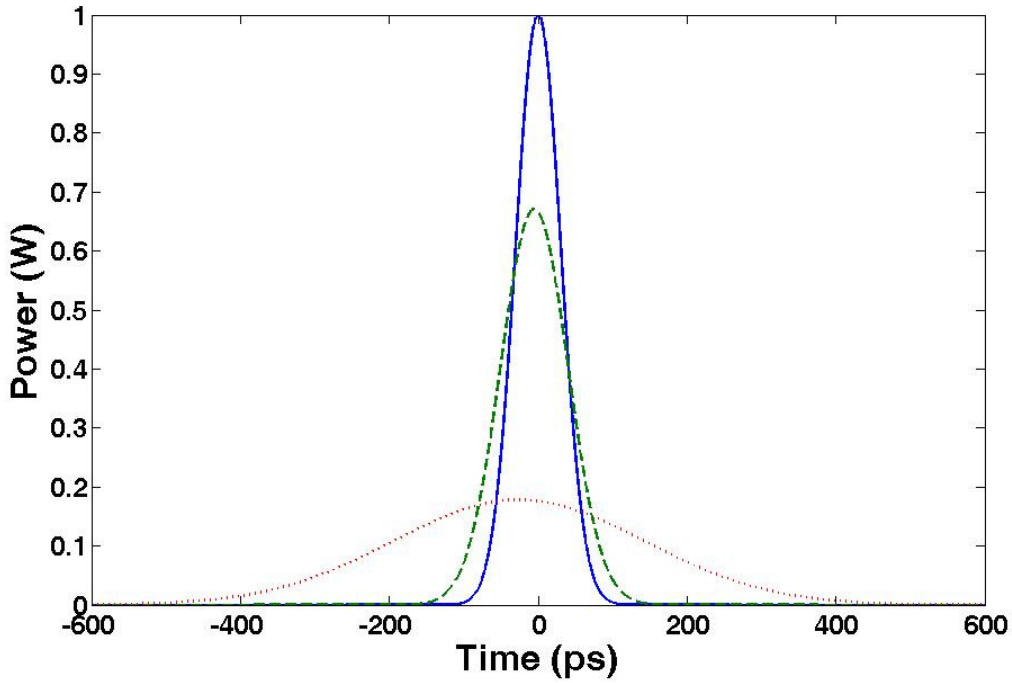

Figure 2.17: Initial 100 ps Gaussian pulse and broadened pulses following propagation within 10 km and 50 km of a medium with GVD coefficient 20 ps^2/km.

The nonlinear phase-shifts acquired by the propagating pulse due to Kerr nonlinearity and its resulting modification to the pulse spectrum are also straightforwardly incorporated into the simulation. In the absence of GVD, a pulse envelope propagates within a Kerr medium according to:

$$\frac{\partial A(z,t)}{\partial z} = i\gamma |A(z,t)|^2 \tag{2.8.5}$$

$$\Rightarrow A(z,t) = e^{i\gamma |A|^2 z} \tag{2.8.6}$$

When both these effects act simultaneously on a pulse, the combination of broadening in the time domain due to dispersion and broadening in the frequency domain

due to SPM combine to alter both the frequency and temporal profile after sufficient propagation distance. The pulse first becomes parabolic in shape before becoming rectangular, with oscillations on the pulse edges (figure 2.18). These oscillations are the result of the phenomenon of optical wave breaking [37]. As the pulse propagates through the fiber, the SPM imposes a red-shift for the leading edge of the pulse. These red-shifted frequency components travel at a faster speed than the unshifted light due to the material dispersion in the fiber (assuming normal dispersion) and overtake unshifted light closer to the tail of the pulse. The opposite occurs at the trailing pulse edge. As a result, the pulse tails will contain widely-separated frequencies which mix and produce new frequencies related to their frequency difference [98]. This wave-mixing generates both side-lobes in the frequency spectrum (visible in figure 2.18 d) as well as interference fringes at the pulse edges in the time domain (figure 2.18 c).

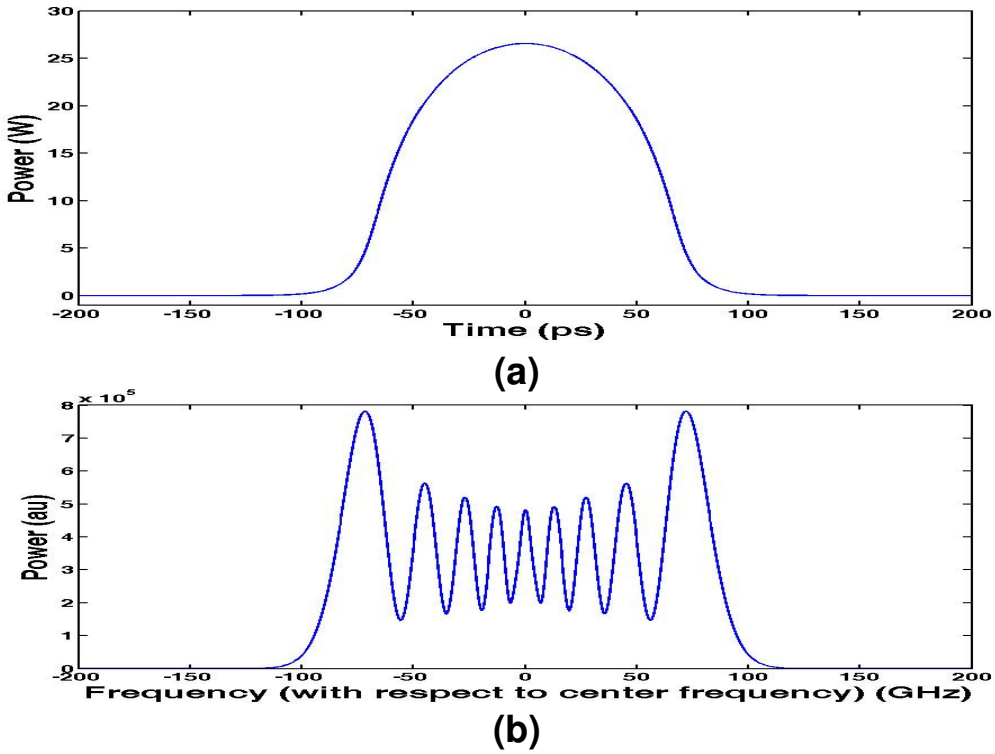

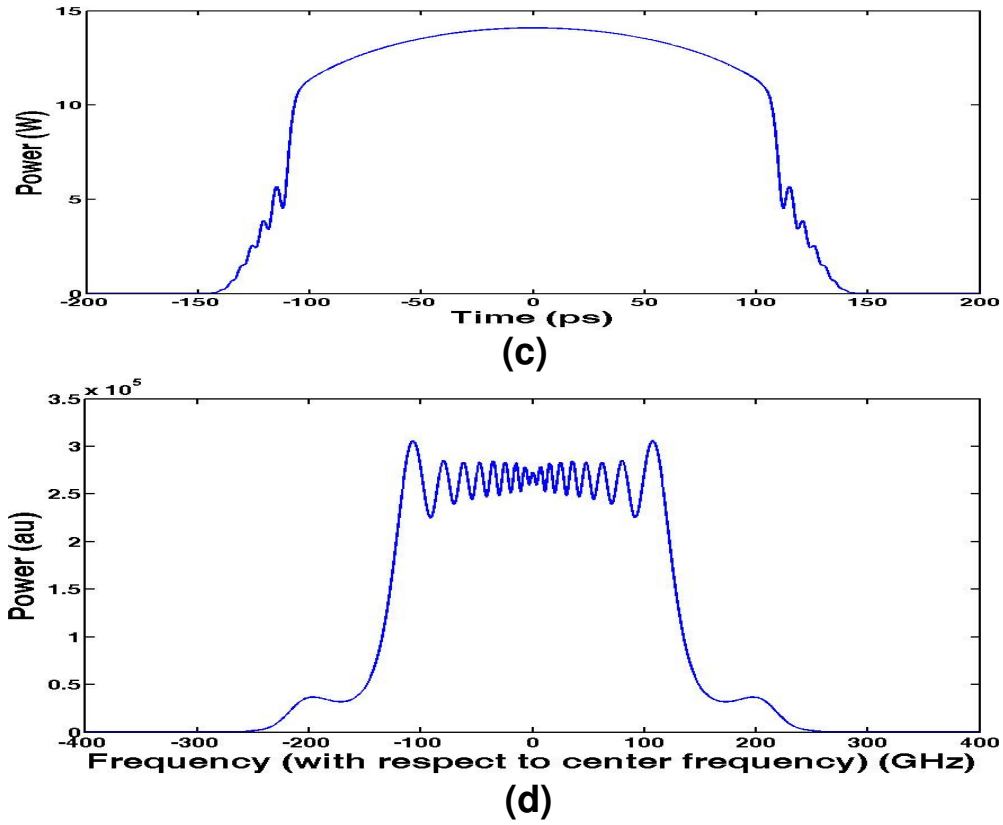

Figure 2.18: Temporal and spectral profiles of a 100 ps, 40 W peak power input pulse after undergoing both SPM and GVD in a single mode fiber. a,b) Temporal profile and spectrum following propagation through 200 m of fiber. c,d) Temporal profile and spectrum after 500 m.

The final effect to be considered in the laser modeling is that of spectral filtering. This can occur due to any element placed within the cavity that exhibits a frequency-dependent response within a finite frequency bandwidth. Such an element could be a gain medium with a finite emission linewidth, a bandpass filter with a resonant transmission, or a cavity mirror with a resonant reflection. Because of the extremely broad gain spectrum of ytterbium-doped fiber, the main bandwidth limiting elements in the linear laser cavity considered in this study are the reflectors that form the laser cavity. The frequency-dependent reflection from the cavity mirrors is modeled as a Lorentzian filter [1]:

$$R(\omega) = \frac{R_{FBG}}{1 + \left(\frac{\omega}{\Delta\omega_{HWHM}} \right)^2} \tag{2.8.7}$$

The above described effects were incorporated into a single numerical model to simulate the evolution of a pulse within a mode-locked laser cavity. The details of the simulation and the results are presented next.

2.8.2: Numerical Simulation

The split-step Fourier method was employed to simulate pulse evolution in the laser cavity in order to determine the conditions necessary for stable mode-locking [37]. The program calculates the linear effects of linear loss, group velocity dispersion and spectral filtering in the frequency domain according to equation 2.8.4 and equation 2.8.7, and the nonlinear effects of gain, saturable absorption and SPM in the time domain according to equation 2.8.2 and equation 2.8.6. A single simulation step is considered to be a single cavity round trip. The pulse is subjected to GVD and linear loss in the frequency domain in the first half-step, followed by gain, saturable absorption and SPM for a full step after transforming to the time domain. GVD and linear loss is applied for the second half step after again transforming to the frequency domain. Anomalous dispersion and spectral filtering at the output coupler are applied as lumped elements before passing the resulting pulse profile through the next round trip. The program iterates through the chosen number of round-trips. To simplify the calculations, the effect

of Q-switching was not included in this set of simulations, and the gain is assumed to saturate at a steady state value according to the average intracavity power:

$$g = \frac{g_0}{1 + \frac{P_{avg}}{P_g}} \tag{2.8.8}$$

$$P_{avg} = \frac{E_{pulse}}{T_{RT}}$$

$$P_g = \frac{h\nu_s}{\sigma_g \tau_g} \cdot A_g$$

This method is similar to the symmetrized split-step Fourier method described in [37]. The initial input pulse is considered to represent the intensity fluctuations present in the cavity as pumping is initiated due to mode beating [41]. The mode-locking is deemed to be stable and self-starting if the simulation converges to a single pulse that remains unchanged after a large number of round-trips. If the pulse breaks up into an unstable radiation pattern, it is concluded that stable mode-locking will not occur under the given conditions.

The simulation described here is based on those previously detailed in the literature [1;76;77;99]. Therefore, to test the efficacy of the program, a simulation was performed with a fast saturable absorber and identical cavity parameters as in [1] (see figure 2.19 for comparison), with the simulation yielding nearly identical radiation patterns under both the stable and unstable mode-locking conditions detailed in the reference. Therefore, the numerical method was deemed to be correct. Furthermore, to test the implementation of the slow saturable absorber model (equation 2.8.2),

simulations were performed under the same conditions as those considered with the fast saturable absorber for the slow absorber case with relaxation times ranging from a few to tens of picoseconds. As expected based on previous studies [77], the simulation still converged to a slightly longer pulse for short enough relaxation times (figure 2.20). Unlike in the fast absorber case, however, the pulse experiences a temporal shift before the steady state is reached, as expected from the discussion on slow and fast absorbers above.

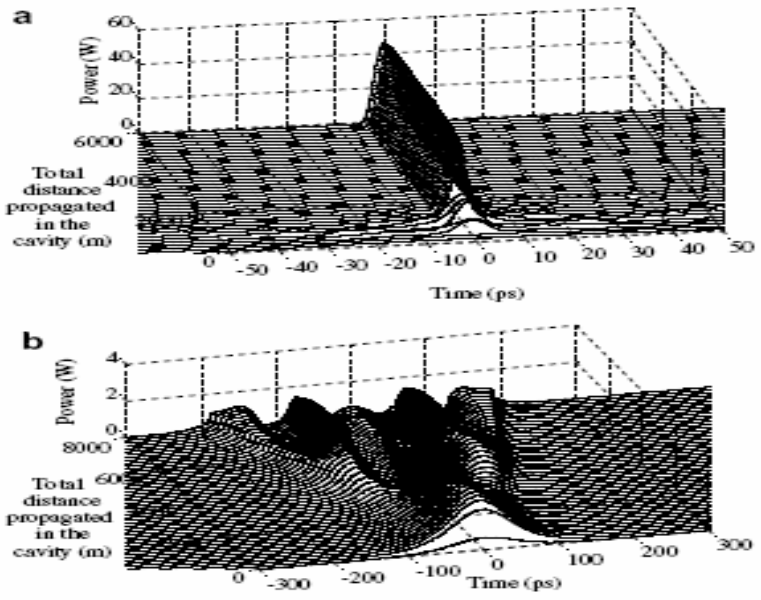

(a)

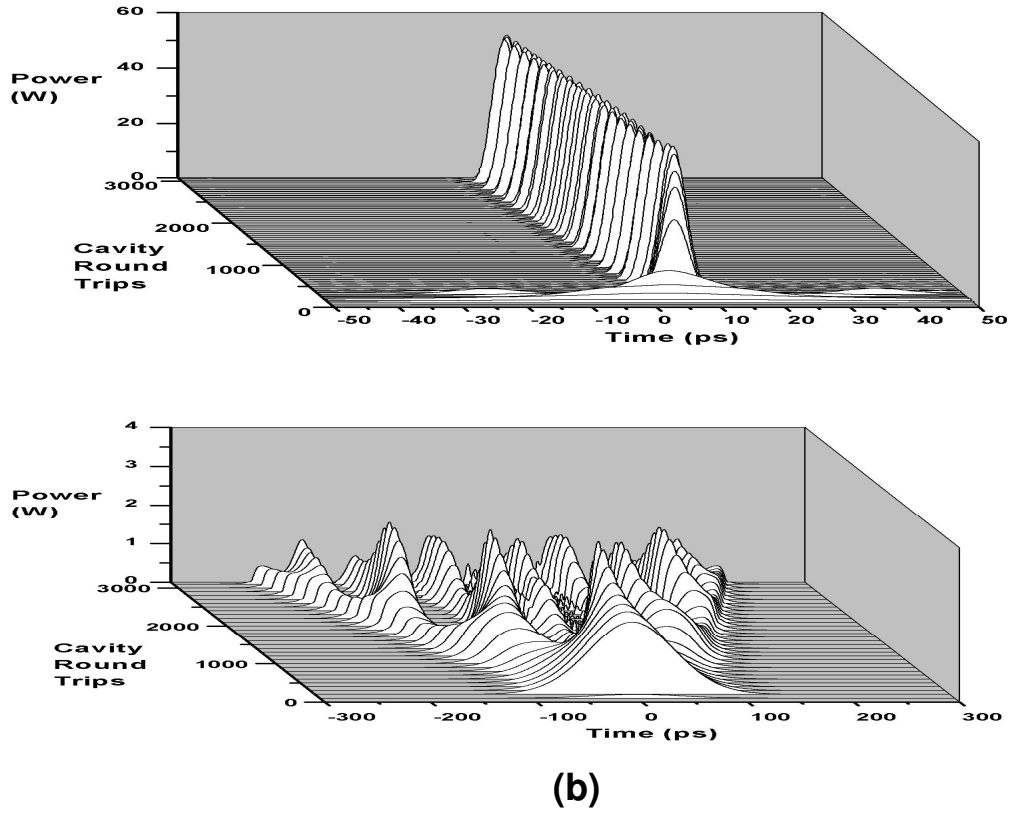

Figure 2.19: Simulated pulse evolution in a mode-locked Yb-doped fiber laser: a) Simulations performed in [1] with the addition of -4.77 ps^2 of dispersion compensation (above) and with no disperson compensation (below). b) Simulated pulse evolution produced using our simulation under identical conditions. With the addition of anomalous dispersion, the simulation converges to a 4.5 ps pulse.

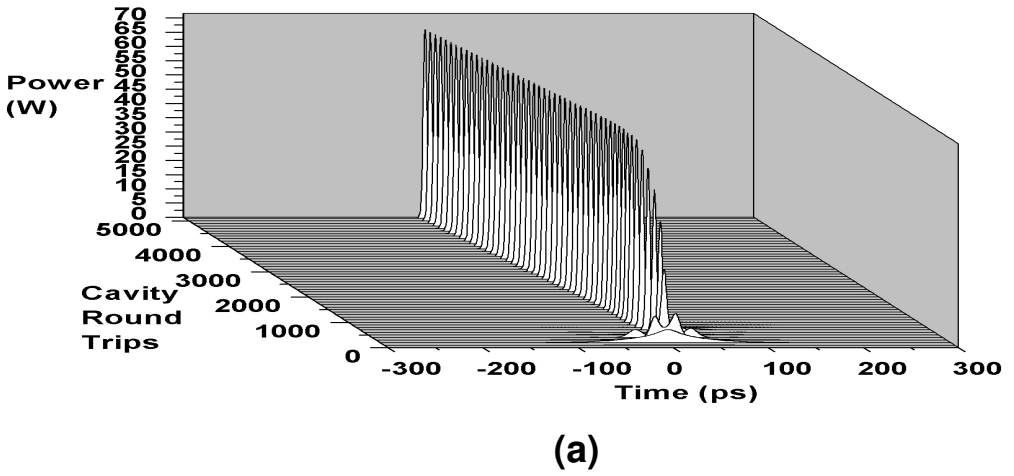

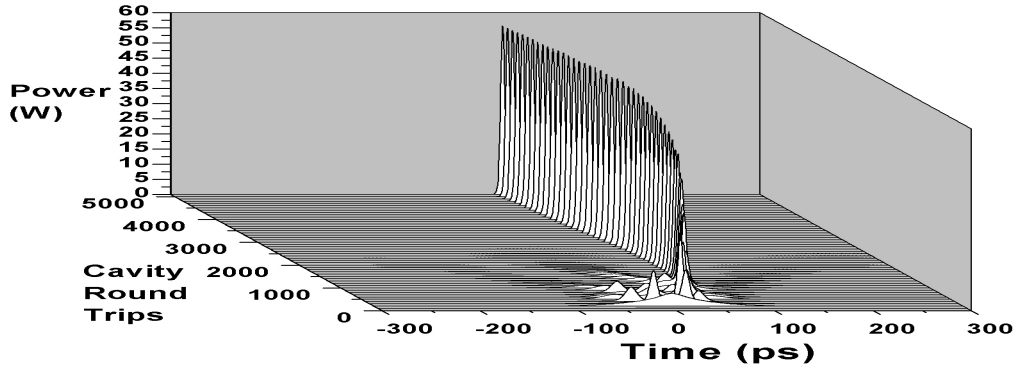

(b)

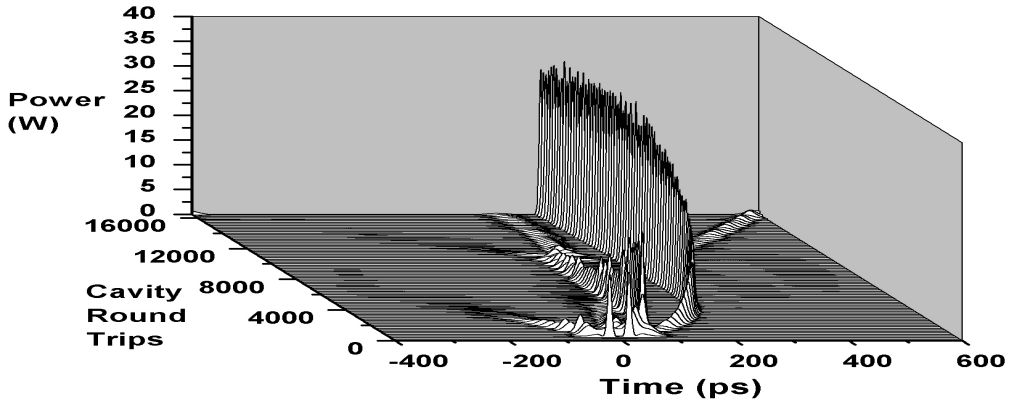

(c)

Figure 2.20: Simulated pulse evolutions for cavity parameters identical to those in figure 5, but for a slow saturable absorber of equal saturation power. a) 10 ps recovery time. b) 40 ps recovery time. c) 120 ps recovery time, showing instability due to the insufficient recovery of the saturable absorber.

As can be seen in figure 2.20, with increasing recovery time, low intensity trailing pulses begin to develop during the first iterations of the program. If the recovery time is short enough, they are gradually attenuated and are not present in the final radiation pattern. However, at recovery times greater than approximately 100 ps, the trailing pulse is not attenuated and is still present in the final output. This observation is consistent with previous numerical studies in the literature [76].

Fiber lasers emitting short pulses have traditionally relied on either soliton pulse shaping, in which the positive nonlinear phase shifts acting on the propagating pulse are balanced by the negative fiber GVD at the operating wavelength [77] or on the use of a dispersion map, in which the positive GVD of the cavity fibers is balanced by an additional negative dispersion added into the cavity [100]. Because of the positive value of the GVD in silica fibers at wavelengths below approximately 1300 nm [13] soliton mode-locking cannot occur in ytterbium-doped fiber lasers oscillating near 1 μm such as the one developed in this thesis. Researchers have traditionally relied on dispersion compensation to obtain short pulses from ytterbium-doped fiber lasers for this reason. Nonetheless, it has been shown that stable, short optical pulses can form within a fiber laser cavity oscillating in the normal dispersion region for silica fiber without the addition of anomalous negative dispersion [39]. Pulse shortening and stabilization in these lasers is achieved through both strong spectral filtering and saturable absorption. Over the course of one cavity round-trip, the pulse is broadened in the time domain due to GVD, and acquires a chirp following amplification in the gain medium because of SPM at the increased peak power [101]. Finally, the pulse is shortened in the time domain through amplitude modulation in the saturable absorber, and the spectral filter eliminates the frequency lobes in the pulse spectrum, thereby preventing pulse break-up due to optical wave breaking from occurring.

Numerical simulations show that these types of lasers tend to evolve toward a stable pulse with a temporal duration largely dictated by the intracavity dispersion [39]. In addition, the selected spectral filter bandwidth and the spectral broadening due to the SPM can further broaden or shorten the pulse, with the pulsing becoming unstable for

excessive SPM or too narrow or too wide filter bandwidth. It was found that after adjusting the dispersion by increasing the total cavity fiber length, the simulation evolved toward a 850 ps duration pulse that could be stabilized by a slow saturable absorber with nanosecond recovery time (figure 2.21 a).

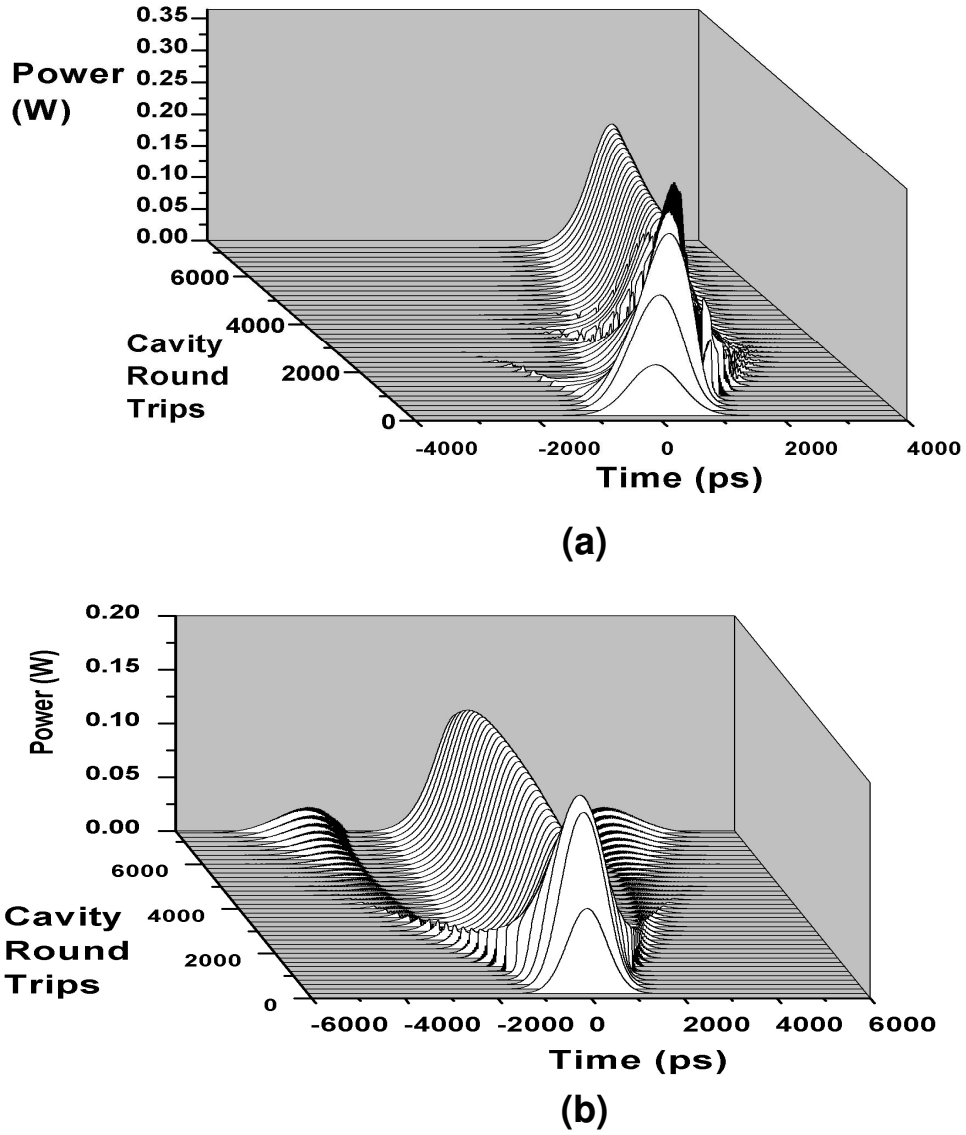

Figure 2.21: Simulated pulse evolutions in an ytterbium-doped fiber laser cavity of length 120 m with only normal dispersion. Spectral filter bandwidth: 5 nm, output mirror reflectivity: 79%, unsaturated gain factor: 1.684, unsaturated SA transmission: 90%. a) Convergence to a stable ~850 ps pulse when the SA saturation energy is set at 3 nJ with a 1 ns recovery time. b) Pulse break-up when the SA saturation energy is increased to 10 μJ.

To see the effect of the SA saturation energy on the pulse stabilization, the saturation energy was increased from 3 nJ to the approximate value of the saturation energy for our own samarium-doped fiber saturable absorber of ~10 μJ. Under these conditions, pulse break-up occurred before a steady state was reached (figure 2.21 b). At this value of the saturation energy, the SA behaves as a linear loss due to negligible saturation by the pulse with nanojoule-order energy and uniformly attenuated the entire pulse profile. Therefore, no pulse shaping occurs upon transmission through the SA. These results lead us to predict that the samarium-doped fiber saturable absorber cannot stabilize short steady-state mode-locked pulses through this mechanism.

It has been shown that a laser cavity that cannot support steady-state continuous wave mode-locking may still support transient Q-switched mode-locking [102;103]. The mode-locked pulses initiate from mode-beating as lasing initiates from spontaneous emission at the start of the Q-switching envelope [44]. The mode-locked pulses are sustained until the stored energy is dissipated since the Q-switching cycle does not encompass enough cavity round-trips for the pulses to break up into a continuous radiation pattern. Theoretical modeling of Q-switched mode-locking is complex and will not be described here. An experimental study on Q-switched mode-locked and Q-switched operation of the developed laser is presented next.

2.9: Experimental Results and Analysis

The pump radiation was launched into the fiber laser cavity by means of a 976 nm fiber pigtailed, diode laser module. Figure 2.22 shows the launched power as a function of laser diode current.

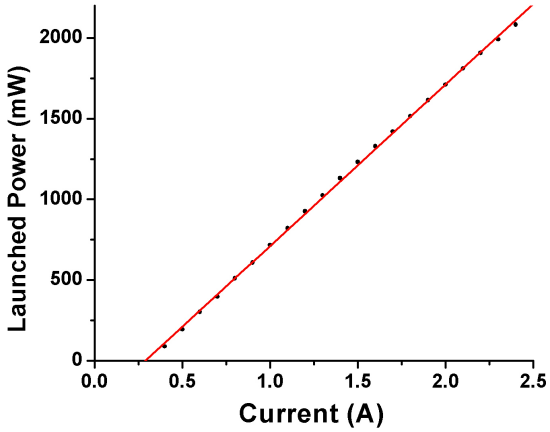

Figure 2.22: Pump laser characterization.

Continuous wave (CW) laser oscillation was observed as the pump current was increased above ~0.9 A corresponding to a launched pump power of ~600 mW. The high threshold for lasing is due to both the presence of the saturable absorber in the cavity and other intracavity losses, including a low coupling efficiency between the MMFC and the gain fiber, and the large number of mode area mismatched splices made while constructing the laser cavity. A scan of the laser emission line obtained using an optical spectrum analyzer (OSA) of resolution 1.25 GHz is shown in figure 2.23. The low resolution of the OSA prevented this instrument from being used to observe the individual longitudinal modes of the laser. To study the longitudinal mode structure during CW oscillation we used a scanning Fabry-Perot spectrum analyzer (SFPSA) with an 8 GHz FSR and 27 MHz resolution. The higher resolution of the SFPSA allowed it to resolve the individual longitudinal modes of the laser within a small portion of the ~60 GHz line profile measured by the OSA (figure 2.24). The SFPSA scan resolved ~24 laser cavity modes (figure 2.24, bottom).

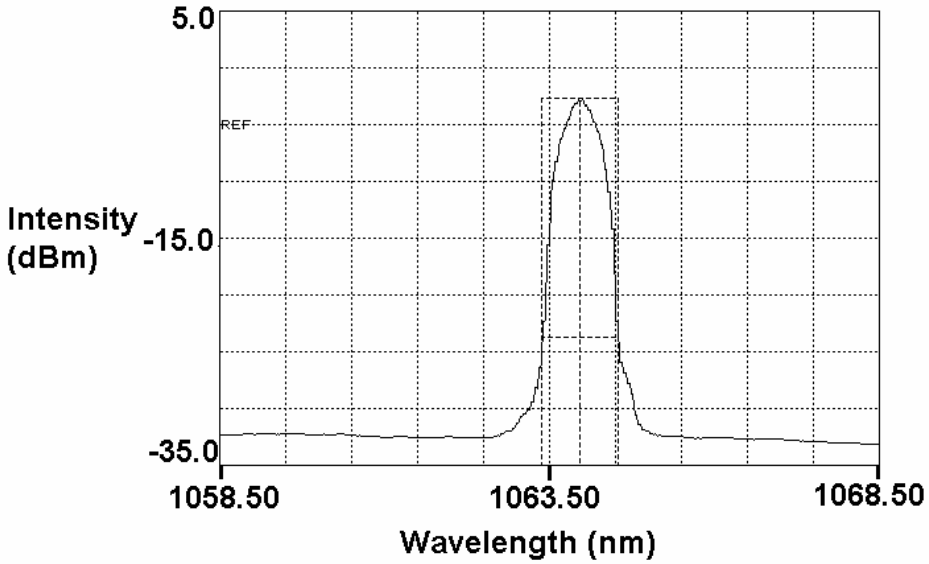

Figure 2.23: Output of the laser at a pump current setting of 1.0 A acquired using the Optical spectrum analyzer.

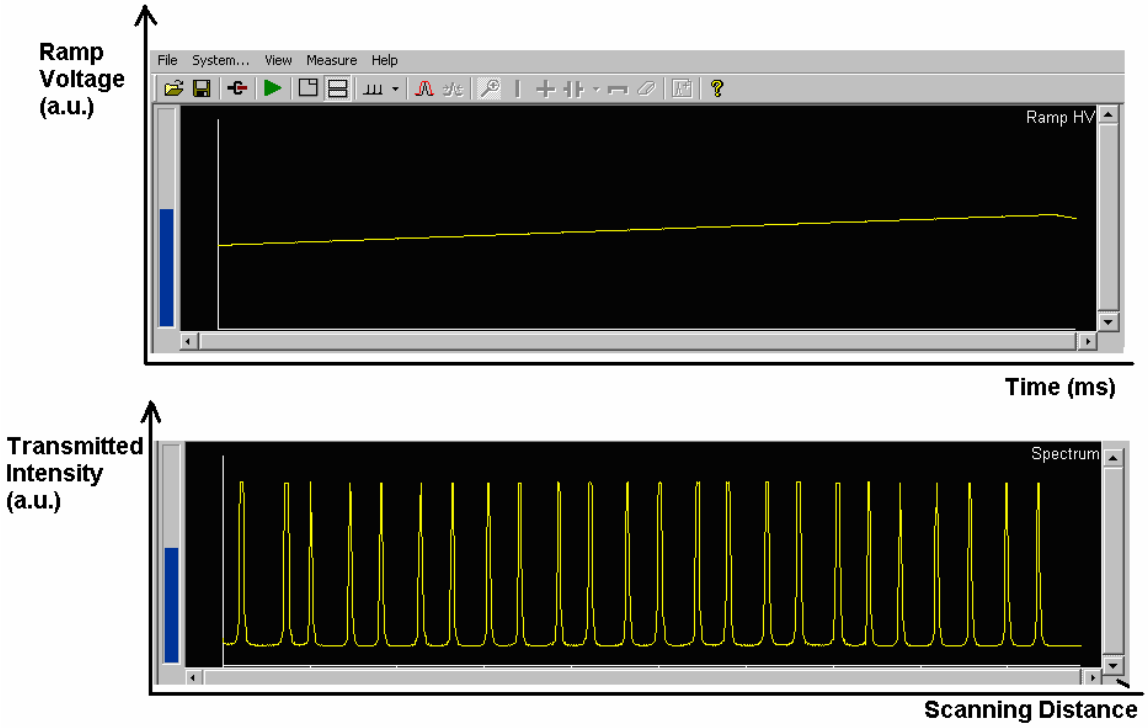

Figure 2.24: SPFSA scan of the laser during CW oscillation showing multiple longitudinal modes.

To determine the conditions for transitioning between CW and pulsed laser oscillation, we monitored the temporal profile of the laser output using a high speed InGaAs photo-detector (PD) with a maximum rise/fall time of 100 ps. The signal from the PD was measured using a 1 GHz digital oscilloscope. When the PC plates were suitably adjusted at low power, the CW oscillation gave way to a train of short, closely spaced pulses modulated by an envelope of ~91 ns duration (figure 2.25). This operation regime of the laser resembles the self mode-locked pulsing observed in other Q-switched fiber lasers [44]. The self mode-locked pulse trains were extremely stable at low pump power, with the repetition rate, duration and amplitude being very reliably reproduced from one Q-switched burst to the next.

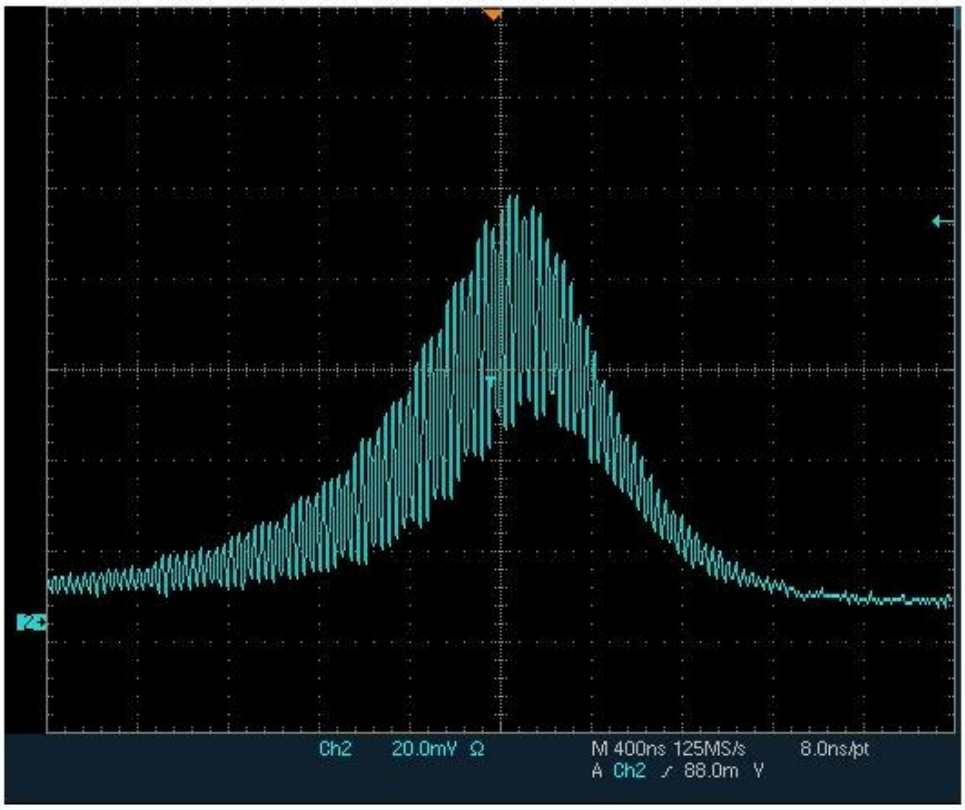

Figure 2.25: Output of the laser obtained using the PD and oscilloscope at a pump current setting of 1.0 A.

An expanded view of the mode-locked pulses is shown in figure 2.26. The mode-locked pulse duration and period were measured to be ~1.7 ns and~3.3 ns respectively. The measured mode-locked repetition rate of ~300 MHz is equal to almost exactly 20 times the estimated fundamental cavity repetition rate of $c/2nL_{cavity}$~15 MHz. This suggests that the observed short duration pulses underneath the Q-switched envelope are attributable to harmonic mode-locking [104-106] Periodic modulation of a Q-switched pulse profile has been also attributed to beating between different cavity modes at the detector [107]. However, the periodicity, consistent duration and high depth of modulation of the observed pulses are not consistent with such mode-beating. Furthermore, the Fourier transform of the oscilloscope signal shows a single peak at the measured mode-locked repetition rate (figure 2.27), consistent with mode-locking rather than mode-beating.

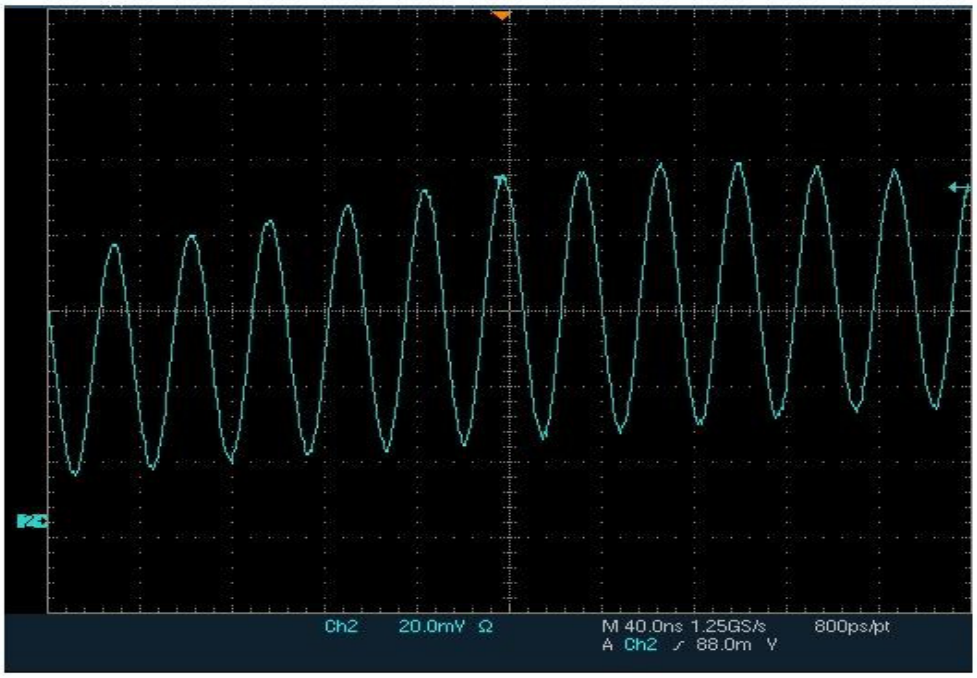

Figure 2.26: Expanded view of the mode-locked pulse train obtained using the PD and oscilloscope at a pump power of ~750 mW.

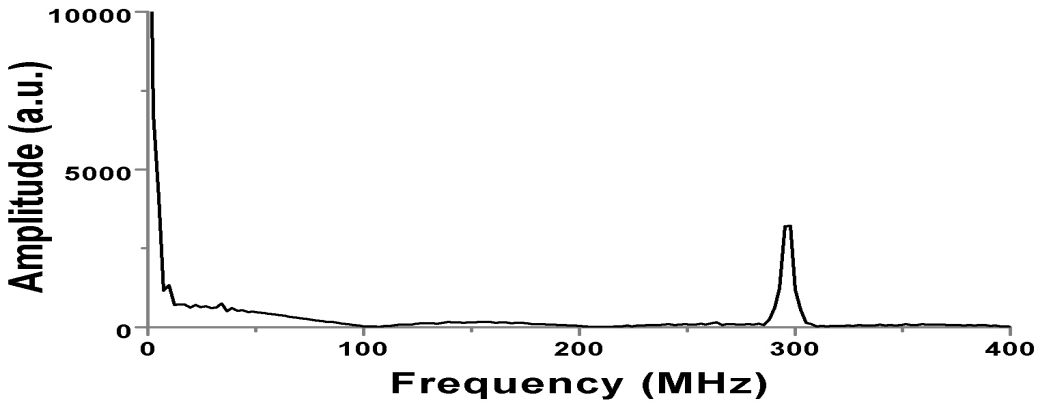

Figure 2.27: Fourier Transform of the Q-switched mode-locked laser output.

There are several indications that another mechanism besides the samarium-doped fiber saturable absorber is responsible for the observed mode-locked pulses. First, the theoretical studies presented in sections 2.7 and 2.8 suggest that the samarium-doped fiber possesses a saturation energy that is too high to provide the proper pulse shaping to stabilize mode-locked pulses [77]. Also, the nanosecond recovery time of Sm^{3+} is likely too long for the saturable absorber to recover fully between each of the high repetition rate mode-locked pulses. The presence of the polarization controller as a polarizing element within the cavity and the importance of its adjustment for achieving passive mode-locking means that the mode-locking is likely attributable to nonlinear polarization evolution (NPE) [108]. In this form of mode-locking, a circulating pulse acquires an elliptical polarization following transmission through a wave-plate combination such as the PC present within our cavity. The *x* and *y*-polarization components then propagate through a length of Kerr medium and undergo both linear and nonlinear phase delays due to birefringence, self phase modulation and their interaction with the other polarization

component (cross phase modulation) [109]. The total phase delay for each polarization component is written as [109]:

$$\Phi_x = \left\{ \beta_x + kn_2 \left[\left| A_x \right|^2 + (2/3) \left| A_y \right|^2 \right] \right\} 2L \qquad (2.9.1\ a)$$

$$\Phi_y = \left\{ \beta_y + kn_2 \left[\left| A_y \right|^2 + (2/3) \left| A_x \right|^2 \right] \right\} 2L \qquad (2.9.1\ b)$$

Where $\beta_{x,y}$ represents the propagation constants along each polarization direction, $A_{x,y}$ is the field amplitude of each polarization component and L is the propagation distance within the Kerr medium. The intensity dependence of the relative phase delays between the polarization components leads to higher intensity light undergoing a larger rotation of its polarization ellipse within the Kerr medium than low intensity light [40]. If the light waves are then superimposed with waves exiting the PC following transmission through the Kerr medium, the intensity-dependent polarization rotation is translated to an intensity-dependent interference between the waves with non-rotated and rotated polarization [108]. The superposition leads to the non-rotated, low-intensity waves undergoing a higher amplitude modulation then the rotated, high-intensity waves, effectively producing an artificial saturable absorption. Due to the instantaneous response of the Kerr nonlinearity, the artificial saturable absorber produced through NPE shapes pulses in a similar way as the fast saturable absorbers discussed in section 2.6 [97].

The mode-locked laser oscillation at a harmonic frequency can be explainable by the NPE mechanism. Both the modulation depth and the saturation energy of the artificial

fast saturable absorber are known to be highly sensitive to adjustment of the polarizing element [108;110]. Adjustments of the PC can therefore yield a saturation energy that is too low in comparison with the intra cavity energy to stabilize a single pulse. Under these conditions the oscillation of multiple, evenly spaced pulses is energetically favorable, leading to harmonic mode-locking [110;111].

As can be seen in figure 2.25, a full modulation to zero intensity was not achieved between the mode-locked pulses. It was found that the modulation depth of the mode-locked pulses was highly dependent on the position of the PC plates. This is most likely due to the sensitivity of the saturation power and modulation depth of the NPE artificial saturable absorber to the adjustment of the polarizing element [108]. However, the modulation depth of QML pulses is also well-known to be dependent on the strength of the Q-switching [102]. Weaker Q-switching leads to a longer rise-time for the Q-switched envelope, enabling the mode-locked pulses to reach a steady state with fuller modulation [112]. In the case of passive Q-switching, the strength of the Q-switching can be reduced by reducing the pump power or increasing the ratio of non-saturable to saturable losses (i.e. reducing the Q-factor of the cavity) [6;112;113]. The most straightforward way to lower the Q-factor of the cavity and improve the mode-locking contrast is to reduce the reflectivity of the output coupler mirror [114]. A lower Q-factor cavity can also improve the modulation of the mode-locked pulses by suppressing the CW background which makes up the signal observed below the mode-locked pulses [40]. These alterations can improve the modulation of the mode-locked pulses at the expense of poorer continuous-wave Q-switched operation.

At a pump power of ~1500 mW, and with further adjustment of the PC plates, the laser emitted a train of individual Q-switched pulses of ~70 ns duration at a repetition rate of ~270 kHz. The average power at this pump power was measured to be 2 mW, which is divided by the repetition rate to obtain an estimated pulse energy of ~7.5 nJ. This gives an estimated peak power of $E_{pulse}/\tau_{duration}$~106 mW. An oscilloscope trace of the Q-switched pulse train is shown in figure 2.28 a). We did not investigate the oscillation of the laser at pump current levels above 2.1 A in order to avoid damage to our cavity components and instruments from the high peak power of the Q-switched pulses.

The measured Q-switched pulse duration is only slightly longer than our estimated cavity round-trip time of $2nL/c$~68 ns. In addition, the Q-switched pulses are shorter than the Q-switched mode-locked envelopes observed at lower power and at different PC positions. These two observations suggest that the conditions for optimum Q-switching are fulfilled at this pump power level and polarization state [115]. At lower pump power the small-signal gain and stored energy within the gain medium is lower, leading to a slower saturation of the samarium-doped fiber at the beginning of the Q-switched pulse. The weaker passive Q-switching under these conditions leads to a slower build-up of the Q-switched pulse, enabling the mode-locked pulses to evolve from noise at the start of the Q-switched envelope [44;102]. Because the stored energy in the gain medium is dissipated by a series of lower energy short duration mode-locked pulses rather than a single Q-switched pulse, the length of the Q-switching envelope is increased. At the increased pump power and different PC position, the small signal gain and stored energy becomes high enough to rapidly saturate the SA, enabling the Q-switched pulse to build up in an almost instantaneous fashion [6;115]. The rapid increase

in amplitude observed at the start of the individual Q-switched pulse in figures 2.29 b) supports this explanation.

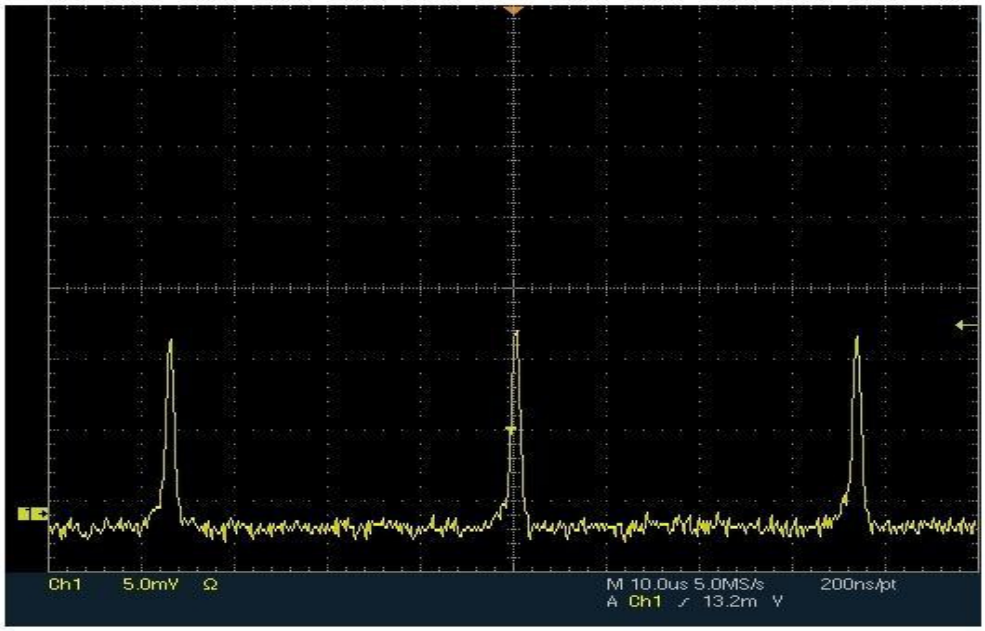

(a)

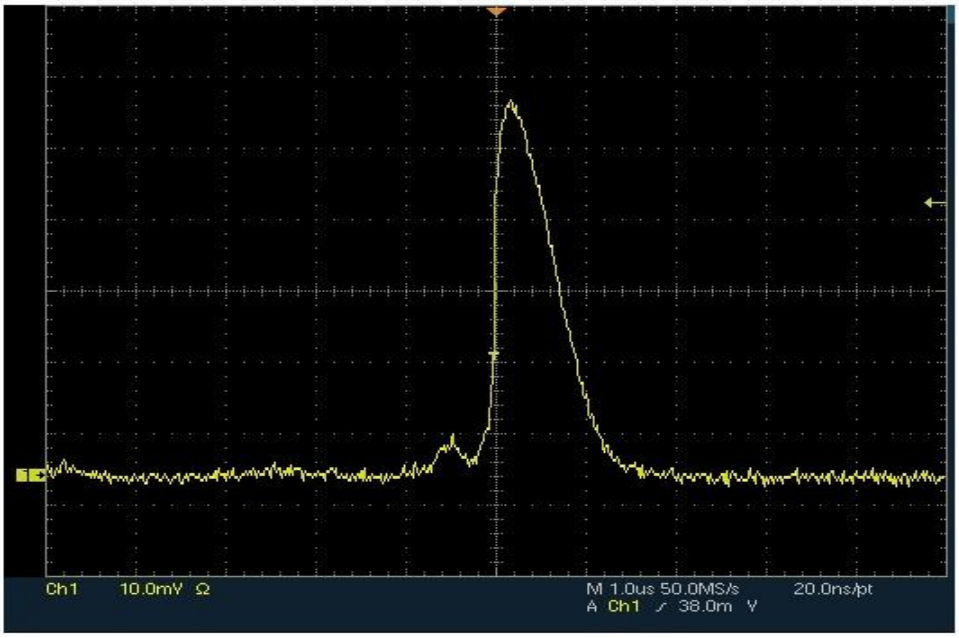

(b)

Figure 2.28: Output of the laser in the Q-switching regime measured using the PD and oscilloscope at a pump current setting of 1.8 A. a) Q-switched pulse train. b) Single Q-switched Pulse.

For giant pulses such as the ones described above to form in a laser cavity containing a saturable absorber, it is necessary for the SA to saturate quickly as the energy stored within the gain medium is released [6]. This requires the gain saturation energy to be large in comparison to the SA saturation energy, in addition to sufficient pumping in the gain medium. The usual approach to fulfilling this requirement is to select a saturable absorber with an absorption cross-section much larger than the emission cross-section of the gain medium [116]. However, the roughly 3 to 1 ratio of our SA cross-section to gain cross-section (based on data from the fiber manufacturers) is much smaller than the required value of ~20 given in numerical studies of fiber lasers Q-switched with fiber saturable absorbers [115]. The good Q-switching performance seen in our laser despite this can be explained by the mismatch in mode field areas between the gain and saturable absorber fibers. Since the saturation energy is directly proportional to the effective mode area of the fiber (see eq. 2.6.18) the smaller mode area in the 6.5 μm core SA fiber decreases its saturation energy in relation to that of the 8.2 μm core double-clad gain fiber. This focusing effect within the SA fiber allows it to be quickly bleached at the start of the Q-switched pulse [117], leading to rapid depletion of the stored energy in the gain medium and the short giant pulses observed here.

2.10: Conclusion

We have demonstrated an ytterbium-doped fiber laser with both continuous wave and pulsed output at 1064 μm. Q-switched operation was achieved by inserting a length of samarium doped fiber into the laser cavity to act as a saturable absorber passive Q-switch. The laser oscillated in the continuous wave, Q-switched mode-locked and Q-

switched regimes depending on the pump power and the setting of the PC plates. At low power the laser emitted Q-switched mode-locked pulses with duration of approximately 1.7 ns at a repetition rate of ~300 MHz when the PC plates were properly adjusted. The mode-locking was attributed to nonlinear polarization evolution. At high pump power we obtained ~70 ns Q-switched pulses with an average power of 2 mW. The pulse energy and peak power were estimated to be ~7.5 nJ and ~106 mW near the threshold for Q-switching.

Chapter 3

Potential application of the Developed Laser

3.1: Introduction

Nanometer-scale noble metal (gold, silver, platinum) particles and colloidal solutions of these metals have been known for centuries. Stained glass windows owe their colour to metal nanoparticles lodged within the glass, and gold and silver particle solutions have been produced since ancient times. It was not until recently that the unique optical properties of nanoscale metal particles were explained, and that their true potential applications came to light. Noble metal nanostructures have already found applications in cancer treatment [118], chemical and biological sensing [119], Raman spectroscopy [120] and as contrast agents in Optical coherence tomography (OCT) [121].

The optical properties of matter are highly dependent on both its composition and surroundings. By passing optical radiation through a sample and measuring the resultant transmitted, scattered and back-reflected signal, it is possible to gain information about its

composition and properties (figure 3.1). By monitoring these optical signals as a function of time, it is also possible to detect changes in these characteristics [121]. This is the basic principle behind all spectroscopic and imaging techniques [119;120;122].

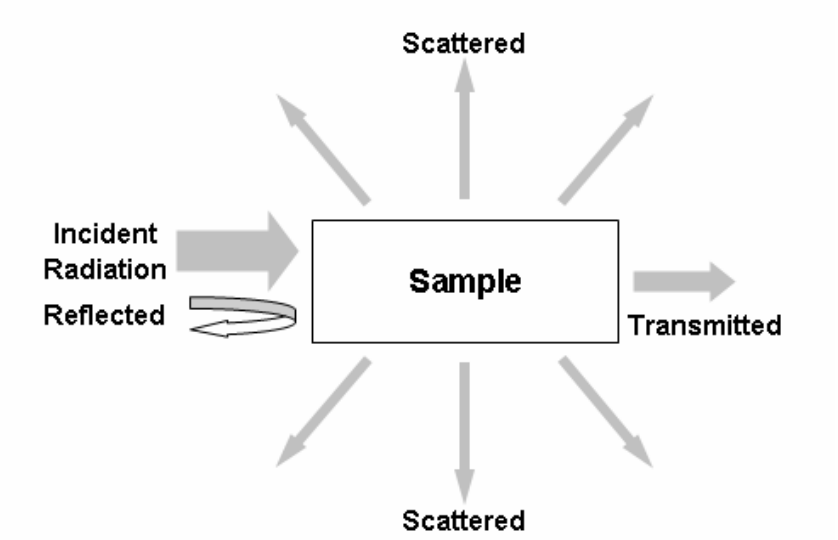

Figure 3.1: Interaction of a sample with optical radiation and the resulting measurable signals.

The metal nanostructures discussed in this chapter possess strong optical scattering and absorption characteristics. Making use of these particles in spectroscopy can therefore allow for an improvement in sensitivity through an increase in the measurable optical signal [123]. This property makes them ideal for applications in sensing [119].

In this chapter, we describe the theory of scattering of electromagnetic waves by nanoparticles and the results of preliminary experiments with gold nanorods will be presented.

3.2: Localized Surface Plasmon Resonance

The differences between the optical properties of dielectrics and metals are easily observable. These properties arise from their electronic structure [124]. Solid transition metals possess large numbers of delocalized electrons within their partly filled *d* orbitals which are free to move about the bulk of the material. The highly mobile charges within metals are responsible for their conductive properties and their response to electromagnetic radiation [125].

The optical properties of a material can be understood by considering the response of the free electrons to an applied oscillating electric field. The external field induces a polarization (net displacement of charge) in the metal or dielectric. The polarization is related to the applied field by a parameter called the susceptibility:

$$\vec{P} = \varepsilon_0 \chi \vec{E} \tag{3.2.1}$$

The susceptibility is represented by the symbol χ. The effect of this polarization is included in the so-called electric displacement field:

$$\begin{aligned} \vec{D} &= \varepsilon_0 \vec{E} + \vec{P} \\ &= \varepsilon \cdot \varepsilon_0 \vec{E} \end{aligned} \tag{3.2.2}$$

Where ε represents the dielectric function, which is characteristic of the material. It quantifies the response of the free electrons to the external field, and in the case of an

oscillating field, it will exhibit strong frequency dependence. The dielectric function of a classical free electron metal in an external field oscillating at a frequency "ω" is [126]:

$$\varepsilon(\omega) = 1 - \frac{\omega_p^2}{\left(\omega^2 + i\frac{\omega}{\tau}\right)} \tag{3.2.3}$$

Where $\omega_p^2 = ne^2/m\varepsilon_0$ is the plasma frequency. The frequency-dependent optical response of metals arises from the ω dependence of the complex dielectric function (equation 3.2.3). This can be seen by considering the basic dispersion relation for electromagnetic waves:

$$\begin{aligned} &\vec{E} = \vec{E}_0 e^{i(\vec{K}\cdot\vec{r}-\omega t)} \\ &\varepsilon\left(\omega, \vec{K}\right)\omega^2 = c^2 K^2 \end{aligned} \tag{3.2.5}$$

When $\omega<\omega_p$, ε and the wave-vector $\boldsymbol{K}$ is complex, and the wave is damped in space. Within this frequency range, EM waves do not propagate within metals and are either absorbed or reflected [124]. The significance of the plasma frequency may further be seen by considering the case of negligible damping where $\varepsilon(\omega) = 1 - \omega_p^2 / \omega^2$. Substituting this into equation 3.2.4, we get the dispersion relation for a transverse EM wave in a plasma:

$$\omega^2 - \omega_p^2 = c^2 K^2 \tag{3.2.6}$$

Equation 3.2.5 shows that the wavevector is real for frequencies above ω_p. This corresponds to the transparency region for metals. Finally, for the case of $\omega=\omega_p$, the dielectric function and also the wavevector is equal to zero. At this frequency the free electrons undergo a longitudinal oscillation known as a volume Plasmon within the bulk of the metal [126].

The longitudinal nature of volume plasmons means that they must be excited by electron scattering rather than optical photons [124]. Despite this, it is still possible for an EM wave to directly excite a transverse charge oscillation in a metal by coupling to the electrons in a sub-wavelength sized metal protrusion or particle [126]. The excitation of a surface Plasmon on a sub-wavelength metal structure is called localized surface Plasmon resonance (LSPR).

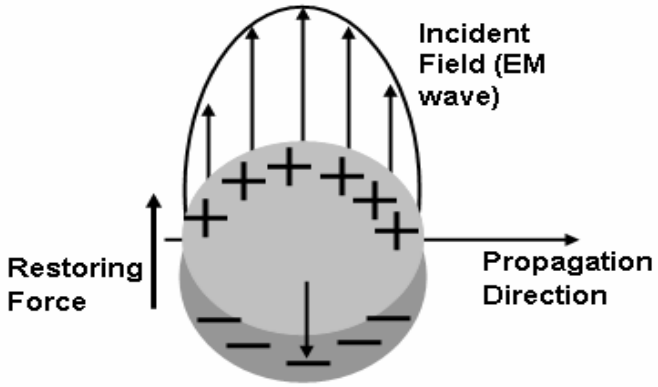

Figure 3.2: Excitation of a localized surface Plasmon by an incident EM wave [118].

The excitation of LSPR by EM waves gives rise to the unique optical properties of nanometer-sized metal particles in comparison to their bulk counterparts [127]. An understanding of the difference between the plasma oscillation within bulk metals and

sub-wavelength metal particles may be gained by considering the case of a sphere within a uniform electric field. This assumption is justified for particles with a diameter much smaller than the wavelength of the exciting wave, since in this case the optical field does not vary across the volume of the particle. The polarization of a sphere subjected to a field E_0 in free space is [124]:

$$P = \frac{\chi \varepsilon_0 E_0}{1 + \chi / 3} \tag{3.2.7}$$

Returning to the free-electron model discussed above, we have for the susceptibility $\chi = -ne^2/m\omega^2$. Substituting this into equation 3.2.8 gives a maximum polarization at $\omega_{LSP} = \omega_p / \sqrt{3}$. Thus the surface Plasmon frequency for a nanoscale diameter metal particle is red-shifted with respect to that of a bulk metal. The result given here is independent of particle size, however, the localized surface Plasmon (LSP) frequency of real particles exhibits a small size dependence. This is attributable to scattering events at the particle surface in small particles and damping and dephasing of the plasma oscillation at large sizes approaching the wavelength of the exciting EM wave [128].

The LSP frequency is also highly dependent on the external dielectric environment of the nanoparticle. If the free-space dielectric constant in equation 3.2.8 is replaced with an arbitrary dielectric constant ε_2, the LSP frequency becomes $\omega_{LSP} = \omega_p / \sqrt{1 + 2\varepsilon_2}$. Given the relation $\varepsilon_2 = n_2^2$ between the external dielectric constant and refractive index, it is clear that the LSP frequency will red-shift as the

external refractive index increases. This property is well studied [127], and has already been exploited for sensing applications to measure changes in the chemical environment of nanoparticles [119].

When excited by an EM wave at the LSP frequency, a nanoparticle can act as a scatterer and absorber with an interaction cross-section equal to many times its physical cross-section. The scattering and absorption cross-sections of a spherical particle can be shown to be [126]:

$$C_{Scattering} = \frac{8\pi}{3} k^4 a^6 \left| \frac{\varepsilon - \varepsilon_m}{\varepsilon + 2\varepsilon_m} \right|^2 \tag{3.2.10}$$

$$C_{absorption} = 4\pi k a^3 \, \mathrm{Im}\left[\frac{\varepsilon - \varepsilon_m}{\varepsilon + 2\varepsilon_m} \right] \tag{3.2.11}$$

The scattering and absorption cross-sections scale with a^6 and a^3. It is therefore clearly possible for these cross-sections to be larger than the physical area πa^2 when the LSPR condition is fulfilled. Under these conditions the local fields are greatly enhanced due to the LSP oscillation, it is therefore possible for the scattered or absorbed energy flux to be greater than the incident flux, increasing the effective scattering or absorption cross-section of the particle. This explains the strong extinction (sum of absorption and scattering) observed for nanoparticles excited at their LSPR frequency.

3.3: Particles with Tunable LSPR: Nanorods

It was shown in the previous section that the LSPR frequency of uniform, spherical nanoparticles may be shifted only a small amount by changing the particle size. This limited tunability leaves the near-IR wavelength band around 1 μm out of reach of the optical response of homogeneous spherical nanoparticles. However, for *in-vivo* biological applications, it is advantageous for nanoparticles to have an extinction maximum between 900 and 1100 nm [118;129] because of the low optical density of soft tissue components at these wavelengths [130]. The issue of limited LSPR tunability in homogeneous spherical particles can be overcome either by lifting their homogeneity of composition[131] or by altering their spherical symmetry [132].

It is possible to achieve large shifts in the LSPR frequency by elongating a nanoparticle to form a cylindrical nanorod [133]. A nanorod supports two surface Plasmon modes: a transverse mode along the short axis of the rod, and a longitudinal mode along the long axis of the rod as shown in figure 3.3 a) [134]. Since the longitudinal mode is forced to oscillate at a frequency corresponding to a node at each nanoparticle end, the longitudinal LSPR frequency red-shifts with increasing rod length when the diameter is kept constant (figure 3.3 b). The extinction spectrum of nanorods may be approximated analytically through an extension of the theory of scattering by spheres describing scattering by ellipsoids (Gans theory) [135] or calculated numerically using either a method called the discrete dipole approximation [134] or the finite difference time domain method.

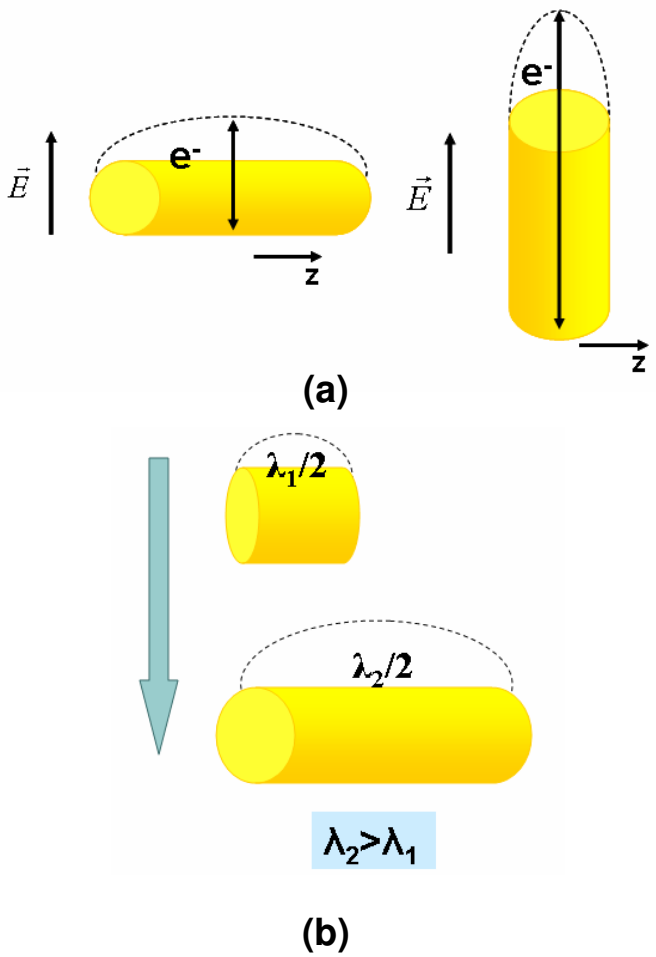

Figure 3.3: a) Longitudinal (left) and transverse (right) Plasmon modes of a nanorod. b) Red-shift of the fundamental longitudinal Plasmon mode with increasing length.

Synthesis of gold nanorods begins with gold nanospheres as a starting point, in the presence of a cationic surfactant called Cetyl trimethylammonium bromide (CTAB). The process begins with the formation of facets on the particles corresponding to the [1 1 0] and [1 0 0] planes of the gold FCC crystal structure [136]. Due to the lower binding energy of the CTAB head group to the [1 1 0] facet, these facets become coated with surfactant, preventing reduction of gold cations onto these surfaces. Therefore, growth of solid gold only occurs along the exposed [1 0 0] facets, resulting in the one dimensional growth of nanorods in the [1 0 0] direction [137]. In addition, because the hydrocarbon

chain portion of CTAB is hydrophobic, and the cationic head group is hydrophilic, the surfactant will form a positively charged bilayer on the sides of the nanorod with the head groups facing outward and the hydrocarbon chains facing inward. The CTAB thus functions to facilitate the growth of the rods as well as to keep them in suspension by means of coulomb repulsion [138]. The positively-charged bilayer also allows negatively charged molecules to be electro-statically adsorbed onto the particle surface (figure 3.4). The resulting modification to the local dielectric environment of the nanoparticle can shift the LSPR frequency. This may be exploited to conjugate nanorods with certain antibodies when placed in a basic (pH above 7.0) solution, or to detect a certain analyte in basic solution by monitoring the extinction spectrum of suspended nanorods [139;140]. Adsorption onto a nanoparticle surface may also take place via chemisorption in which a molecule covalently bonds to the surface, or through physisorption, where the molecule is attracted to the nanoparticle by the Van der Waals force [141]. Because of the comparative weakness of Van der Waals interactions, the former adsorption process is typically much weaker than both chemisorption and electrostatic adsorption.

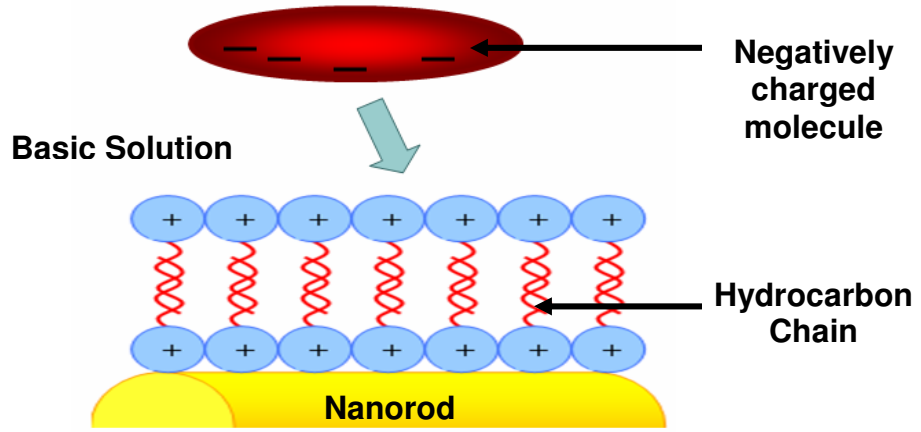

Figure 3.4: Electrostatic adsorption. A molecule in a basic solution with a pH above the isoelectric point acquires a net negative charge, resulting in an electrostatic attraction to the positively charged bilayer on the nanorod surface [139].

3.4: Experimental Methods, Results and Discussion

Experiments were performed using a commercially available solution of gold nanorods suspended by CTAB. The approximate axial diameter of the nanorods was 10 nm and the length was 67 nm giving an aspect ratio of 6.7 and a longitudinal LSPR extinction maximum of 1060 nm according to information provided by the manufacturer. The particle concentration was $4.1*10^{11}$ particles/mL (0.03 mg Au/mL) and the CTAB concentration was <0.1% by mass. The extinction spectrum of the nanorod solution as provided was first acquired using a UV-VIS-NIR spectrophotometer (Varian Cary 50). Figure 3.5 shows the extinction spectrum with both the smaller amplitude transverse LSP peak at ~515 nm and the larger amplitude longitudinal LSP peak at ~1083 nm being clearly visible. We note that although the instrument outputs data as absorbance vs. wavelength, this figure is simply calculated using the ratio of throughput light intensity to input light intensity. Since neither the scattered nor the absorbed radiation is likely to be detected following transmission of the signal through the sample, the output from the spectrophotometer is assumed to represent the extinction spectrum of the sample.

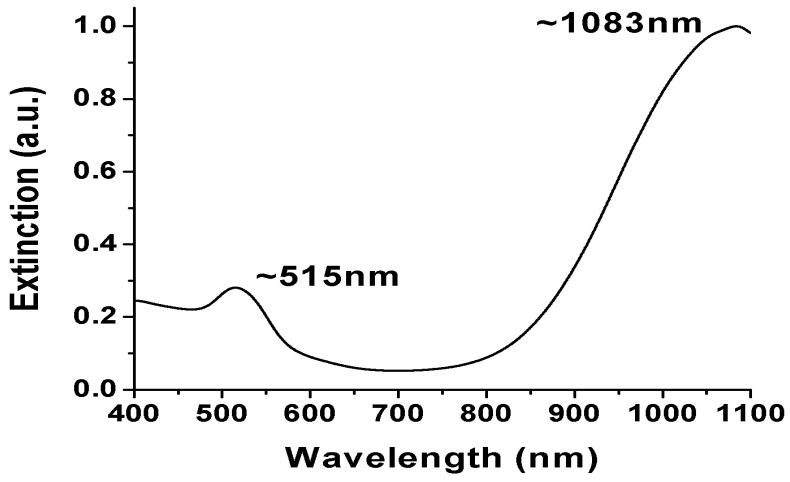

Figure 3.5: Extinction spectrum of the nanorod solution.

The low sensitivity and resolution, limited scanning range and insufficient light source brightness of the commercial instruments used in this study limited the obtainable results. Although commercial diode lasers are available with emission wavelengths within our region of interest, their stability and linewidth are limited without external stabilization. Diode lasers may be stabilized using either an external grating [142] or resonant cavity [143], but the brightness of these lasers is limited.

The laser developed in chapter 2 can potentially overcome these limitations. The nanoparticle surface effects can be further increased by the high peak power at low average power of our laser when operating in the pulsed mode. The enhanced inelastic scattering from molecules adsorbed onto the surface of nanorods excited on-resonance may be exploited for applications in sensing [144].

3.5: Conclusions

In this chapter we presented an early theoretical and experimental study on the interaction of gold nanoparticles and infrared radiation. The extinction spectra of gold nanorod samples in the aqueous state were measured. The optical measurements we were able to acquire were limited by the commercial instruments and diode laser used in our experiments.

Chapter 4

Summary

In this thesis, we presented study of ytterbium-doped fiber lasers and their applications. An ytterbium-doped fiber laser oscillating at 1064 nm was presented in chapter 2. The pulsed operation of this laser was investigated theoretically and experimentally. A series of numerical simulations on pulse formation in ytterbium-doped fiber lasers as well as experimental results with the developed laser were presented. The laser oscillated in the continuous wave, Q-switched mode-locked or Q-switched regimes depending on the pump power and adjustment of the intracavity polarization controller. Harmonic mode-locked pulses with a repetition rate of ~300 MHz and duration of ~1.7 ns were obtained. Q-switched pulses with duration of ~70 ns and ~7.5 nJ pulse energy were observed at a pump power of ~1500 mW. The Q-switching behaviour of the laser was attributed to the presence of the samarium-doped fiber saturable absorber in the cavity

while nonlinear polarization evolution was proposed as the mechanism for the passive mode-locking.

The applications of near-infrared lasers and gold nanoparticles in sensing were described in chapter 3. Early experimental results with gold nanorod samples using existing commercial instruments were presented.

References

[1] O. Katz, Y. Sintov, Y. Nafcha, and Y. Glick, "Passively mode-locked ytterbium fiber laser utilizing chirped-fiber-Bragg-gratings for dispersion control," *Optics Communications*, vol. 269, no. 1, pp. 156-165, Jan.2007.

[2] C. G. R. Geddes, C. Toth, J. van Tilborg, E. Esarey, C. B. Schroeder, D. Bruhwiler, C. Nieter, J. Cary, and W. P. Leemans, "High-quality electron beams from a laser wakefield accelerator using plasma-channel guiding," *Nature*, vol. 431, no. 7008, pp. 538-541, Sept.2004.

[3] D. Keefe, "Inertial Confinement Fusion," *Annual Review of Nuclear and Particle Science*, vol. 32, pp. 391-441, 1982.

[4] A. L. Schawlow and C. H. Townes, "Infrared and Optical Masers,", 112 ed 1958, pp. 1940-1949.

[5] T. H. Maiman, "Stimulated Optical Radiation in Ruby," *Nature*, vol. 187, pp. 493-494, June1960.

[6] A. E. Siegman, *Lasers* University Science Books, 1986.

[7] D. J. Griffiths, *Introduction to Quantum Mechanics*, 2 ed. Upper Saddle River, NJ: Pearson Prentice Hall, 2005.

[8] E. Hecht, *Optics*, 4 ed. San Francisco: Addison Wesley, 2002.

[9] A. Yariv, *Optical Electronics in Modern Communications*, 5 ed. New York: Oxford University Press, 1997.

[10] G. Das and Z. J. Chaboyer, "Single-wavelength fiber laser with 250 mW output power at 1.57 μm," *Optics Express*, vol. 17, no. 10, pp. 7750-7755, 2009.

[11] G. Das and J. W. Y. Lit, "L-band multiwavelength fiber laser using an elliptical fiber," *Ieee Photonics Technology Letters*, vol. 14, no. 5, pp. 606-608, May2002.

[12] J. Valiunas and G. Das, "Tunable Single-Longitudinal-Mode High-Power Fiber Laser," *International Journal of Optics*, vol. 2012, no. Article ID 475056, pp. 1-6, 2012.

[13] G. Keiser, *Optical Fiber Communications*, 3 ed. Boston, MA: McGraw Hill, 2000.

[14] K. C. Kao and G. A. Hockham, "Dielectric-fibre surface waveguides for optical frequencies,", 113 ed 1966, pp. 1151-1158.

[15] W. A. Gambling, "The rise and rise of optical fibers," *Ieee Journal of Selected Topics in Quantum Electronics*, vol. 6, no. 6, pp. 1084-1093, Nov.2000.

[16] W. A. Gambling, "The rise and rise of optical fibers," *Ieee Journal of Selected Topics in Quantum Electronics*, vol. 6, no. 6, pp. 1084-1093, Nov.2000.

[17] A. K. Ghatak and K. Thyagarajan, *Introduction to Fiber Optics*, 1 ed. New York: Cambridge University Press, 1998.

[18] A. W. Snyder and W. R. Young, "Modes of Optical-Waveguides," *Journal of the Optical Society of America*, vol. 68, no. 3, pp. 297-309, 1978.

[19] S. B. Poole, D. N. Payne, and M. E. Fermann, "Fabrication of Low-Loss Optical Fibers Containing Rare-Earth Ions," *Electronics Letters*, vol. 21, no. 17, pp. 737-738, 1985.

[20] G. H. Dieke and H. M. Crosswhite, "The Spectra of the Doubly and Triply Ionized Rare Earths," *Applied Optics*, vol. 2, no. 7, pp. 675-686, 1963.

[21] A. J. Kenyon, "Recent developments in rare-earth doped materials for optoelectronics," *Progress in Quantum Electronics*, vol. 26, no. 4-5, pp. 225-284, 2002.

[22] B. R. Judd, "Optical Absorption Intensities of Rare-Earth Ions," *Physical Review*, vol. 127, no. 3, pp. 750-761, 1962.

[23] H. M. Pask, R. J. Carman, D. C. Hanna, A. C. Tropper, C. J. Mackechnie, P. R. Barber, and J. M. Dawes, "Ytterbium-Doped Silica Fiber Lasers - Versatile Sources for the 1-1.2 Mu-M Region," *Ieee Journal of Selected Topics in Quantum Electronics*, vol. 1, no. 1, pp. 2-13, Apr.1995.

[24] K. Lu and N. K. Dutta, "Spectroscopic properties of Yb-doped silica glass," *Journal of Applied Physics*, vol. 91, no. 2, pp. 576-581, Jan.2002.

[25] J. W. Y. Lit, "Recent advances in fiber lasers,", 2695 ed 1996, pp. 132-143.

[26] J. Nilsson and D. N. Payne, "High-Power Fiber Lasers," *Science*, vol. 332, no. 6032, pp. 921-922, May2011.

[27] J. L. Zyskind, V. Mizrahi, D. J. Digiovanni, and J. W. Sulhoff, "Short Single Frequency Erbium-Doped Fiber Laser," *Electronics Letters*, vol. 28, no. 15, pp. 1385-1387, July1992.

[28] L. F. Stokes, M. Chodorow, and H. J. Shaw, "All-Single-Mode Fiber Resonator," *Optics Letters*, vol. 7, no. 6, pp. 288-290, 1982.

[29] F. Zhang and J. W. Y. Lit, "Direct-Coupling Single-Mode Fiber Ring Resonator," *Journal of the Optical Society of America A-Optics Image Science and Vision*, vol. 5, no. 8, pp. 1347-1355, Aug.1988.

[30] Z. J. Chaboyer, P. J. Moore, and G. Das, "Medium power single-mode single-wavelength fiber laser," *Optics Commun.*, vol. 282, pp. 3100-3103, 2009.

[31] J. J. Zayhowski, "Limits Imposed by Spatial Hole Burning on the Single-Mode Operation of Standing-Wave Laser Cavities," *Optics Letters*, vol. 15, no. 8, pp. 431-433, Apr.1990.

[32] T. von Lerber and M. W. Sigrist, "Cavity-ring-down principle for fiber-optic resonators: experimental realization of bending loss and evanescent-field sensing," *Applied Optics*, vol. 41, no. 18, pp. 3567-3575, June2002.

[33] S. V. Chernikov, J. R. Taylor, and R. Kashyap, "Coupled-Cavity Erbium Fiber Lasers Incorporating Fiber Grating Reflectors," *Optics Letters*, vol. 18, no. 23, pp. 2023-2025, Dec.1993.

[34] P. C. Becker, N. A. Olsson, and J. R. Simpson, *Erbium-Doped Fiber Amplifiers: Fundamentals and Technology*, 1 ed. San Diego: Academic Press, 2010.

[35] M. E. Fermann and I. Hartl, "Ultrafast Fiber Laser Technology," *Ieee Journal of Selected Topics in Quantum Electronics*, vol. 15, no. 1, pp. 191-206, Jan.2009.

[36] D. Marcuse, "Interdependence of Waveguide and Material Dispersion," *Applied Optics*, vol. 18, no. 17, pp. 2930-2932, 1979.

[37] G. P. Agrawal, *Nonlinear Fiber Optics*, 3rd ed Academic Press, 2001.

[38] K. S. Kim, R. H. Stolen, W. A. Reed, and K. W. Quoi, "Measurement of the Nonlinear Index of Silica-Core and Dispersion-Shifted Fibers," *Optics Letters*, vol. 19, no. 4, pp. 257-259, Feb.1994.

[39] A. Chong, W. H. Renninger, and F. W. Wise, "Properties of normal-dispersion femtosecond fiber lasers," *Journal of the Optical Society of America B-Optical Physics*, vol. 25, no. 2, pp. 140-148, Feb.2008.

[40] H. A. Haus, "Mode-locking of lasers," *Ieee Journal of Selected Topics in Quantum Electronics*, vol. 6, no. 6, pp. 1173-1185, Nov.2000.

[41] F. Krausz, M. E. Fermann, T. Brabec, P. F. Curley, M. Hofer, M. H. Ober, C. Spielmann, E. Wintner, and A. J. Schmidt, "Femtosecond Solid-State Lasers," *Ieee Journal of Quantum Electronics*, vol. 28, no. 10, pp. 2097-2122, Oct.1992.

[42] J. N. Kutz, B. C. Collings, K. Bergman, S. Tsuda, S. T. Cundiff, W. H. Knox, P. Holmes, and M. Weinstein, "Mode-locking pulse dynamics in a fiber laser with a saturable Bragg reflector," *Journal of the Optical Society of America B-Optical Physics*, vol. 14, no. 10, pp. 2681-2690, Oct.1997.

[43] G. P. Lees and T. P. Newson, "Diode pumped high power simultaneously Q-switched and self mode-locked erbium doped fibre laser," *Electronics Letters*, vol. 32, no. 4, pp. 332-333, Feb.1996.

[44] P. Myslinski, J. Chrostowski, J. A. K. Koningstein, and J. R. Simpson, "Self-Mode Locking in A Q-Switched Erbium-Doped Fiber Laser," *Applied Optics*, vol. 32, no. 3, pp. 286-290, Jan.1993.

[45] M. V. Andres, J. L. Cruz, A. Diez, P. Perez-Millan, and M. gado-Pinar, "Actively Q-switched all-fiber lasers," *Laser Physics Letters*, vol. 5, no. 2, pp. 93-99, Feb.2008.

[46] D. Marcuse, "Pulsing Behavior of A 3-Level Laser with Saturable Absorber," *Ieee Journal of Quantum Electronics*, vol. 29, no. 8, pp. 2390-2396, Aug.1993.

[47] Y. K. Kuo and Y. A. Chang, "Numerical study of passive Q switching of a Tm : YAG laser with a Ho : YLF solid-state saturable absorber," *Applied Optics*, vol. 42, no. 9, pp. 1685-1691, Mar.2003.

[48] Y. F. Chen, Y. P. Lan, and H. L. Chang, "Analytical model for design criteria of passively Q-switched laser," *Ieee Journal of Quantum Electronics*, vol. 37, no. 3, pp. 462-468, Mar.2001.

[49] F. X. Kartner, L. R. Brovelli, D. Kopf, M. Kamp, I. Calasso, and U. Keller, "Control of Solid-State Laser Dynamics by Semiconductor-Devices," *Optical Engineering*, vol. 34, no. 7, pp. 2024-2036, July1995.

[50] J. Lee, J. Koo, Y. M. Chang, P. Debnath, Y. W. Song, and J. H. Lee, "Experimental investigation on a Q-switched, mode-locked fiber laser based on the combination of active mode locking and passive Q switching," *Journal of the Optical Society of America B-Optical Physics*, vol. 29, no. 6, pp. 1479-1485, June2012.

[51] C. Honninger, R. Paschotta, F. Morier-Genoud, M. Moser, and U. Keller, "Q-switching stability limits of continuous-wave passive mode locking," *Journal of the Optical Society of America B-Optical Physics*, vol. 16, no. 1, pp. 46-56, Jan.1999.

[52] A. Galvanauskas, "High Power Fiber Lasers,", July 2004 ed 2004, pp. 42-47.

[53] F. O. Ilday, J. Buckley, L. Kuznetsova, and F. W. Wise, "Generation of 36-femtosecond pulses from a ytterbium fiber laser," *Optics Express*, vol. 11, no. 26, pp. 3550-3554, Dec.2003.

[54] C. Tsai, J. Chen, and W. Wang, "Near-Infrared Absorption Property of Biological Soft Tissue Constituents," *Journal of Medical and Biological Engineering*, 2001.

[55] E. Viherkoski, "Lasers in Medicine," *Annales Chirurgiae et Gynaecologiae*, vol. 79, no. 4, pp. 176-181, 1990.

[56] J. Nilsson and D. N. Payne, "High-Power Fiber Lasers," *Science*, vol. 332, no. 6032, pp. 921-922, May2011.

[57] Y. Jeong, J. K. Sahu, D. N. Payne, and J. Nilsson, "Ytterbium-doped large-core fiber laser with 1.36 kW continuous-wave output power," *Optics Express*, vol. 12, no. 25, pp. 6088-6092, Dec.2004.

[58] C. Florea and K. A. Winick, "Ytterbium-doped glass waveguide laser fabricated by ion exchange," *Journal of Lightwave Technology*, vol. 17, no. 9, pp. 1593-1601, Sept.1999.

[59] G. Herzberg and J. W. T. Spinks, *Atomic Spectra and Atomic Structure*, 2 ed. New York: Dover Publications, 1944.

[60] C. Jiang, H. Jiu, Q. Zeng, Y. Wang, J. Zhang, and F. Gan, "Stark Energy Split Characteristics of ytterbium ion in glasses," *Rare-Earth-Doped Materials and Devices IV*, vol. 4 2000.

[61] S. X. Dai, A. Sugiyama, L. L. Hu, Z. P. Liu, G. S. Huang, and Z. H. Jiang, "The spectrum and laser properties of ytterbium doped phosphate glass at low temperature," *Journal of Non-Crystalline Solids*, vol. 311, no. 2, pp. 138-144, Nov.2002.

[62] K. Lu and N. K. Dutta, "Spectroscopic properties of Yb-doped silica glass," *Journal of Applied Physics*, vol. 91, no. 2, pp. 576-581, Jan.2002.

[63] B. Poumellec, P. Niay, M. Douay, and J. F. Bayon, "The UV-induced refractive index grating in Ge:SiO2 preforms: Additional CW experiments and the macroscopic origin of the change in index," *Journal of Physics D-Applied Physics*, vol. 29, no. 7, pp. 1842-1856, July1996.

[64] K. O. Hill and G. Meltz, "Fiber Bragg grating technology fundamentals and overview," *Journal of Lightwave Technology*, vol. 15, no. 8, pp. 1263-1276, Aug.1997.

[65] G. Meltz, W. W. Morey, and W. H. Glenn, "Formation of Bragg Gratings in Optical Fibers by A Transverse Holographic Method," *Optics Letters*, vol. 14, no. 15, pp. 823-825, Aug.1989.

[66] D. K. W. Lam and B. K. Garside, "Characterization of Single-Mode Optical Fiber Filters," *Applied Optics*, vol. 20, no. 3, pp. 440-445, 1981.

[67] J. Xu and R. Stroud, *Acousto-Optic Devices: Principles, Design, and Applications*. New York: Wiley, 1992.

[68] R. Ulrich and A. Simon, "Polarization Optics of Twisted Single-Mode Fibers," *Applied Optics*, vol. 18, no. 13, pp. 2241-2251, 1979.

[69] J. Noda, K. Okamoto, and Y. Sasaki, "Polarization-Maintaining Fibers and Their Applications," *Journal of Lightwave Technology*, vol. 4, no. 8, pp. 1071-1089, Aug.1986.

[70] R. Ulrich, S. C. Rashleigh, and W. Eickhoff, "Bending-Induced Birefringence in Single-Mode Fibers," *Optics Letters*, vol. 5, no. 6, pp. 273-275, 1980.

[71] H. C. Lefevre, "Single-Mode Fiber Fractional Wave Devices and Polarization Controllers," *Electronics Letters*, vol. 16, no. 20, pp. 778-780, 1980.

[72] V. N. Philippov, A. V. Kir'yanov, and S. Unger, "Advanced configuration of erbium fiber passively Q-switched laser with Co2+: ZnSe saturable absorber," *IEEE Photonics Technology Letters*, vol. 16, no. 1, pp. 57-59, Jan.2004.

[73] U. Keller, K. J. Weingarten, F. X. Kartner, D. Kopf, B. Braun, I. D. Jung, R. Fluck, C. Honninger, N. Matuschek, and J. A. derAu, "Semiconductor saturable absorber mirrors (SESAM's) for femtosecond to nanosecond pulse generation in solid-state lasers," *Ieee Journal of Selected Topics in Quantum Electronics*, vol. 2, no. 3, pp. 435-453, Sept.1996.

[74] Y. Pang and F. Wise, "Use of Saturable Absorber Dyes for Self-Starting Operation of A Self-Mode-Locked Ti-Al2O3 Laser," *Optical and Quantum Electronics*, vol. 24, no. 8, pp. 841-849, Aug.1992.

[75] A. S. Kurkov, "Q-switched all-fiber lasers with saturable absorbers," *Laser Physics Letters*, vol. 8, no. 5, pp. 335-342, May2011.

[76] R. Paschotta and U. Keller, "Passive mode locking with slow saturable absorbers," *Applied Physics B-Lasers and Optics*, vol. 73, no. 7, pp. 653-662, Nov.2001.

[77] F. X. Kartner, J. A. D. Au, and U. Keller, "Mode-locking with slow and fast saturable absorbers - What's the difference?," *Ieee Journal of Selected Topics in Quantum Electronics*, vol. 4, no. 2, pp. 159-168, Mar.1998.

[78] H. A. Haus, "Theory of Mode-Locking with A Slow Saturable Absorber," *Ieee Journal of Quantum Electronics*, vol. 11, no. 9, pp. 736-746, 1975.

[79] F. X. Kartner and U. Keller, "Stabilization of Soliton-Like Pulses with A Slow Saturable Absorber," *Optics Letters*, vol. 20, no. 1, pp. 16-18, Jan.1995.

[80] S. Stepanov, "Dynamic population gratings in rare-earth-doped optical fibres," *Journal of Physics D-Applied Physics*, vol. 41, no. 22 Nov.2008.

[81] S. Stepanov, "Two-wave mixing via reflection population gratings," *Optik*, vol. 117, no. 4, pp. 151-162, 2006.

[82] E. Desurvire, "Study of the Complex Atomic Susceptibility of Erbium-Doped Fiber Amplifiers," *Journal of Lightwave Technology*, vol. 8, no. 10, pp. 1517-1527, Oct.1990.

[83] Y. Mitnick, M. Horowitz, and B. Fischer, "Coupling effects of signal and pump beams in three-level saturable-gain media," *Journal of the Optical Society of America B-Optical Physics*, vol. 15, no. 9, pp. 2433-2438, Sept.1998.

[84] M. Horowitz, R. Daisy, and B. Fischer, "Filtering behavior of a self-induced three-mirror cavity formed by intracavity wave mixing in a saturable absorber," *Optics Letters*, vol. 21, no. 4, pp. 299-301, Feb.1996.

[85] B. Fischer, J. L. Zuskind, and D. J. Digiovanni, "Nonlinear 4-Wave-Mixing in Erbium-Doped Fiber Amplifiers," *Electronics Letters*, vol. 29, no. 21, pp. 1858-1859, Oct.1993.

[86] D. K. W. Lam and B. K. Garside, "Characterization of Single-Mode Optical Fiber Filters," *Applied Optics*, vol. 20, no. 3, pp. 440-445, 1981.

[87] B. Wu and P. L. Chu, "Fast optical switching in Sm3+-doped fibers," *IEEE Photonics Technology Letters*, vol. 8, no. 2, pp. 230-232, Feb.1996.

[88] C. B. Layne, W. H. Lowdermilk, and M. J. Weber, "Multiphonon Relaxation of Rare-Earth Ions in Oxide Glasses," *Physical Review B*, vol. 16, no. 1, pp. 10-20, 1977.

[89] A. A. Fotiadi, A. S. Kurkov, and I. M. Razdobreev, "All-fiber Passively Q-switched Ytterbium Laser," 2005, p. 515.

[90] C. E. Preda, G. Ravet, and P. Megret, "Experimental demonstration of a passive all-fiber Q-switched erbium- and samarium-doped laser," *Optics Letters*, vol. 37, no. 4, pp. 629-631, Feb.2012.

[91] A. A. Fotiadi, I. M. Razdobreev, B. Segard, and A. S. Kurkov, "Stable Self-Pulse Behaviour of Two-Core Yb/Sm Fiber Laser," 2009, p. 1.

[92] U. Ghera, N. Friedman, and M. Tur, "A Fiber Laser with A Comb-Like Spectrum," *Ieee Photonics Technology Letters*, vol. 5, no. 10, pp. 1159-1161, Oct.1993.

[93] J. S. Wey, D. L. Butler, N. W. Rush, G. L. Burdge, and J. Goldhar, "Optical bit-pattern recognition by use of dynamic gratings in erbium-doped fiber," *Optics Letters*, vol. 22, no. 23, pp. 1757-1759, Dec.1997.

[94] H. Lim, F. O. Ilday, and F. W. Wise, "Femtosecond ytterbium fiber laser with photonic crystal fiber for dispersion control," *Optics Express*, vol. 10, no. 25, pp. 1497-1502, Dec.2002.

[95] P. Tournois, "New Diffraction Grating Pair with Very Linear Dispersion for Laser-Pulse Compression," *Electronics Letters*, vol. 29, no. 16, pp. 1414-1415, Aug.1993.

[96] H. A. Haus, "Theory of Mode-Locking with A Fast Saturable Absorber," *Journal of Applied Physics*, vol. 46, no. 7, pp. 3049-3058, 1975.

[97] H. A. Haus, J. G. Fujimoto, and E. P. Ippen, "Analytic Theory of Additive Pulse and Kerr Lens Mode-Locking," *Ieee Journal of Quantum Electronics*, vol. 28, no. 10, pp. 2086-2096, Oct.1992.

[98] W. J. Tomlinson, R. H. Stolen, and A. M. Johnson, "Optical-Wave Breaking of Pulses in Nonlinear Optical Fibers," *Optics Letters*, vol. 10, no. 9, pp. 457-459, 1985.

[99] N. N. Akhmediev, A. Ankiewicz, M. J. Lederer, and B. Luther-Davies, "Ultrashort pulses generated by mode-locked lasers with either a slow or a fast saturable-absorber response," *Optics Letters*, vol. 23, no. 4, pp. 280-282, Feb.1998.

[100] Y. Chen, F. X. Kartner, U. Morgner, S. H. Cho, H. A. Haus, E. P. Ippen, and J. G. Fujimoto, "Dispersion-managed mode locking," *Journal of the Optical Society of America B-Optical Physics*, vol. 16, no. 11, pp. 1999-2004, Nov.1999.

[101] F. W. Wise, A. Chong, and W. H. Renninger, "High-energy femtosecond fiber lasers based on pulse propagation at normal dispersion," *Laser & Photonics Reviews*, vol. 2, no. 1-2, pp. 58-73, Apr.2008.

[102] Y. Wang, A. Martinez-Rios, and H. Po, "Analysis of a Q-switched ytterbium-doped double-clad fiber laser with simultaneous mode-locking," *Optics Communications*, vol. 224, pp. 113-123, 2003.

[103] F. Brunet, Y. Taillon, P. Galarneau, and S. LaRochelle, "A simple model describing both self-mode locking and sustained self-pulsing in ytterbium-doped ring fiber lasers," *Journal of Lightwave Technology*, vol. 23, no. 6, pp. 2131-2138, June2005.

[104] A. B. Grudinin and S. Gray, "Passive harmonic mode locking in soliton fiber lasers," *Journal of the Optical Society of America B-Optical Physics*, vol. 14, no. 1, pp. 144-154, Jan.1997.

[105] Y. J. Deng and W. H. Knox, "Self-starting passive harmonic mode-locked femtosecond Yb3+-doped fiber laser at 1030 nm," *Optics Letters*, vol. 29, no. 18, pp. 2121-2123, Sept.2004.

[106] S. A. Zhou, D. G. Ouzounov, and F. W. Wise, "Passive harmonic mode-locking of a soliton Yb fiber laser at repetition rates to 1.5 GHz," *Optics Letters*, vol. 31, no. 8, pp. 1041-1043, Apr.2006.

[107] N. Kishi, J. N. Carter, R. Mottahedeh, P. R. Morkel, R. G. Smart, A. J. Seeds, J. S. Roberts, C. C. Button, D. N. Payne, A. C. Tropper, and D. C. Hanna, "Actively Mode-Locked and Passively Q-Switched Operation of Thulium-Doped Fiber Laser Using Multiquantum Well Asymmetric Fabry-Perot Modulator," *Electronics Letters*, vol. 28, no. 2, pp. 175-177, Jan.1992.

[108] H. A. Haus, E. P. Ippen, and K. Tamura, "Additive-Pulse Modelocking in Fiber Lasers," *Ieee Journal of Quantum Electronics*, vol. 30, no. 1, pp. 200-208, Jan.1994.

[109] M. Hofer, M. E. Fermann, F. Haberl, M. H. Ober, and A. J. Schmidt, "Mode-Locking with Cross-Phase and Self-Phase Modulation," *Optics Letters*, vol. 16, no. 7, pp. 502-504, Apr.1991.

[110] J. M. Soto-Crespo, M. Grapinet, P. Grelu, and N. Akhmediev, "Bifurcations and multiple-period soliton pulsations in a passively mode-locked fiber laser," *Physical Review e*, vol. 70, no. 6 Dec.2004.

[111] F. O. Ilday, J. R. Buckley, H. Lim, F. W. Wise, and W. G. Clark, "Generation of 50-fs, 5-nJ pulses at 1.03 mu m from a wave-breaking-free fiber laser," *Optics Letters*, vol. 28, no. 15, pp. 1365-1367, Aug.2003.

[112] Y. F. Chen, J. L. Lee, H. D. Hsieh, and S. W. Tsai, "Analysis of passively Q-switched lasers with simultaneous modelocking," *Ieee Journal of Quantum Electronics*, vol. 38, no. 3, pp. 312-317, Mar.2002.

[113] P. K. Mukhopadhyay, M. B. Alsous, K. Ranganathan, S. K. Sharma, P. K. Gupta, J. George, and T. P. S. Nathan, "Simultaneous Q-switching and mode-locking in an intracavity frequency doubled diode-pumped Nd : YVO4/KTP green laser with Cr4+: YAG," *Optics Communications*, vol. 222, no. 1-6, pp. 399-404, July2003.

[114] J. K. Jabczynski, W. Zendzian, and J. Kwiatkowski, "Q-switched mode-locking with acousto-optic modulator in a diode pumped Nd : YVO4 laser," *Optics Express*, vol. 14, no. 6, pp. 2184-2190, Mar.2006.

[115] L. G. Luo and P. L. Chu, "Passive Q-switched erbium-doped fibre laser with saturable absorber," *Optics Communications*, vol. 161, no. 4-6, pp. 257-263, Mar.1999.

[116] S. Forget, F. Druon, F. Balembois, P. Georges, N. Landru, J. P. Feve, J. L. Lin, and Z. M. Weng, "Passively Q-switched diode-pumped Cr4+ : YAG/Nd3+: GdVO4 monolithic microchip laser," *Optics Communications*, vol. 259, no. 2, pp. 816-819, Mar.2006.

[117] T. Y. Tsai, Y. C. Fang, H. M. Huang, H. X. Tsao, and S. T. Lin, "Saturable absorber Q- and gain-switched all-Yb(3+) all-fiber laser at 976 and 1064 nm," *Optics Express*, vol. 18, no. 23, pp. 23523-23528, Nov.2010.

[118] P. K. Jain, I. H. El-Sayed, and M. A. El-Sayed, "Au nanoparticles target cancer," *Nano Today*, vol. 2, no. 1, pp. 18-29, Feb.2007.

[119] K. A. Willets and R. P. Van Duyne, "Localized surface plasmon resonance spectroscopy and sensing," *Annual Review of Physical Chemistry*, vol. 58, pp. 267-297, 2007.

[120] K. Hering, D. Cialla, K. Ackermann, T. Dorfer, R. Moller, H. Schneidewind, R. Mattheis, W. Fritzsche, P. Rosch, and J. Popp, "SERS: a versatile tool in chemical and biochemical diagnostics," *Analytical and Bioanalytical Chemistry*, vol. 390, no. 1, pp. 113-124, Jan.2008.

[121] E. C. Dreaden, A. M. Alkilany, X. H. Huang, C. J. Murphy, and M. A. El-Sayed, "The golden age: gold nanoparticles for biomedicine," *Chemical Society Reviews*, vol. 41, no. 7, pp. 2740-2779, 2012.

[122] W. Demtroder, *Laser Spectroscopy: Basic Concepts and Instrumentation*, 3 ed. Berlin: Springer-Verlag, 2003.

[123] C. J. Murphy, A. M. Gole, S. E. Hunyadi, J. W. Stone, P. N. Sisco, A. Alkilany, B. E. Kinard, and P. Hankins, "Chemical sensing and imaging with metallic nanorods," *Chemical Communications*, no. 5, pp. 544-557, 2008.

[124] C. Kittel, *Introduction to Solid State Physics*, 8 ed. Hoboken, NJ: Wiley, 2004.

[125] H. P. Myers, *Introductory Solid State Physics*, 2 ed CRC Press, 1997.

[126] S. A. Maier, *Plasmonics: Fundamentals and Applications*, 1 ed. New York: Springer, 2007.

[127] K. L. Kelly, E. Coronado, L. L. Zhao, and G. C. Schatz, "The optical properties of metal nanoparticles: The influence of size, shape, and dielectric environment," *Journal of Physical Chemistry B*, vol. 107, no. 3, pp. 668-677, Jan.2003.

[128] S. Link and M. A. El-Sayed, "Size and temperature dependence of the plasmon absorption of colloidal gold nanoparticles," *Journal of Physical Chemistry B*, vol. 103, no. 21, pp. 4212-4217, May1999.

[129] R. Weissleder, "A clearer vision for in vivo imaging," *Nature Biotechnology*, vol. 19, no. 4, pp. 316-317, Apr.2001.

[130] C. Tsai, J. Chen, and W. Wang, "Near-Infrared Absorption Property of Biological soft Tissue Constituents," *Journal of Medical and Biological Engineering*, 2001.

[131] S. J. Oldenburg, R. D. Averitt, S. L. Westcott, and N. J. Halas, "Nanoengineering of optical resonances," *Chemical Physics Letters*, vol. 288, no. 2-4, pp. 243-247, May1998.

[132] Y. Y. Yu, S. S. Chang, C. L. Lee, and C. R. C. Wang, "Gold nanorods: Electrochemical synthesis and optical properties," *Journal of Physical Chemistry B*, vol. 101, no. 34, pp. 6661-6664, Aug.1997.

[133] X. H. Huang, S. Neretina, and M. A. El-Sayed, "Gold Nanorods: From Synthesis and Properties to Biological and Biomedical Applications," *Advanced Materials*, vol. 21, no. 48, pp. 4880-4910, Dec.2009.

[134] S. Link, M. B. Mohamed, and M. A. El-Sayed, "Simulation of the optical absorption spectra of gold nanorods as a function of their aspect ratio and the effect of the medium dielectric constant," *Journal of Physical Chemistry B*, vol. 103, no. 16, pp. 3073-3077, Apr.1999.

[135] C. F. Bohren and D. R. Huffman, *Absorption and Scattering of Light by Small Particles*, 1 ed. New York: John Wiley and Sons, 1983.

[136] M. Z. Liu and P. Guyot-Sionnest, "Mechanism of silver(I)-assisted growth of gold nanorods and bipyramids," *Journal of Physical Chemistry B*, vol. 109, no. 47, pp. 22192-22200, Dec.2005.

[137] J. Perez-Juste, I. Pastoriza-Santos, L. M. Liz-Marzan, and P. Mulvaney, "Gold nanorods: Synthesis, characterization and applications," *Coordination Chemistry Reviews*, vol. 249, no. 17-18, pp. 1870-1901, Sept.2005.

[138] B. Nikoobakht and M. A. El-Sayed, "Evidence for bilayer assembly of cationic surfactants on the surface of gold nanorods," *Langmuir*, vol. 17, no. 20, pp. 6368-6374, Oct.2001.

[139] D. Pissuwan, S. M. Valenzuela, M. C. Killingsworth, X. D. Xu, and M. B. Cortie, "Targeted destruction of murine macrophage cells with bioconjugated gold nanorods," *Journal of Nanoparticle Research*, vol. 9, no. 6, pp. 1109-1124, Dec.2007.

[140] C. X. Yu and J. Irudayaraj, "Multiplex biosensor using gold nanorods," *Analytical Chemistry*, vol. 79, no. 2, pp. 572-579, Jan.2007.

[141] E. Zaremba and W. Kohn, "Vanderwaals Interaction Between An Atom and A Solid-Surface," *Physical Review B*, vol. 13, no. 6, pp. 2270-2285, 1976.

[142] L. Ricci, M. Weidemuller, T. Esslinger, A. Hemmerich, C. Zimmermann, V. Vuletic, W. Konig, and T. W. Hansch, "A Compact Grating-Stabilized Diode-Laser System for Atomic Physics," *Optics Communications*, vol. 117, no. 5-6, pp. 541-549, June1995.

[143] K. Liu and M. G. Littman, "Novel Geometry for Single-Mode Scanning of Tunable Lasers," *Optics Letters*, vol. 6, no. 3, pp. 117-118, 1981.

[144] B. Nikoobakht, J. P. Wang, and M. A. El-Sayed, "Surface enhanced Raman scattering (SERS) of molecules on gold nanorods (NRs)," *Abstracts of Papers of the American Chemical Society*, vol. 223, p. C70, Apr.2002.